U.PORTO

MESTRADO
MEDICINA E ONCOLOGIA MOLECULARES

Development of a Multi-Organ-on-a-Chip Platform to Study Gastric Cancer Metastasis

Júlia Subotyak

M

2026

Júlia Subotyak

Development of a Multi-Organ-on-a-Chip Platform to Study Gastric Cancer Metastasis

Dissertação de Candidatura ao grau de **Mestre em Medicina e Oncologia Molecular** submetida à Faculdade de Medicina da Universidade do Porto

Orientador: Doutor Daniel André Gonçalves Ferreira

Investigador Júnior

Expression Regulation in Cancer

Instituto de Investigação e Inovação em Saúde (i3S)

Co-Orientadora: Doutora Carla Isabel Gonçalves de Oliveira

Investigadora Principal, Professora Afiliada

Instituto de Investigação e Inovação em Saúde (i3S)

Faculdade de Medicina da Universidade do Porto (FMUP)

Acknowledgments

Gostaria de começar por agradecer ao meu orientador, Dr. Daniel Ferreira. Despertou o meu interesse por esta área científica tão inovadora, tão diferente de tudo aquilo que alguma vez imaginei vir a trabalhar, e abriu-me a porta para um mundo científico inteiramente novo e desafiante. Ao longo deste ano, esteve sempre presente, oferecendo um apoio incansável e uma disponibilidade constante, mesmo nos momentos mais difíceis deste percurso. Mais do que orientar-me cientificamente, desafiou-me continuamente a superar-me, incentivando-me a nunca me acomodar e ajudando-me a crescer, dia após dia, como uma cientista melhor.

À minha co-orientadora, Dra. Carla Oliveira, estou profundamente grata por todas as discussões científicas que nos incentivam constantemente a melhorar, e pelas inúmeras ideias notáveis que enriqueceram este trabalho. O seu pensamento crítico e a forma como partilha o seu conhecimento são verdadeiramente inspiradores, e sinto-me privilegiada por ter tido a oportunidade de aprender consigo.

Às minhas colegas de laboratório, Catarina, Ana Pedro, Raquel e Beatriz, um agradecimento muito especial. Para além de toda a ajuda que me deram no laboratório no dia a dia, tornaram-se verdadeiras amigas ao longo desta jornada. Convosco, os dias mais difíceis tornaram-se mais leves, e cada conquista tornou-se mais gratificante por poder ser partilhada. Gostaria também de agradecer especialmente ao José, Sara, Ricardo, Marta e Alexandre, por toda a ajuda nas minhas experiências e pelas ideias, sempre valiosas para o desenvolvimento deste trabalho.

À Raquel, Margarida, João e Martim, que partilharam comigo estes últimos cinco anos naquela que foi, um dia, uma cidade completamente nova, nunca haverá palavras suficientes para vos agradecer. Obrigada por acreditarem sempre em mim, por estarem presentes em todas as fases desta jornada, e por fazerem com que até as noites de estudo mais longas se tornassem, de alguma forma, mais leves, simplesmente por estarem lá. O Porto nunca se teria tornado casa da mesma forma sem vocês, e tantas das memórias que vou levar destes anos são inseparáveis de vocês os quatro.

Aos meus amigos de sempre, obrigada por permanecerem sempre presentes, apesar da distância e da passagem do tempo. É reconfortante saber que haverá sempre um lugar, e pessoas, para onde posso voltar.

Por fim, e mais importante, gostaria de agradecer à minha família.

Aos meus pais, não há palavras que descrevam verdadeiramente o apoio que me deram, especialmente por me permitirem seguir aquilo que sempre quis sem nunca questionarem as minhas escolhas, e por apoiarem até as minhas ideias mais loucas. A vossa ajuda ao longo deste último ano foi inestimável, tornando o meu dia a dia mais fácil, mesmo nas coisas mais simples.

À minha irmã, a minha âncora e uma das minhas maiores inspirações na vida, obrigada por seres sempre alguém que admiro. Desde pequena que quis ser como tu, algo que provavelmente era óbvio na forma como tentava sempre vestir a tua roupa, usar as tuas coisas, e até agir como tu. Com o passar dos anos, acabámos por escolher caminhos académicos e profissionais muito diferentes, mas de alguma forma sempre permanecemos incrivelmente próximas. Apesar de os nossos mundos poderem, por vezes, parecer tão diferentes, continuas a ser uma das pessoas que melhor me conhece e uma daquelas a quem posso sempre recorrer. Ainda admiro a tua força, resiliência, paciência, e a forma como enfrentas tudo o que a vida te traz, e só espero conseguir levar comigo algumas dessas qualidades. Obrigada pelo teu apoio incondicional, pelos teus conselhos, pela tua paciência e, claro, por me aturares uma vida inteira. E ao meu cunhado, Manu, obrigada por estares sempre presente também, pelo teu apoio constante, e por te teres tornado uma parte tão importante da nossa família e da minha vida. Tenho muita sorte por vos ter a ambos ao meu lado.

A todos vocês que, de uma forma ou de outra, fizeram parte desta jornada, obrigada por a tornarem não só possível, mas também verdadeiramente significativa.

Abstract

Gastric cancer (GC) remains a major cause of cancer-related mortality worldwide, with metastatic dissemination representing the main determinant of poor clinical outcome. Importantly, metastasis is not a random process, and the two major Laurén histological subtypes display distinct patterns of dissemination. Intestinal-type gastric cancer (IGC) predominantly spreads through hematogenous routes to distant organs, particularly the liver, lungs, and bone, whereas diffuse-type gastric cancer (DGC) shows a marked propensity for peritoneal dissemination. These differences suggest that metastatic progression is determined not only by tumor-intrinsic properties but also by interactions with organ-specific microenvironments.

Despite these well-established clinical patterns, the mechanisms that determine organ-specific metastatic colonization remain poorly understood. Conventional *in vitro* models generally isolate individual steps of the metastatic cascade and cannot reproduce the systemic interactions between the primary tumor, circulation, and distant tissues. Animal models provide greater biological complexity but are limited by interspecies differences, reduced experimental controllability, and ethical concerns. Also, disease progression in both patients and animal models is ultimately constrained by survival, potentially, in the case of DGC, preventing us from observing the complete metastatic trajectory from being observed.

This project aimed to establish the technological and biological foundations of MetaCHIP, a multi-organ-on-a-chip platform designed to connect a primary gastric tumor model with multiple potential metastatic niches through a shared perfusable vascular compartment. Device development combined multiple microfluidic designs and fabrication with computational modelling, followed by experimental assessment of the integrity of the device. In parallel, biological models representing the intestinal and diffuse gastric tumor subtypes, the vascular compartment, and selected metastatic niches were established and characterized to define conditions suitable for their future integration within the platform.

The engineering process resulted in the MetaCHIP v5 design, which improved fabrication reliability and reproducible Matrigel confinement while maintaining fluidic integrity under continuous perfusion. Computational and experimental analyses supported a low-shear, diffusion-dominated transport regime between the vascular channel and the tissue compartments. Both GC cell lines successfully generated viable and metabolically active

spheroids suitable for prolonged culture. HUVEC-C cells successfully attached and formed a confluent monolayer within the fibronectin-coated perfusable channel. Furthermore, BEAS-2B and HepaRG cells maintained comparable metabolic activity in F-12K relative to their conventional culture conditions, supporting the feasibility of a shared culture environment for the lung and liver compartments so far.

In summary, this work established the technological validation of the fabricated device, which proved to be easy to fabricate, highly reproducible, structurally robust, leak-free, and capable of sustaining endothelial culture. It also validated individually the biological components that will be integrated into the chip in the future. So far, these findings are consistent with the reliability of our fabricated device. And we expect this system may provide a human-relevant and animal-free platform to investigate the mechanisms underlying gastric cancer organotropism and tumor–organ interactions.

Resumo

O cancro gástrico (GC) continua a ser uma importante causa de mortalidade associada ao cancro a nível mundial, sendo a disseminação metastática o principal determinante de um mau prognóstico clínico. É importante salientar que a metastização não é um processo aleatório e que os dois principais subtipos histológicos definidos pela classificação de Laurén apresentam padrões distintos de disseminação. O cancro gástrico do tipo intestinal (IGC) dissemina-se predominantemente por via hematogénica para órgãos distantes, particularmente o fígado, os pulmões e o osso, enquanto o cancro gástrico do tipo difuso (DGC) apresenta uma propensão para a disseminação peritoneal. Estas diferenças sugerem que a progressão metastática é determinada não apenas por propriedades intrínsecas das células tumorais, mas também pelas suas interações com microambientes específicos de cada órgão.

Apesar destes padrões clínicos estarem bem estabelecidos, os mecanismos que determinam a colonização metastática específica de cada órgão ainda são pouco compreendidos. Os modelos convencionais *in vitro* tendem a isolar etapas individuais do processo metastático e não conseguem reproduzir as interações sistémicas entre o tumor primário, a circulação e os tecidos distantes. Os modelos animais proporcionam uma maior complexidade biológica, mas apresentam limitações relacionadas com diferenças interespécies, menor controlo experimental e questões éticas. Além disso, a progressão da doença, tanto em doentes como em modelos animais, encontra-se inevitavelmente limitada pela sobrevivência do hospedeiro, o que, particularmente no caso do DGC, poderá impedir a observação da trajetória metastática na totalidade.

Este projeto teve como objetivo estabelecer as bases tecnológicas e biológicas do MetaCHIP, uma plataforma multi-organ-on-a-chip produzida para conectar um modelo de tumor gástrico primário a múltiplos nichos metastáticos potenciais através de um compartimento vascular comum. O desenvolvimento do dispositivo combinou diferentes desenhos microfluídicos e processos de fabrico com modelação computacional, seguidos de uma avaliação experimental da integridade do dispositivo. Em paralelo, foram estabelecidos e caracterizados modelos biológicos representativos dos subtipos intestinal e difuso do cancro gástrico, do compartimento vascular e de nichos metastáticos selecionados, com o objetivo de definir condições adequadas à sua futura integração na plataforma.

O processo de desenvolvimento resultou no desenho MetaCHIP v5, que melhorou a fiabilidade do fabrico e a reprodutibilidade do confinamento de Matrigel, mantendo simultaneamente a integridade fluídica sob perfusão contínua. As análises computacionais e experimentais suportaram a existência de um regime de transporte dominado por difusão e sujeito a baixo “shear stress” entre o canal vascular e os compartimentos tecidulares. Ambas as linhas celulares de GC formaram com sucesso esferoides viáveis e metabolicamente ativos, adequados para cultura prolongada. As células HUVEC-C aderiram com sucesso e formaram uma monocamada confluente no canal revestido com fibronectina. Adicionalmente, as células BEAS-2B e HepaRG mantiveram uma atividade metabólica comparável em F-12K relativamente às respetivas condições de cultura convencionais, apoiando, até ao momento, a viabilidade da utilização de um meio de cultura comum para os compartimentos pulmonar e hepático.

Resumidamente, este trabalho permitiu estabelecer a validação tecnológica do dispositivo desenvolvido, que demonstrou ser de fabrico simples, altamente reprodutível, estruturalmente robusto, isento de fugas e capaz de sustentar cultura endotelial. Paralelamente, foram validados individualmente os componentes biológicos que serão futuramente integrados no chip. Até ao momento, estes resultados suportam a fiabilidade do dispositivo desenvolvido. Espera-se que, no futuro, este sistema possa constituir uma plataforma relevante para a fisiologia humana e livre de recurso a modelos animais, permitindo investigar os mecanismos subjacentes ao organotropismo do cancro gástrico e às interações entre o tumor e os diferentes órgãos.

Scientific Outputs

Conference Communications:

Júlia Subotyak, Raquel Fernandes, Celina São José, Ana Pedro, Peter Ertl, Gustavo Mostoslavsky, Ricardo Amorim, Carla Oliveira, and Daniel Ferreira. Deciphering Metastatic Tropism in Gastric Cancer Using a Multi-Organ-on-a-Chip System. **21st YES Meeting – Young European Scientist Meeting**, Porto, Portugal, 17–20 September 2026. **Oral presentation.**

Júlia Subotyak, Raquel Fernandes, Celina São José, Ana Pedro, Peter Ertl, Gustavo Mostoslavsky, Ricardo Amorim, Carla Oliveira, and Daniel Ferreira. Metastatic Patterning of Gastric Cancer using Multi-Organ-on-a-Chip Technology. **7th Annual EUROoCS Conference**, Braga, Portugal, 22–24 June 2026. **Poster presentation.**

Júlia Subotyak, Raquel Fernandes, Celina São José, Ana Pedro, Peter Ertl, Gustavo Mostoslavsky, Ricardo Amorim, Carla Oliveira, and Daniel Ferreira. An Organoid-Based Multi-Organ-on-a-Chip Platform for Studying Gastric Cancer Metastasis. **19th IJUP – Young Researchers Meeting of the University of Porto**, 6–8 May 2026. **Poster presentation.**

Júlia Subotyak, Raquel Fernandes, Celina São José, Ana Pedro, Peter Ertl, Gustavo Mostoslavsky, Ricardo Amorim, Carla Oliveira, and Daniel Ferreira. Development of an Organoid-Based Multi-Organ-on-a-Chip to Study Gastric Cancer Metastasis. **32nd Porto Cancer Meeting**, 22–24 April 2026. **Poster presentation.**

Júlia Subotyak, Raquel Fernandes, Celina São José, Ana Pedro, Peter Ertl, Gustavo Mostoslavsky, Ricardo Amorim, Carla Oliveira, and Daniel Ferreira. An Organoid-Based Multi-Organ-on-a-Chip to Model Gastric Cancer Metastasis. **29th Annual Meeting of the Portuguese Society of Human Genetics (SPGH)**, 20–22 November 2025. **Poster presentation.**

Awards:

- **Best Poster Communication – Biological Sciences:**

Júlia Subotyak, Raquel Fernandes, Celina São José, Ana Pedro, Peter Ertl, Gustavo Mostoslavsky, Ricardo Amorim, Carla Oliveira, and Daniel Ferreira. An Organoid-Based Multi-Organ-on-a-Chip Platform for Studying Gastric Cancer Metastasis. 19th IJUP – Young Researchers Meeting of the University of Porto, 6–8 May 2026. **Poster presentation.**

Table of Contents

Ackowledgements 6

Abstract 8

Resumo 10

Scientific Outputs 12

Table of contents 14

List of Figures 18

List of Tables 21

Abbreviations 22

I. Introduction 25

1. Cancer 26

1.1. Global Incidence 26

1.2. Hallmarks of Cancer 26

2. Gastric Cancer 27

2.1. Epidemiology and Global Burden 27

2.2. Histological and Molecular Classification 29

2.3. Etiology and Risk Factors 31

2.3.1. Pathogenesis 32

2.3.2. Clinical Presentation, Staging and Prognosis 34

3. Metastasis 37

3.1. Gastric Cancer Metastasis 38

3.2. Current Models to Study Gastric Cancer 39

3.2.1. *In vitro* Models 39

3.2.2. *In vivo* Models 40

3.2.3. Clinical and Epidemiological Studies 41

3.2.4. Limitations of Current Models 42

3.2.5. The Resulting Gap 43

4. Advanced *In vitro* Models for Gastric Cancer Research 44
4.1. Organoids 44
4.2. Microfluidics 45
4.2.1. Organ-on-a-Chip 45
4.2.2. Multi-Organ-on-a-Chip and Metastatic Modeling 46

II. Rationale and Aims 49

III. Materials and Methods 53
1. Engineering 54
1.1. Microfluidic Device Design 54
1.2. Flow, Shear Stress, and Culture-Medium Permeation Simulation 54
1.3. Fabrication of the Device 56
1.4. System Assembly 58
1.5. Technological Validation 59
1.5.1. Structural Integrity Assessment 60
1.5.2. Hydrogel Confinement Assessment 60
1.5.3. Leakage Assessment 60
1.5.4. Matrigel Diffusion Assessment 61
2. Validation of the Biological Model 61
2.1. Cell Culture 62
2.2. Gastric Cancer Spheroids 64
2.2.1. Agarose Molds 64
2.2.2. Cell Seeding 65
2.2.3. Spheroid Harvest 67
2.2.4. Spheroid Growth Assessment 67
2.2.5. Spheroid Viability 68
2.3. Functional Characterization Assays 68
2.3.1. Metabolic Activity 68

2.3.2. Immunofluorescence 69
2.4. Endothelialization of the Vascular Compartment 70
2.4.1. Coating Optimization 70
2.4.2. Chip Endothelialization 70

IV. Results 73
1. Engineering 74
1.1. Device Design 74
1.2. Flow, Shear Stress, and Culture – Medium Permeation Simulation 75
1.3. Fabrication 79
2. Validation of the Technological Model 79
2.1. Hydrogel Confinement 79
2.2. Chamber Volume 80
2.3. Leakage Test 81
2.4. Diffusion Test 82
3. Validation of the Biological Model 84
3.1. Gastric Cancer Spheroids 84
3.1.1. Cell Seeding 85
3.1.2. MKN-74 Spheroids – Growth Kinetics and Viability 85
3.1.3. MKN-45 Spheroids – Growth Kinetics and Viability 88
3.1.4. Metabolic Activity 90
3.2. Artificial Vasculature 90
3.2.1. Coating Optmization 91
3.2.2. HUVECs-on-Chip 93
3.3. Medium Compatibility 93
3.3.1. Lung 94
3.3.2. Liver 94

V. Discussion 96

VI. References 109

List of Figures

Figure 1. **Map with the global distribution of incidence rates of GC, in both sexes, in 2024. Source: GLOBOCAN 2024** 28

Figure 2. **Histological (Laurén) and molecular (TCGA) classification systems of gastric adenocarcinoma**..... 31

Figure 3. **Comparison of the characteristic growth patterns of the two major Laurén histological subtypes of GC** 36

Figure 4. **Schematic representation of the main principles of Organ-on-a-Chip technology** 46

Figure 5. **Conceptual overview of the MetaCHIP platform** 52

Figure 6. **Reconstructed chip mask**..... 55

Figure 7. **Fabrication workflow of the MetaCHIP device** 57

Figure 8. **Schematic representation of the pressure-driven microfluidic flow control system (Elveflow, France) used to perfuse the MetaCHIP device**. 58

Figure 9. **Schematic representation of the pressurized-reservoir principle** 59

Figure 10. **Preparation of agarose microwell molds using the MicroTissues® 3D Petri Dish® micromold** 64

Figure 11. **Schematic representation of gastric cancer spheroid formation using the MicroTissues® 3D Petri Dish® agarose micromold.** 66

Figure 12. **Experimental setup used for HUVEC-C perfusion and chip endothelialization.** 72

Figure 13. **Evolution of the MetaCHIP device design across three successive design versions (v3–v5).** 75

Figure 14. **Full-chip velocity field (left) and detail of the inlet port-to-channel transition (right).** 75

Figure 15. **Lateral (wall-to-wall) velocity profile across the channel width at x = 25 mm, illustrating the near-wall slowdown.** 76

Figure 16. **Wall shear stress along the main channel and ports.** 77

Figure 17. **Time evolution of the culture-medium concentration (normalized to the source concentration) at the center of each of the three Matrigel chambers** 78

Figure 18. **Representative photograph of fabricated MetaCHIP devices (MetaCHIP v5, with 3 chambers).** 79

Figure 19. **Comparison of Matrigel confinement between 3 mm and 4 mm tissue chambers on a MetaCHIP v4 device.** 80

Figure 20. **Comparison of PDMS casting volumes and resulting tissue chamber volumes.** 81

Figure 21. **Leakage test of a MetaCHIP v4 device at T0h and T16h.** 82

Figure 22. **Preliminary diffusion test in a MetaCHIP v5 device** 83

Figure 23. **Quantitative diffusion assay in a MetaCHIP v5 device** 83

Figure 24. **Cell distribution within agarose microwells immediately after seeding (T0).** 85

Figure 25. **Brightfield images of MKN-74 spheroids embedded in Matrigel over 72h** 86

Figure 26. **Growth kinetics of MKN-74 spheroids in Matrigel** 86

Figure 27. **Growth of MKN-74 spheroids embedded in Matrigel during 72 h.** 87

Figure 28. **Viability of MKN-74 spheroids after 10 days in culture (6 days embedded in Matrigel)** 88

Figure 29. **Growth of MKN-45 spheroids embedded in Matrigel during 72 h** 89

Figure 30. **Viability of MKN-45 spheroids after 10 days in culture (6 days embedded in Matrigel)** 89

Figure 31. **Metabolic activity of MKN-74 and MKN-45 spheroids embedded in Matrigel.** 90

Figure 32. **Brightfield microscopy images of HUVEC-C** 91

Figure 33. **Immunofluorescence characterization of HUVEC-C cultured on fibronectin, gelatin, or uncoated coverslips** 92

Figure 34. **Comparison of HUVEC-C morphology on-chip and off-chip** 93

Figure 35. **Metabolic activity of BEAS-2B cells cultured in DMEM, F-12K, or DMEM/F-12** 94

Figure 36. **Metabolic activity of HepaRG cells cultured in William's E, F-12K, or DMEM/F-12,** 95

Listo of Tables

Table 1. **- T, N and M category definitions (AJCC 8th edition)** 34

Table 2. **- AJCC 8th edition stage groupings for gastric cancer** 35

Table 3. **- Metastatic site distribution by Laurén subtype (Dutch national cohort, n=8200)** 38

Table 4. **- Input parameters and computed wall shear stress values** 56

Table 5. **- Human cell lines and culture conditions used in this study**. 63

Table 6. **- Cell seeding densities used for gastric cancer spheroid generation** ... 65

Table 7. **- Numerical wall shear stress values** .....

Abbreviations

AJCC	American Joint Committee on Cancer
APC	APC Regulator of WNT Signaling Pathway
ARHGAP6	Rho GTPase Activating Protein 6
ARHGAP26	Rho GTPase Activating Protein 26
ARID1A	AT-Rich Interaction Domain 1A
ASCs	Adult Stem Cells
BCA	Bicinchoninic Acid
BSA	Bovine Serum Albumin
C/EBPα	CCAAT/Enhancer-Binding Protein Alpha
CAD	Computer-Aided Design
CAF	Cancer-Associated Fibroblast
CDH1	Cadherin 1
CDX	Cell Line-Derived Xenograft
CFD	Computational Fluid Dynamics
CIN	Chromosomal Instability
CLDN18	Claudin 18
CT	Computed Tomography
CTCs	Circulating Tumor Cells
CTNNA1	Catenin Alpha 1
DGC	Diffuse Gastric Cancer
DNA	Deoxyribonucleic Acid
DMEM	Dulbecco’s Modified Eagle Medium
EBV	Epstein–Barr Virus
ECM	Extracellular Matrix

EDTA	Ethylenediaminetetraacetic Acid
EGFR	Epidermal Growth Factor Receptor
EMT	Epithelial–Mesenchymal Transition
FAP	Familial Adenomatous Polyposis
FBS	Fetal Bovine Serum
FGFR2	Fibroblast Growth Factor Receptor 2
FR+ CTCs	Folate Receptor-Positive Circulating Tumor Cells
GC	Gastric Cancer
GEMMs	Genetically Engineered Mouse Models
GFP	Green Fluorescent Protein
GS	Genomically Stable
HDGC	Hereditary Diffuse Gastric Cancer
HER2	Human Epidermal Growth Factor Receptor 2
HUVEC-C	Human Umbilical Vein Endothelial Cells-C
IGC	Intestinal Gastric Cancer
ID	Inner Diameter
LGR5	Leucine-Rich Repeat-Containing G Protein-Coupled Receptor 5
MALT	Mucosa-Associated Lymphoid Tissue
MMP	Matrix Metalloproteinase
MoC	Multi-Organ-on-a-Chip
MSI	Microsatellite Instability
NF-κB	Nuclear Factor Kappa B
OD	Outer Diameter
OoC	Organ-on-a-Chip
PBS	Phosphate-Buffered Saline
PDMS	Polydimethylsiloxane

PDO	Patient-Derived Organoid
PDOX	Patient-Derived Orthotopic Xenograft
PDX	Patient-Derived Xenograft
PECAM-1	Platelet Endothelial Cell Adhesion Molecule 1
PFA	Paraformaldehyde
PPARγ	Peroxisome Proliferator-Activated Receptor Gamma
PCR	Polymerase Chain Reaction
PSCs	Pluripotent Stem Cells
RHOA	Ras Homolog Family Member A
SEER	Surveillance, Epidemiology, and End Results
SRB	Sulforhodamine B
TCGA	The Cancer Genome Atlas
TNM	Tumor–Node–Metastasis
cTNM	Clinical TNM
pTNM	Pathological TNM
ypTNM	Pathological Tumor–Node–Metastasis After Neoadjuvant Therapy
UV	Ultraviolet
VacA	Vacuolating Cytotoxin A

I. INTRODUCTION

1. Cancer

1.1. Global Incidence

Cancer is a multifactorial and progressive disease that arises from the transformation of normal cells into tumor cells through a multistep process involving the accumulation of genetic and epigenetic alterations, driven by the interplay between inherited susceptibility and external carcinogenic agents, including physical agents such as ultraviolet and ionizing radiation, chemical agents such as tobacco smoke and alcohol, and biological agents such as oncogenic infections [1]. This gradual disruption of cellular homeostasis leads to uncontrolled proliferation, resistance to regulatory mechanisms, and ultimately invasive growth, with incidence rising markedly with age as a reflection of cumulative carcinogen exposure and the progressive decline of cellular repair mechanisms [1].

In parallel with its biological complexity, cancer represents one of the most pressing public health challenges of the 21st century, accounting for nearly one in six deaths globally and one in four deaths from noncommunicable diseases and ranking among the three leading causes of death in individuals aged 30–69 years in most countries worldwide [2]. In 2022 alone, approximately 20 million new cases and 9.7 million deaths were reported across 185 countries [2]. Although mortality rates have declined in certain high-income countries, reflecting reduced smoking prevalence, earlier detection, and advances in targeted therapy and immunotherapy, such as the 34% decrease in cancer death rates observed in the United States since 1991, incidence continues to rise for several major malignancies, with shifting patterns toward younger adults and women and persistent racial disparities in outcomes [3]. Projections further indicate that the global cancer burden will increase substantially by 2050, driven by demographic growth, population aging, and inequalities in prevention and access to care [4].

1.2. Hallmarks of Cancer

The concept of the "hallmarks of cancer" was introduced in 2000 as a framework to organize the vast diversity of genetic and phenotypic alterations observed across human cancers [5]. Tumorigenesis was understood as a multistep evolutionary process in which normal cells progressively acquire specific biological capabilities that allow them to overcome regulatory barriers and develop into malignant tumors [6]. This original

framework identified six core capabilities: sustained proliferative signaling, evasion of growth suppressors, resistance to programmed cell death, replicative immortality, induction of angiogenesis, and activation of invasion and metastasis [5].

The framework was later expanded to include two further hallmarks, deregulation of cellular metabolism and evasion of immune destruction, alongside two enabling characteristics, genomic instability and tumor-promoting inflammation, that facilitate the acquisition of the others [6]. This update also introduced the tumor microenvironment as a relevant contributor, recognizing that cancer cells interact continuously with surrounding stromal and immune cells, vasculature, and extracellular matrix.

A subsequent revision added four more dimensions, unlocking phenotypic plasticity, non-mutational epigenetic reprogramming, polymorphic microbiomes, and senescent cells, reflecting a growing appreciation of tumor heterogeneity and non-genetic drivers of progression [7]. Most recently, an update reorganized the model around four integrated dimensions rather than a cumulative list: the hallmark capabilities, the characteristics enabling their acquisition, the tumor microenvironment, and systemic physiological interactions across the body [8]. Collectively, the hallmarks of cancer provide a unifying framework that helps explain the complex biological behavior of tumors and continues to guide research aimed at understanding cancer development and progression.

2. Gastric Cancer

2.1. Epidemiology and Global Burden

Gastric cancer (GC) is a malignant neoplasm arising from the epithelial cells of the gastric mucosa [9]. Despite a gradual decline in global incidence over recent decades, it remains a major global health burden. According to GLOBOCAN 2022, GC ranks as the fifth most common malignancy and the fifth leading cause of cancer-related mortality worldwide [10, 11]. The disease disproportionately affects men, with incidence rates approximately twice those observed in women, a pattern consistently reported across most regions, although the gap narrows in some high-incidence areas such as Eastern Asia and Eastern Europe, where women represent a proportionally larger share of cases [12, 13].

Marked geographical disparities characterize the global epidemiology of GC. The highest incidence rates are reported in Eastern Asia, Eastern Europe, and South America, whereas North America and much of Africa exhibit comparatively lower rates. This

disparity is reflected in cumulative risk estimates, which reach 2.64% in Eastern Asia compared with 0.42% in Southern Africa [14]. Countries such as South Korea and Japan maintain persistently elevated age-standardized incidence rates, yet South Korea, in particular, has one of the lowest gastric cancer mortality-to-incidence ratios worldwide. This pattern has been largely attributed to its nationwide endoscopic screening program, which has been associated with an approximately 47% reduction in gastric cancer mortality among individuals undergoing endoscopic screening [15].

The observed global decline in overall incidence has been largely attributed to improved food preservation through refrigeration, reduced consumption of salt-preserved foods, and falling rates of *H. pylori* infection, driven by better sanitation and broader antibiotic use [16]; however, marked regional disparities persist [10, 17]. Despite this downward trend, projections indicate that the absolute number of GC cases will continue to rise in the coming decades due to population growth and aging, with recent modelling estimating that approximately 15.6 million new GC cases will occur among individuals born between 2008 and 2017 alone, of which three-quarters would, in principle, be preventable through *H. pylori* eradication strategies [18]. Age-related trends are further complicated by a documented rise in early-onset GC, defined as diagnosis before age 50, with its share among all GC cases rising markedly over recent decades in several countries; this phenomenon is not fully explained by traditional risk factors and is increasingly considered a distinct epidemiological and clinicopathological entity that needs further investigation [19].

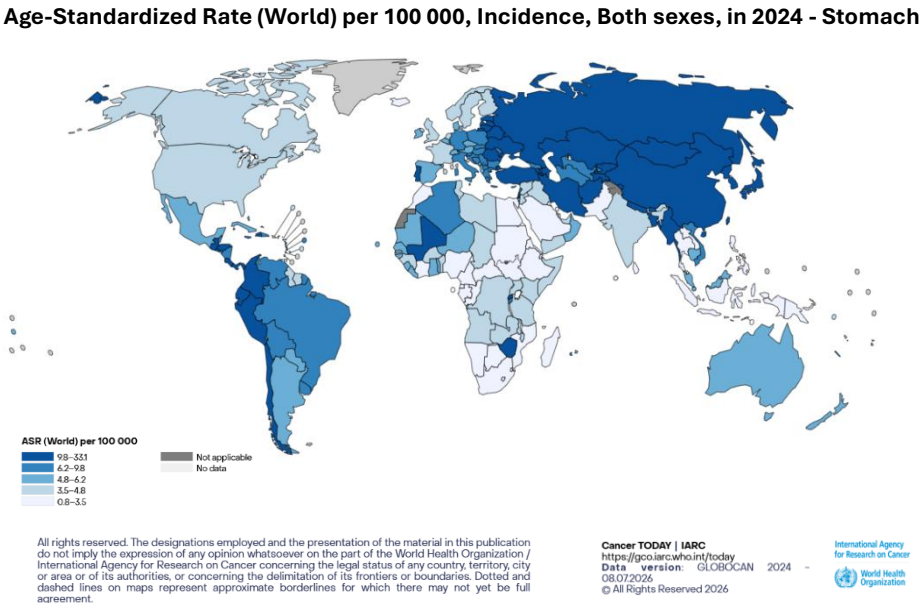


Figure 1. **Map with the global distribution of incidence rates of GC, in both sexes, in 2024.**
Source: GLOBOCAN 2024 (Access date: 12/07/2026).

2.2. Histological and Molecular Classification

Approximately 90% of gastric malignancies are adenocarcinomas, which constitute the primary focus of this thesis. The remaining cases comprise relatively uncommon malignancies, including mucosa-associated lymphoid tissue (MALT) lymphoma and mesenchymal tumors such as leiomyosarcoma [20]. Based on anatomical location, gastric adenocarcinoma is classified into cardia and non-cardia tumors, which differ in their epidemiological distribution, risk factor profiles, and underlying carcinogenic mechanisms. Cardia tumors arise near the gastroesophageal junction, whereas non-cardia tumors occur in the remaining stomach and are more closely linked to *H. pylori* infection and chronic atrophic gastritis [12, 14].

Histologically, the most widely used classification system is the Laurén classification, proposed in 1965, which categorizes gastric adenocarcinoma into three subtypes: intestinal, diffuse, and mixed (Figure 2) [21]. Despite the emergence of molecular classification systems, the Laurén classification remains the standard for routine histopathological diagnosis owing to its ability to capture clinically relevant differences in tumor morphology, histogenesis, differentiation, etiology, carcinogenesis, and prognosis [21].

The intestinal gastric cancer (IGC) is composed of cohesive tumor cells arranged in well-defined glandular or tubular structures, frequently arising in the setting of intestinal metaplasia [22, 23]. It predominantly affects older male patients and is strongly associated with chronic *H. pylori* infection and environmental risk factors [24-26]. Clinically, intestinal-type tumors generally exhibit a more cohesive growth pattern and preferentially disseminate through lymphatic and hematogenous routes [27].

In contrast, diffuse gastric cancer (DGC) is characterized by poorly cohesive tumor cells with little or no glandular differentiation, resulting in a diffusely infiltrative growth pattern [23]. The loss of cell-cell adhesion allows tumor cells to infiltrate the gastric wall individually or in small clusters, producing a scattered population of non-cohesive cells [9, 28]. Compared with IGC, DGC occurs more frequently in younger patients and shows a relatively higher incidence among women [9, 26]. These tumors are typically diagnosed at more advanced stages, infiltrate deeper into the gastric wall, and are associated with poorer clinical outcomes and a distinct metastatic pattern [11, 22].

Approximately 20% of gastric cancers are classified as mixed-type gastric cancer (MGC), reflecting the coexistence of intestinal and diffuse histological components within the same tumor. Unlike IGC and DGC, the biological behavior and prognostic significance of

MGC remains comparatively poorly understood [29]. Nevertheless, recent studies have associated this subtype with aggressive clinicopathological features and unfavorable clinical outcomes, with some reporting that its behavior and prognosis more closely resemble diffuse-type than intestinal-type disease [30].

Although the Laurén classification remains highly valuable in clinical practice, it does not fully capture the molecular heterogeneity of gastric cancer. Advances in genomic profiling have enabled a more refined molecular characterization of gastric adenocarcinoma, leading to the development of molecular classification systems that complement traditional histopathological approaches. The Cancer Genome Atlas (TCGA) proposed a comprehensive molecular classification comprising four distinct molecular subtypes: Epstein–Barr virus-positive (EBV), microsatellite instability (MSI), chromosomal instability (CIN), and genomically stable (GS) tumors [31]. These subtypes differ markedly in their genomic alterations, biological behavior, prognosis, and potential therapeutic vulnerabilities.

Although there is considerable overlap between histological and molecular classifications, they are not entirely concordant (Figure 2). The GS subtype is enriched for diffuse-type tumors and is characterized by frequent alterations in CDH1, which encodes E-cadherin, and RHOA, a small GTPase that regulates cytoskeletal dynamics and cell polarity. In contrast, MSI tumors are more commonly associated with the intestinal-type and generally have a more favorable prognosis, as well as increased responsiveness to immune checkpoint inhibitors, partly due to their high tumor mutational burden resulting from MLH1 promoter hypermethylation [31-33]. The CIN subtype, the most prevalent among the four, is characterized by frequent TP53 mutations and amplification of receptor tyrosine kinases and, similar to MSI, is more commonly associated with intestinal-type tumors [33]. The EBV-positive subtype, meanwhile, shows the highest degree of DNA hypermethylation among GC subtypes and frequent PD-L1/PD-L2 amplification, supporting its relevance as a target for immune checkpoint therapy [33]. Collectively, the TCGA classification has provided important biological insights into gastric cancer heterogeneity, reinforcing that gastric cancer comprises a spectrum of biologically distinct diseases rather than a single entity, and has built the foundation for the development of more personalized therapeutic strategies.

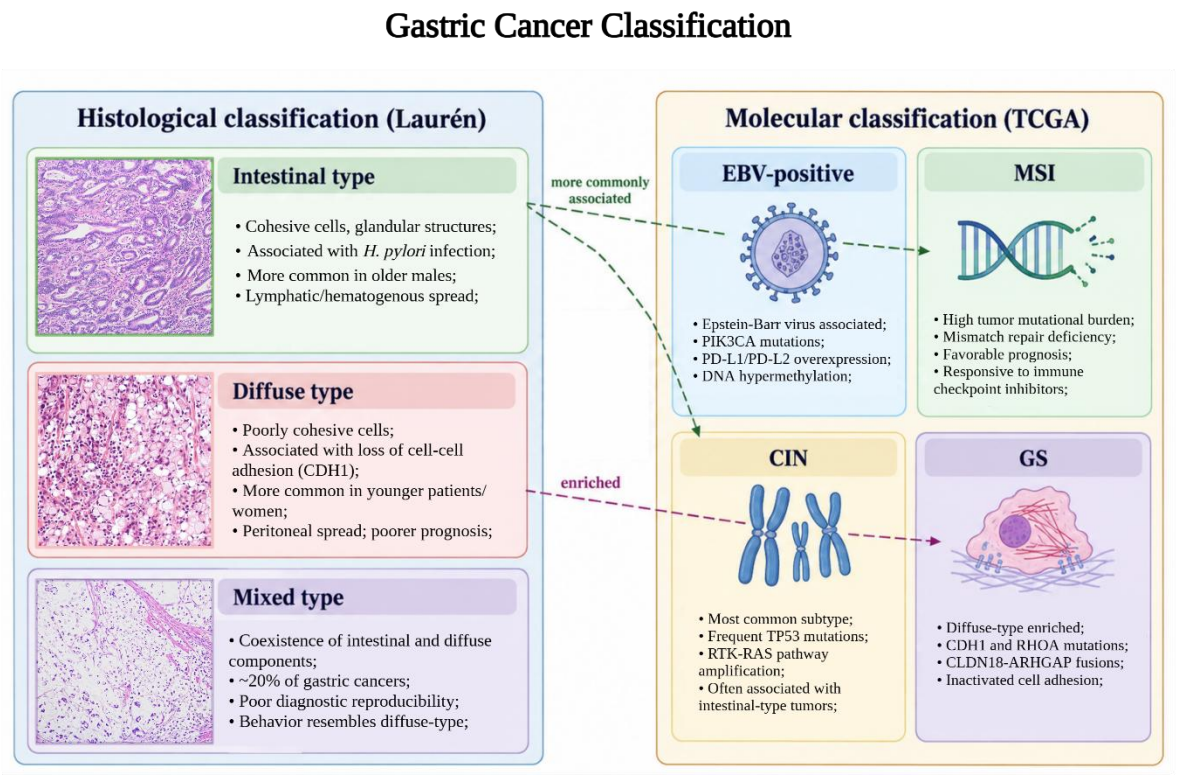


Figure 2. **Histological (Laurén) and molecular (TCGA) classification systems of gastric adenocarcinoma.** Arrows indicate the reported associations between histological subtypes and molecular classifications.

2.3. Etiology and Risk Factors

The etiology of GC is multifactorial, encompassing environmental, lifestyle, and genetic determinants. *H. pylori* infection stands as the most significant risk factor, implicated in approximately 89% of noncardia GC cases [14]. At the molecular level, this bacterium drives carcinogenesis through DNA damage induction, chronic mucosal inflammation, oxidative stress, and aberrant activation of oncogenic signaling pathways [10]. Notably, *H. pylori* exerts a stage-dependent dual role on apoptosis in gastric epithelial cells: during early infection, virulence factors such as VacA activate the mitochondria-mediated intrinsic apoptotic pathway as a host defence mechanism; however, as infection progresses towards malignancy, *H. pylori* shifts to suppressing apoptosis, facilitating tumor cell survival, proliferation, and dissemination [10].

Beyond infection, several environmental and lifestyle factors modulate GC risk. Dietary patterns play an important role, with high intake of salty and smoked foods increasing susceptibility, while diets rich in fresh fruit and vegetables confer a protective effect [26, 34]. Tobacco smoking and alcohol consumption are also established risk factors regardless of anatomical subsite, and available evidence suggests these two exposures

may act synergistically with each other and, in some populations, with *H. pylori* infection to further increase the risk [35]. Obesity has additionally been linked to GC risk, an association that is considerably more pronounced for cardia than for noncardia tumors [20]. Age represents a further, non-modifiable risk factor common to both cardia and noncardia disease, with incidence rising markedly beyond the fifth decade of life, reflecting the cumulative, multistep nature of gastric carcinogenesis [20]. Chronic atrophic gastritis and pernicious anemia are recognized precursor conditions that substantially elevate GC risk and represent key intermediate stages in the stepwise progression from normal mucosa to carcinoma [20]. EBV infection is an additional, less common etiological agent, corresponding to a distinct molecular subtype of GC already introduced in the context of the TCGA classification [31].

A positive family history, particularly in first-degree relatives, is associated with a two- to ten-fold increased risk of GC, reflecting the combined influence of shared genetic susceptibility and environmental exposures, including early-life *H. pylori* infection [20]. Most GCs are sporadic. Familial clustering is observed in about 10% of the cases. Only 1-3% arise in the context of well-defined inherited cancer syndromes [20, 22, 36]. The most common of these is Hereditary Diffuse Gastric Cancer (HDGC), although Lynch syndrome, Familial Adenomatous Polyposis (FAP), Peutz–Jeghers syndrome, and Li–Fraumeni syndrome have also been associated with an increased risk of GC [20, 36].

2.3.1. Pathogenesis

GC pathogenesis is biologically heterogeneous and closely linked to the histological subtype defined by Laurén, with IGC and DGC arising through partially distinct etiopathogenic routes.

In IGC, carcinogenesis classically follows the Correa cascade, a multistep sequence in which normal gastric mucosa progresses through chronic non-atrophic gastritis, chronic atrophic gastritis, intestinal metaplasia, dysplasia, and finally invasive adenocarcinoma [37]. Contemporary reviews continue to support this model and emphasize that *H. pylori* is its dominant initiating driver, acting through persistent inflammation, oxidative stress, DNA damage, and deregulation of major oncogenic pathways such as NF-κB, STAT3, Hippo, and Wnt/β-catenin [10, 38]. In this context, chronic infection promotes epithelial injury, gland loss, and a pro-tumorigenic inflammatory microenvironment that facilitates metaplastic and dysplastic transformation. Recent work by Li et al. (2024) further refines this sequence at the molecular level, showing that intestinal-type early gastric

carcinogenesis is accompanied by progressive acquisition of genomic alterations, with TP53 emerging as an important early event in progression beyond intestinal metaplasia, while alterations in genes such as APC, ARID1A, PIK3CA, and PRKDC may also accumulate during transition toward neoplasia [39, 40]. At the broader molecular level, intestinal-type tumors are frequently associated with the CIN subtype described by TCGA, characterized by aneuploidy and amplification of receptor tyrosine kinase pathways such as ERBB2/HER2, EGFR, FGFR2, and MET [38].

In contrast, DGC usually does not conform to the full Correa cascade and instead develops through mechanisms centered on loss of epithelial cohesion, abnormal cell polarity, cytoskeletal remodeling, and infiltrative growth [41]. DGC is composed of poorly cohesive cells, often including signet ring cells, that infiltrate the gastric wall diffusely rather than forming glandular structures [22, 42]. Consistent with the GS/diffuse-type overlap described above, DGC is strongly associated with recurrent, largely mutually exclusive alterations in CDH1, RHOA, and CLDN18–ARHGAP26/6 fusions [22, 31]. Mechanistically, these alterations converge on impaired intercellular adhesion and altered actin-cytoskeletal dynamics, thereby promoting cellular scattering, survival without anchorage, motility, invasion, and the characteristic non-cohesive phenotype of DGC [22].

A particularly important hereditary form of diffuse gastric carcinogenesis is HDGC, a cancer predisposition syndrome driven predominantly by germline pathogenic variants in CDH1 [43, 44] and also in CTNNA1 [45], both of which encode key components of the E-cadherin–catenin adhesion complex [46]. HDGC is a rare, autosomal dominant inherited form of GC, usually with a highly invasive diffuse-type tumor, a late presentation, and a poor prognosis [20]. CDH1 germline mutation carriers face a substantially elevated lifetime risk of developing gastric cancer, estimated at approximately 40% in men and 30% in women, considerably exceeding the risk observed in the general population, a disparity that underlies current clinical guidelines recommending prophylactic gastrectomy in confirmed high-risk carriers [22]. The central biological event in HDGC is loss of E-cadherin function [44], which destabilizes epithelial architecture, weakens cell–cell adhesion, and enables dissemination-prone behavior [47]. Importantly, pathogenesis in HDGC follows a tumor-suppressor model in which the inherited germline defect is typically followed by a second hit affecting the remaining wild-type allele [48]; recent literature continues to identify promoter hypermethylation as the most frequent mechanism of this second inactivation event [48, 49]. Histopathologically, HDGC stomachs often harbor multifocal, small, early-stage (intramucosal) signet ring cell lesions [46], many of which are small and occult, explaining why endoscopic

surveillance can miss disease and why prophylactic gastrectomy remains standard in high-risk carriers [49].

2.3.2. Clinical Presentation, Staging, and Prognosis

Clinically, one of the most significant challenges in GC management is the frequent delay in diagnosis. Early diseases are typically asymptomatic, and most symptoms of GC reflect advanced disease [50], contributing to a pattern in which diagnosis is consistently delayed until late stages of progression. When symptoms do manifest, they are often nonspecific, with weight loss and persistent abdominal pain being the most commonly reported [12].

Disease staging follows the TNM classification system of the American Joint Committee on Cancer (AJCC), wherein T reflects the depth of tumor invasion through the gastric wall, N indicates regional lymph node involvement, and M denotes the presence or absence of distant metastasis [34]. The pathological pTNM stage is the primary criterion for prognostic assessment, directly reflecting lymph node status and metastatic spread [28]. The full T, N, and M category definitions and their combination into stage groups (0 to IV) are summarized in Tables 1 and 2.

Table 1. **T, N and M category definitions (AJCC 8th edition).** Adapted from [51] and [52].

Category	Definition
Tis	Carcinoma *in situ;* intraepithelial tumor without invasion of the lamina propria
T1a	Tumor invades the lamina propria or muscularis mucosae
T1b	Tumor invades the submucosa
T2	Tumor invades the muscularis propria
T3	Tumor penetrates the subserosal connective tissue without invasion of the visceral peritoneum or adjacent structures
T4a	Tumor invades the serosa (visceral peritoneum)
T4b	Tumor invades adjacent structures or organs
N0	No regional lymph node metastasis
N1-N3	Metastasis in regional lymph nodes (depending on the number of nodes involved)
M0	No distant metastasis
M1	Distant metastasis present

Table 2. **AJCC 8th edition stage groupings for gastric cancer.** Adapted from [53].

Stage	General definition
0	Tis, N0, M0
I	Tumor confined to the gastric wall, with no or minimal nodal involvement
II	Greater local invasion and/or moderate nodal involvement
III	Locally advanced tumor and/or extensive nodal involvement
IV	Any T, any N, M1 (distant metastasis)

Staging can be assigned at different points in the clinical pathway, indicated by a prefix: cTNM ("clinical") reflects the pre-treatment estimate based on endoscopy and imaging (CT, endoscopic ultrasound), and guides initial treatment decisions such as the use of neoadjuvant chemotherapy; pTNM ("pathological") is determined by histopathological examination of the resected specimen after surgery and is generally considered the most accurate basis for prognosis and adjuvant treatment planning; and ypTNM refers to pathological staging performed after neoadjuvant therapy, reflecting treatment response rather than the original extent of disease [54].

This staging framework correlates strongly with clinical outcomes. In a study directly reporting 5-year survival by T category, rates declined progressively with depth of invasion: 84.3% for T1 tumors, 64.8% for T2, 48.9% for T3, and 29.2% for T4 [55]. This gap widens further at the extremes of disease: stage IV gastric cancer, defined by the presence of distant metastasis, carries a particularly poor prognosis, with 5-year survival rates of only 15–18% in Japanese and Korean cohorts [56]. This decline in survival with increasing stage underscores the central clinical relevance of metastatic spread as the single most important determinant of outcome in GC.

Importantly, the TNM system itself is histologically neutral; it classifies disease based purely on anatomical extent and is applied identically to both Laurén subtypes. What differs between IGC and DGC is not the staging system itself, but the stage at which each subtype tends to be diagnosed and the pattern by which it progresses through that staging scale (Figure 3).

As illustrated in Figure 3, the two Laurén subtypes exhibit fundamentally distinct growth patterns, which directly influence their clinical presentation and symptom onset [57]. In

the early stages of disease, DGC can present vague symptoms such as reflux or no symptoms at all, as the tumor infiltrates the musculature of the gastric wall (Figure 3B), leading to a rigid, leather-bottle stomach, a condition known as *linitis plastica* [58]. This infiltrative growth with an unpredictable pattern makes the disease visually absent, and endoscopic detection is particularly challenging, contributing to consistently later diagnosis compared with the intestinal subtype [58]. IGC, by contrast, is characterized by well-defined masses that are more easily endoscopically identified (Figure 3A), often arising through a stepwise progression from chronic gastritis to intestinal metaplasia and dysplasia, thereby facilitating earlier detection and enabling more effective screening, particularly in high-incidence regions [20, 37]. Having established how GC is diagnosed, staged, and how survival declines sharply with the acquisition of metastatic disease, the following section examines the specific patterns through which gastric cancer disseminates to distant organs.

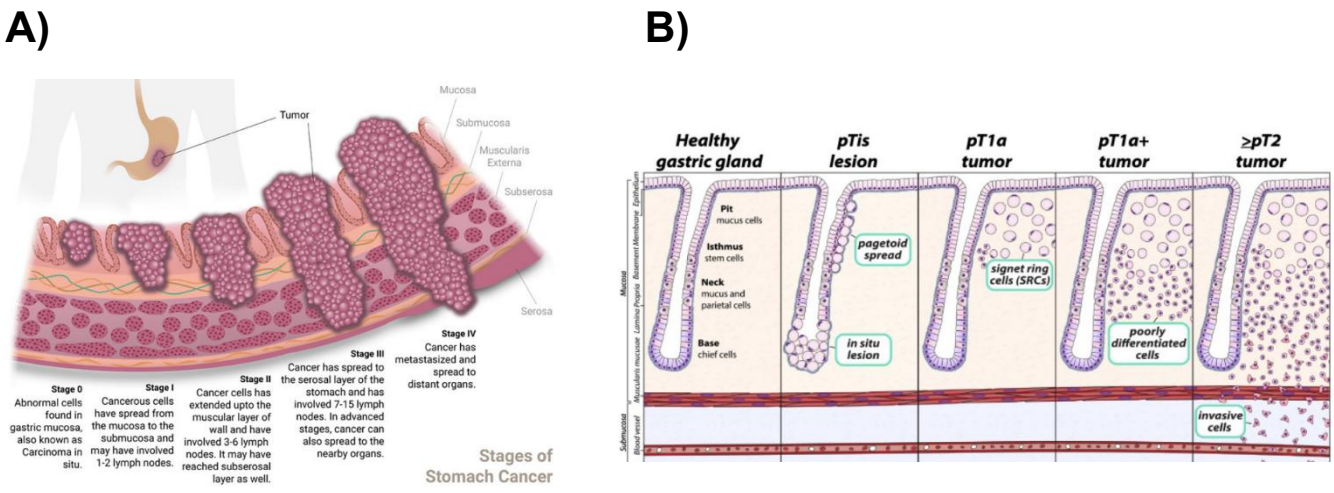


Figure 3. **Comparison of the characteristic growth patterns of the two major Laurén histological subtypes of GC.** A) IGC exhibits cohesive and expansive growth, progressively invading deeper layers of the gastric wall with increasing tumor stage; Adapted from the National Cancer Institute PDQ® Gastric Cancer Treatment [59]; B): DGC is characterized by infiltrative growth with pagetoid spread, signet-ring cell formation and diffuse invasion of the gastric wall without the formation of a well-defined tumor mass; Adapted from Monster *et al.* [57].

3. Metastasis

Metastasis is widely recognized as the principal cause of cancer-related mortality, accounting for most cancer deaths due to the spread of malignant cells from the primary tumor to distant organs and the subsequent physiological damage caused by tumor growth in those tissues [60-63]. Although major advances have been made in understanding the molecular and genetic basis of cancer, disease progression to metastatic stages still represents the cause of more than 90% of cancer-associated mortality [60, 62]. Clinically, cancers detected at early stages, before the dissemination to other organs occurs, are generally associated with more successful treatment outcomes, highlighting the significant challenge posed by metastatic disase [60]. Despite improvements in early detection and therapeutic strategies targeting primary tumors, the development of metastasis remains a major obstacle to effective cancer treatment, reflecting the still-limited understanding of the biological mechanisms associated with metastatic progression [62].

Metastasis is a complex and highly inefficient multistep process that requires tumor cells to complete several sequential events before establishing secondary tumors at distant sites. During this process, cancer cells first invade the surrounding tissue of the primary tumor, intravasate into blood or lymphatic vessels, and enter the circulation as circulating tumor cells (CTCs), which can then travel through the vasculature toward distant organs [61]. Once at these distant locations, tumor cells must extravasate from the circulation, adapt to the new microenvironment, and ultimately proliferate and colonize the tissue to form clinically detectable metastases [61].

Importantly, metastasis is not a random process. Many solid tumors exhibit characteristic patterns of organ-specific dissemination depending on the primary tumor's origin [63]. This phenomenon was historically described by Stephen Paget in the late nineteenth century through the “seed and soil” theory, which proposes that metastatic cells (“seeds”) can successfully colonize only those distant tissues (“soil”) that provide a permissive microenvironment for tumor growth [63]. These observations highlight the importance of both tumor cell intrinsic properties and the microenvironment of distant organs in determining metastatic colonization. Despite decades of research, however, many aspects of metastatic dissemination remain poorly understood, underscoring the need for improved experimental models capable of recapitulating the complex interactions between tumor cells and target tissues during metastatic progression [60-62].

3.1. Gastric Cancer Metastasis

As mentioned earlier, metastatic dissemination is critical in gastric cancer survival, and it also proves that metastasis is not a random process, since it has been shown that GC has subtype-specific dissemination. In a cohort study that involved 8231 patients to study metastatic patterning by Laurén subtype, IGC metastasized significantly more often to the liver (57%) and lungs (13%), whereas DGC metastasized significantly more to the peritoneum (58%) and bone (9% versus 6% for IGC) ($p<0.001$ for all comparisons). MGC displayed an intermediate pattern, more closely resembling DGC for peritoneal involvement (52%) and IGC for hepatic involvement (27%), consistent with its mixed histological composition. No significant difference between subtypes was found for extra-regional lymph node metastases ($p=0.231$) (Table 3) [23].

Table 3. **Metastatic site distribution by Laurén subtype (Dutch national cohort, n=8200).** Adapted from [23].

Metastatic site	IGC (%)	DGC (%)	MGC (%)	p-value
Liver	57	21	27	<0.001
Lung	13	7	9	<0.001
Peritoneum	29	58	52	<0.001
Bone	6	9	9	<0.001
Extra-regional lymph nodes	29	28	30	0.231
Adrenal gland	3	2	3	<0.009
Other	5	7	8	<0.001

These proportions are also consistent with other population-based data showing the liver, peritoneum, lung, and bone as the four most common metastatic sites in GC overall. Those studies also prove that survival in metastatic cancer remains poor regardless of the T- and N- stage, the site of metastasis, or the anatomical location of the primary tumor. Age emerged as a strong prognostic factor, with older patients showing poorer survival. Outcomes also showed variations in metastatic sites, where liver and bone

showed a poor survival of about 2 months, and those with thoracic (lung) metastasis showed somewhat better survival of approximately 4.5 months [64].

These different metastatic patterns reflect distinct step-by-step dissemination mechanisms. IGC cells retain a cohesive, gland-forming architecture [65] and disseminate primarily through a hematogenous route [66]. The process begins with Epithelial-Mesenchymal Transition (EMT), which allows tumor cells to invade the basal lamina and penetrate the gastric vasculature. Once detached from the primary nodule, single cells or tumor spheres must remain anoikis-resistant while circulating and endure the hypoxic, non-adherent conditions of the portal vein [67]. This portal drainage pattern accounts for the liver, lungs, and bone, which constitute the principal hematogenous sites reached by IGC, with tumor cells colonizing a preconditioned metastatic niche established before their arrival [66, 67]. Spread beyond the liver has been attributed to a cascadic, liver-to-systemic progression, or, in tumors located near the cardia, to venous drainage that bypasses the portal system entirely, allowing direct hematogenous spread to the lungs [64].

DGC, in contrast, is characterized by early loss of cell cohesion [62] and spreads through two main, non-hepatotropic routes. The first is direct contiguous extension, in which the tumor grows locally and invades along nearby lymphatics and ligaments (hepatoduodenal, gastrocolic, gastrosplenic, and gastrohepatic), eventually reaching the peritoneal cavity via the omentum [63]. The second is the peritoneal seeding cascade, a multistep process in which tumor cells detach from a tumor that has already invaded the serosa, survive the harsh, low-oxygen and low-glucose peritoneal environment, and then attach to the mesothelium lining the cavity. From there, they invade the underlying basement membrane and proliferate, promoting new blood vessel formation to support their growth [65]. This same loss of adhesion also underlies the early lymphatic and vascular invasion characteristic of DGC [62], reinforcing its dual tendency for lymphatic and peritoneal spread, further supported by an EMT/angiogenic program in the peritoneal microenvironment [66].

3.2. Current Models to Study Gastric Cancer Metastasis

3.2.1. *In vitro* models

In vitro investigation of GC metastatic potential relies predominantly on established human GC cell lines with well-documented invasive and migratory phenotypes,

including, for example, SGC-7901[68-70], MKN-45 [69, 71], AGS [72], MKN-7 and HSC44PE, a diffuse-type signet-ring cell line [71].

These lines are used to isolate discrete migratory and invasive capacities rather than to model metastasis as a process, most commonly using the scratch (wound-healing) assay and the transwell/Matrigel invasion assay, often alongside Matrix Metalloproteinases (MMP) activity as a marker of Extracellular Matrix (ECM) degradation [68, 69, 72, 73]. More complex 2D/3D co-culture systems incorporating stromal cells such as cancer-associated fibroblasts (CAFs) extend this approach by allowing cell-cell and cell-matrix interactions to be studied and have shown that invasion mode itself can differ between GC subtypes, with intestinal-type lines invading in a CAF-dependent manner and diffuse-type lines invading independently of CAF movement [71].

These same cell lines, having demonstrated invasive capacity *in vitro*, are also the ones most frequently xenografted into animal models to study GC metastasis *in vivo*, as discussed next

3.2.2. *In vivo* animal models

Animal models remain the most established platform for studying GC metastasis, as they are the only systems capable of recapitulating the full metastatic cascade, from the local invasion to distant organ colonization, within a living organism. The most widely used approach relies on cell line-derived xenografts (CDX), in which human GC cell lines such as MKN45 or AGS are implanted into immunodeficient mice. These models are valued for their reproducibility and controllability, and certain cell lines display consistent organotropism; for example, the MKN45 cell line preferentially disseminates to the liver and peritoneum [74]. However, subcutaneous implantation, the simplest and most common CDX approach, very rarely produces spontaneous metastasis, which led to the development of orthotopic models, in which tumor tissue or cell suspensions are implanted directly into the gastric wall. This approach was first explored in 1993, achieving 100% tumor formation with widespread dissemination to the lymph nodes and liver [74], and later GFP/luciferase-labelled cell lines were used to enable dynamic in vivo imaging of local invasion and hematogenous or lymphatic spread [75].

Some CDX models specifically developed to study peritoneal dissemination have been established using highly metastatic sublines generated through serial *in vivo* intraperitoneal passaging, such as MKN45-P. These models successfully recapitulate key pathological features of human peritoneal carcinomatosis, including organ invasion

and extensive stromal fibrosis, providing a clinically relevant platform for investigating the mechanisms underlying peritoneal metastasis and for evaluating novel therapeutic strategies [76].

Patient-derived xenografts (PDX) represent a step further in clinical relevance because they preserve the histological and genetic heterogeneity of the original tumor more faithfully than cell lines. Similarly to CDX, subcutaneous PDX implantation rarely metastasizes, whereas orthotopic implantation (patient-derived orthotopic xenografts, PDOX) shows a microenvironment more histologically and vascularly like the tumor of origin. PDOX models have proven that they can generate metastases in the liver, lungs, and peritoneal cavity, enriched in cancer stem cell populations [77]. Orthotopic implantation reliably outperforms subcutaneous implantation for modelling spontaneous metastatic dissemination [78].

Beyond transplantation-based approaches, genetically engineered mouse models (GEMMs) allow metastasis to arise *de novo* through defined genetic or epigenetic alterations in an intact organism, offering insight into the natural evolutionary trajectory of metastatic disease, though at the cost of longer latency and lower throughput compared to transplantation models [79].

3.2.3. Clinical and epidemiological studies

Side-by-side with experimental models, large-scale clinical and epidemiological studies can provide a population-level perspective on GC metastasis. The characterization of real-world patterns of dissemination, organotropism, and risk cannot be reproduced experimentally in animal and *in vitro* systems.

National and international cancer registries, such as the Dutch national cohort and the US SEER database, have been used to establish subtype- and subsite-specific metastatic patterns, showing that metastatic organotropism differs according to the primary tumor's anatomical subsite within the stomach, for example, with cardia tumors preferentially metastasizing to the liver and other subsites showing a different organotropism [23, 80]. The metastatic distribution data provided by the Dutch cohort was previously presented in section 3.1 (Table 3).

Beyond describing population-level patterns, clinical studies are also used to identify and validate circulating biomarkers capable of predicting metastatic risk before it becomes clinically evident. Preoperative folate receptor-positive circulating tumor cells (FR+

CTCs), combined with other serum markers, have been shown to predict occult peritoneal metastasis and early recurrence in GC patients with high sensitivity [81].

Unlike experimental models, clinical and epidemiological studies cannot be manipulated to test causal mechanisms; instead, their value lies in grounding mechanistic hypotheses generated in real, patient-derived patterns of disease behavior and in validating candidate biomarkers and models for clinical translation.

3.2.4. Limitations of current models

Each category of model discussed above carries limitations that constrain its ability to fully capture GC metastasis.

In vitro cell-based assays are inherently reductionist: they isolate single cellular behaviors, migration, invasion, and proteolytic activity from a static, two-dimensional or simplified three-dimensional context and cannot reproduce the sequential, multistep nature of the metastatic cascade, including vascular circulation, immune surveillance, or colonization of a distant organ [73].

Although animal models can reproduce the complete metastatic cascade, they also present several important limitations. Most xenograft models rely on immunodeficient mice, which lack a functional immune system and therefore cannot capture immune-tumor interactions known to shape metastatic progression [82]. Inter-species differences represent another major limitation. Although mice and humans share approximately 80% similarity, they differ in gene regulation, gut microbiota, hormonal regulation, and drug metabolism [83]. More broadly, translational predictivity remains poor, since more than 90% of therapies showing efficacy in preclinical animal models fail in human trials [82], and in GC specifically, several targeted therapies that showed promising results in xenograft and genetically engineered mouse models failed to improve overall survival in clinical trials [84]. Model establishment itself is also subtype-biased; diffuse-type GC, including signet-ring cell carcinoma, engrafts far less efficiently than intestinal-type tumors, likely due to lower tumor cellularity, which has historically limited the availability of animal models representative of this more aggressive subtype [78]. Finally, beyond questions of translational validity, animal models raise ethical concerns of their own. The 3Rs framework, Replacement, Reduction and Refinement, establishes that animal use in research should be replaced with suitable alternatives whenever possible, reduced to the minimum number of animals necessary, and refined to minimize suffering, and has

become an internationally recognized ethical standard governing the design of animal-based studies [85].

Clinical and epidemiological studies, though grounded in real patient data, face a limitation of a different nature, the disease's own lethality curtails observation. Because GC metastasis carries a poor prognosis regardless of the site involved, with median survival after metastatic diagnosis often measured in months, patients frequently die before the full trajectory of disease progression can be followed, truncating longitudinal data and limiting the ability of cohort studies to capture the complete natural history of metastatic spread [64].

3.2.5. The resulting gap

Despite the significant advances provided by current experimental and clinical models, no single platform is capable of comprehensively reproducing the complexity of GC metastasis. Existing *in vitro* models successfully isolate individual processes, such as migration, invasion, or ECM degradation, but fail to capture the sequential and dynamic nature of metastatic dissemination. Conversely, *in vivo* models reproduce the complete metastatic cascade but are limited by interspecies differences, reduced translational predictability and ethical constraints. Clinical and epidemiological studies provide invaluable insight into metastatic patterns and patient outcomes; however, their observational nature precludes mechanistic investigation and experimental manipulation.

Consequently, a gap remains between reductionist *in vitro* assays, complex animal models, and patient-derived clinical evidence. An ideal experimental platform should combine the controllability and reproducibility of *in vitro* systems with the physiological relevance of *in vivo* models, while preserving the human-specific characteristics of gastric cancer and allowing the different stages of the metastatic cascade to be investigated within a single integrated system. Addressing this challenge remains one of the major objectives in GC research.

4. Advanced *In Vitro* Models for Gastric Cancer Research

4.1. Organoids

Organoid technology has emerged as one of the most significant advances in tissue engineering and disease modelling over the past two decades. Organoids are three-dimensional multicellular structures generated *in vitro* from adult stem cells (ASCs), pluripotent stem cells (PSCs), or tissue-specific progenitor cells that possess the intrinsic ability to self-renew and self-organize into structures that resemble their tissue of origin [86, 87]. Unlike conventional two-dimensional cell cultures, organoids recreate key aspects of tissue architecture, cellular diversity, and physiological function while maintaining long-term proliferative capacity, thereby providing a more physiologically relevant model for studying human development and disease [88, 89].

The development of organoid technology was made possible by the identification of adult tissue stem cells capable of sustaining continuous epithelial renewal. A major breakthrough was achieved in 2009, when Sato and colleagues demonstrated that single Lgr5-positive intestinal stem cells embedded within an ECM substitute and cultured in the presence of a defined cocktail of niche factors could generate self-organizing crypt-villus structures that expanded indefinitely without the need for a mesenchymal niche [90]. This landmark discovery established the fundamental principles underlying organoid culture and paved the way for the successful establishment of organoids from numerous epithelial organs, including the stomach [91], liver [92], pancreas [93], lung [94] and prostate [95].

Depending on their cellular origin, organoids can be broadly classified into ASC-derived organoids and PSC-derived organoids, each reproducing different aspects of tissue biology [86]. ASC-derived organoids are established directly from tissue-resident stem cells and primarily model adult tissue homeostasis, regeneration, and disease, whereas PSC-derived organoids arise through directed differentiation of embryonic stem cells or induced pluripotent stem cells (iPSCs), allowing developmental processes and tissue morphogenesis to be recapitulated *in vitro* [87, 89]. More recently, this technology has been extended to tumor tissues, enabling the generation of patient-derived tumor organoids that faithfully preserve the genetic alterations, histopathological characteristics, and intratumoral heterogeneity of the original lesion [96, 97].

Following the establishment of organoid culture systems for multiple epithelial tissues, the technology was successfully adapted to the stomach, enabling the long-term

expansion of both normal gastric epithelium and gastric tumors [98, 99]. More recently, patient-derived gastric cancer organoids have become widely used in gastric cancer research, providing physiologically relevant models for studying tumor biology, molecular heterogeneity, and therapeutic response while maintaining many of the characteristics of the original tumor [97, 100].

4.2. Microfluidics

Beyond organoid technology, engineering-based strategies have also been developed to better recapitulate the physiological microenvironment *in vitro*. Among these, microfluidics has emerged as a particularly powerful tool. Microfluidics is the science and technology of manipulating fluids within channels with dimensions of tens to hundreds of micrometers, a field with considerable potential across chemical synthesis, biological analysis, and diagnostics [101, 102].

4.2.1 Organ-on-a-chip

Within biomedical research, this ability to precisely control fluid flow, spatial organization, and biochemical gradients at the microscale has been widely used to engineer more physiologically relevant *in vitro* systems [102]. As a direct application of microfluidic technology to tissue engineering, organ-on-a-chip (OoC) technology has emerged as one of the most promising microphysiological platforms for overcoming the limitations of conventional *in vitro* models while reducing the use of animal experimentation [102-104]. OoC platforms consist of micro-engineered devices containing living human cells cultured within perfusable microfluidic channels that recreate key structural, biochemical, and biomechanical features of native tissues [104, 105]. By integrating controlled fluid flow, mechanical stimulation, and tissue-specific microenvironments, these systems reproduce physiological conditions that are difficult to achieve using static culture models, allowing cellular behavior to be studied under conditions that more closely resemble those found *in vivo* (Figure 4) [105, 106]. These features make OoC platforms particularly attractive for modelling human diseases in which tissue mechanics, vascular interfaces, and multicellular communication play fundamental roles.

The versatility of OoC technology has led to its application across numerous physiological systems, including the lung [106], liver [107], intestine [108], kidney [109], and stomach [110], where tissue-specific functions have been successfully reproduced

under controlled microfluidic conditions. In particular, our group recently developed a bioinspired human stomach-on-a-chip that successfully recreated the architecture and mechanical environment of the human stomach by combining multilayer polydimethylsiloxane (PDMS) microfabrication with hydrogel-based tissue engineering strategies, reproducing physiological luminal flow and peristaltic-like mechanical stimulation [110, 111].

Importantly, the incorporation of vascular compartments, continuous perfusion, and tissue-specific microenvironments makes OoC technology particularly well suited to investigate dynamic processes involved in cancer progression, including tumor invasion, intravasation, extravasation, and metastatic colonization, which are difficult to reproduce using conventional *in vitro* models [103, 112].

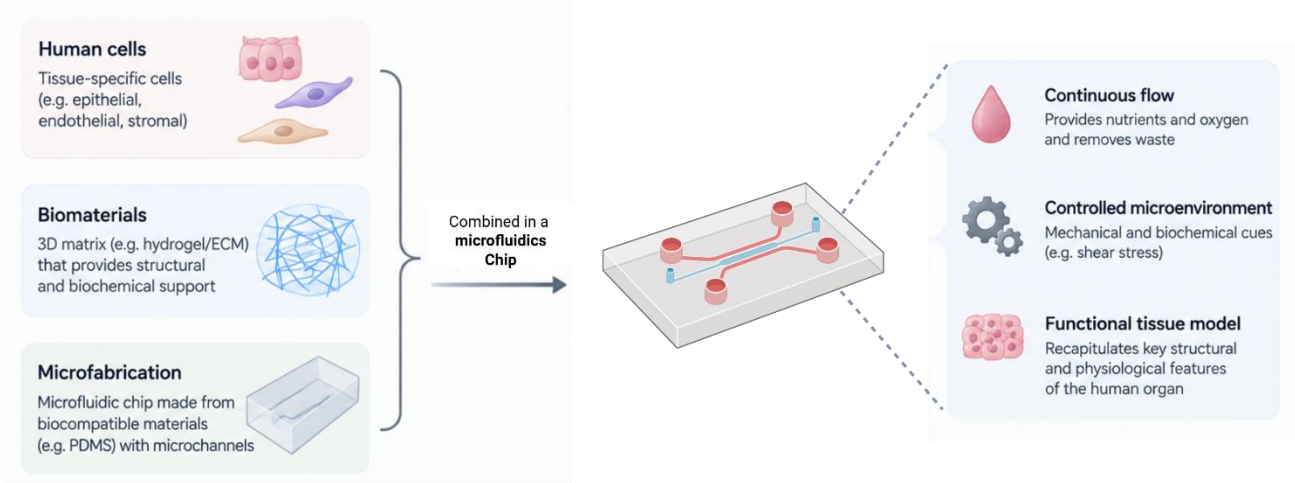


Figure 4. **Schematic representation of the main principles of Organ-on-a-Chip technology.** Organ-on-a-Chip systems integrate human cells, biomaterials, and microengineered fluidic compartments to recreate key structural and functional features of human tissues *in vitro*.

4.2.2. Multi-Organ-on-a-chip and Metastasis Modeling

Although still a relatively young technology, on-a-chip systems are already showing considerable promise for research and development applications. In recent years, systems of increased biological complexity, incorporating more than one organ or organoid within a single connected device, have begun to emerge. These multi-organoid devices, sometimes referred to as "body-on-a-chip" or "multi-organ-on-chip" (MoC) systems, hold considerably greater potential than single-organ platforms, though until

recently they relied primarily on cell lines and, in some cases, animal-derived cells rather than fully human systems [113].

Metastasis is a multistep process that depends on continuous interactions between the primary tumor, the vascular compartment, and distant organs, making isolated, single tissue models insufficient to reproduce disease progression. Consequently, the need to investigate inter-organ communication under physiologically relevant conditions has driven the development of MoC systems, specifically applied to the study of cancer metastasis.

A representative example of this approach is the multi-site metastasis-on-a-chip system, in which cancer cells were introduced into a microfluidic device connecting several distinct tissue compartments, allowing their relative preference for colonizing different organ sites to be assessed directly within a single platform [114]. More recently, a leaf-vein-inspired multi-organ microfluidic chip was developed to model breast cancer organotropism, connecting separate liver, bone and lung compartments and perfusing them with CTCs from different breast cancer subtypes, revealing distinct, organ-specific patterns of invasion and colonization consistent with the known metastatic preferences of each subtype [115]. Together, these platforms illustrate the core advantage of the MoC approach: unlike single-organ or *in vitro* systems, they allow organotropism itself, the differential tendency of cancer cells to metastasize to specific organs, to be studied directly and comparatively, under continuous circulatory connection between tissue compartments.

Dedicated multi-organ platforms tailored specifically to GC metastasis remain considerably scarcer, reflecting a broader gap in GC-specific microphysiological modelling. Multi-organ systems incorporating GC organoids do exist but have so far been directed primarily at systemic drug toxicity rather than metastatic dissemination. Co-culturing GC organoids with liver, kidney or heart modules, connected by fluidic channels that mimic systemic circulation and drug metabolism, has enabled the study of organ-specific toxicity mechanisms, such as liver-mediated metabolic activation dictating the local toxic exposure of matched intestinal tissue [116]. A recent review of this field explicitly describes the integration of GC organoids into such multi-organ-on-chip systems as the "next frontier" for assessing the systemic impact of oncological interventions, underscoring that this remains an emerging rather than an established application [116]. The closest work addressing metastatic dissemination is an organotypic three-dimensional model of the human peritoneum, established by co-culturing peritoneal mesothelial cells with fibroblasts embedded in collagen I and seeding

human GC cell lines onto its surface, which reproduced key morphological features of tumor adhesion, invasion, and growth into the peritoneal mesothelium [117]. While this model captures the target-organ side of peritoneal dissemination with considerable histological fidelity, it remains a static, non-perfused co-culture rather than a connected, circulating multi-organ system, underscoring the continued absence of a perfused, multi-compartment platform capable of modelling the complete GC metastatic route, from primary tumor through circulation to distant colonization, within a single integrated device.

II. Rationale and Aims

Metastatic dissemination is the principal determinant of GC mortality, and this dissemination is not random: intestinal- and diffuse-type GC follow distinct, subtype-specific metastatic routes, ranging from the hematogenous, liver-directed spread of IGC to the lymphatic and peritoneal dissemination characteristic of DGC. Despite decades of clinical oncology, two fundamental questions about these patterns remain unresolved, and the limitations presented by the current models available show us that they cannot be resolved with these tools.

The first concerns DGC. Patients with diffuse-type gastric cancer die rapidly, almost invariably from peritoneal carcinomatosis. It remains unclear, however, whether this rapid lethality reflects an intrinsic confinement of DGC cells to the peritoneal cavity, or whether these cells retain an equally real capacity to colonize distant organs that simply does not have time to manifest before the patient succumbs to local disease. This distinction carries clinical relevance beyond mechanistic interest. If peritoneal dissemination one day becomes preventable or controllable, understanding the latent organotropic potential of DGC cells could reveal where they would spread next, informing surveillance and treatment for a disease course not currently observed in the clinic.

The second concerns IGC. Here, patients frequently develop distant metastases, yet the biological basis for the preferential colonization of specific organs, such as the liver, lung, or bone, remains poorly understood. Identifying the factors that drive organ-specific colonization could inform site-directed surveillance strategies and the development of therapies tailored to prevent or treat metastasis at its most likely destinations.

Current experimental platforms are unable to resolve either question, each for a distinct reason. *In vitro* assays isolate individual cellular behaviors but cannot reproduce the full metastatic cascade. Animal models reproduce this cascade but are constrained by interspecies differences, limited translational predictivity, and ethical concerns. Clinical studies, though grounded in real patient data, are observational and cannot be manipulated to test mechanisms directly. Traditional models, both human and animal, share a further, more fundamental limitation: disease progression is invariably truncated by death. In the specific case of DGC, this means that both patients and xenografted animals typically succumb to peritoneal carcinomatosis before the full metastatic potential of diffuse-type cells can be observed, leaving the underlying question unresolved.

This raises a critical question: could a human gastric cancer avatar model, unconstrained by host survival, help elucidate the speed and patterns of GC dissemination beyond the point at which conventional models are limited?

By reproducing dynamic microenvironmental cues via hydrogel scaffolds and circulating flow, such a system would replicate a systemic response resembling the *in vivo* context, while allowing disease progression to be followed indefinitely, without being bound by the survival of a living host. As an initial, tractable step toward this goal, we hypothesize that a MoC system incorporating 3D spheroids derived from immortalized intestinal- and diffuse-type gastric cancer cell lines will effectively recreate the organ-specific metastatic pathways associated with each subtype (Figure 5).

This spheroid-based strategy was adopted as a reductionist proof-of-concept; the incorporation of patient-derived organoids, which would more closely capture the genetic and phenotypic heterogeneity of GC, remains a long-term objective. Beyond the mechanistic gap it addresses, this approach also aligns with the 3Rs framework, Replacement, Reduction, Refinement, offering a scientifically and ethically motivated alternative to the immunodeficient, xenograft-based animal models that currently dominate GC metastasis research.

To address this hypothesis, we defined the following objectives, which guided the design, validation, and application of our platform:

I. Design and fabrication of a prototype MoC combining a primary tumor site connected by an artificial vasculature to multiple metastatic sites.

II. Establishment and characterization of 3D spheroid models derived from immortalized intestinal- and diffuse-type gastric cancer cell lines.

III. Development and optimization of chip surface functionalization and endothelialization strategies to reconstitute a functional artificial vasculature within the device.

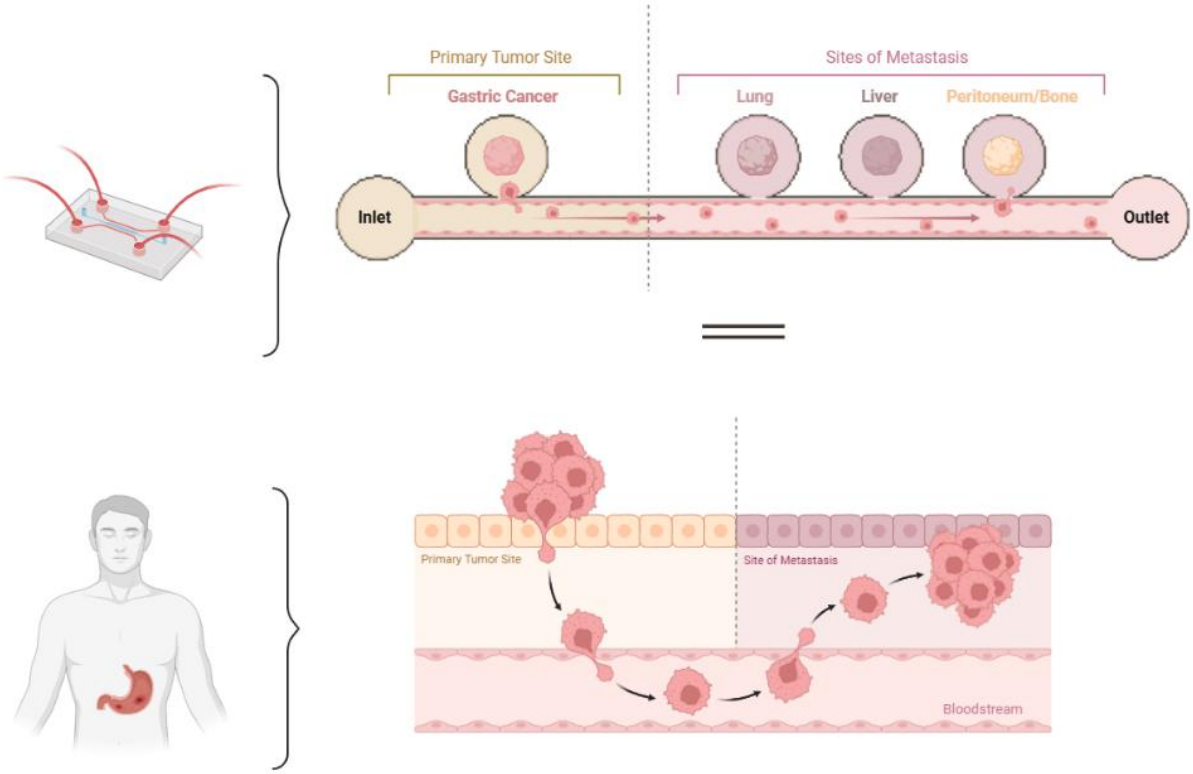


Figure 5. **Conceptual overview of the MetaCHIP platform.** The upper panel illustrates the idea of the MetaCHIP design, comprising a primary gastric tumor compartment connected through a perfusable vascular channel to organ-specific metastatic niches, enabling the study of tumor cell dissemination under dynamic flow conditions. The lower panel depicts the corresponding metastatic cascade *in vivo*, highlighting the sequential steps of tumor cell intravasation, circulation through the bloodstream, extravasation and colonization of distant organs.

III. Materials and Methods

1. Engineering

1.1. Microfluidic Device Design

The microfluidic platform used throughout this study, designated MetaCHIP, was designed to recapitulate the organ-specific metastatic dissemination of gastric cancer in a physiologically relevant microenvironment. The device consisted of three or four independent tissue chambers interconnected by a central perfusable microfluidic channel intended to mimic the vascular compartment. The three-chamber configuration was used for initial optimization experiments, given its simpler geometry, while the four-chamber configuration, comprising one primary tumor compartment and three metastatic target-organ compartments, represents the intended final architecture of the platform. This configuration enables continuous communication among multiple metastatic target tissues while maintaining spatial separation among the different organ equivalents.

The device architecture was designed using computer-aided design (CAD) software and underwent several optimization steps before reaching the final configuration (MetaCHIPv3 – MetaCHIPv4 - MetaCHIP v5). Successive design iterations focused on improving hydrogel confinement, minimizing leakage during gel loading, facilitating endothelialization of the vascular channel, and ensuring homogeneous perfusion throughout the device.

1.2. Flow, Shear Stress and Culture-Medium Permeation Simulation

The final chip geometry (50 × 24 mm footprint; 2 mm-wide, 36 mm-long main channel; two 4 mm-diameter access ports; three 4 mm-diameter Matrigel chambers, MetaCHIPv5) was reconstructed from the original vector CAD drawing, as the simulation software did not support direct import of CAD files. The geometry was therefore discretized into a binary mask on a uniform Cartesian grid (dx = 100 µm), distinguishing the open fluid path (main channel and inlet/outlet ports) from the Matrigel-filled culture chambers (Figure 6). This mask defined the flow and transport domains used in all subsequent numerical simulations.

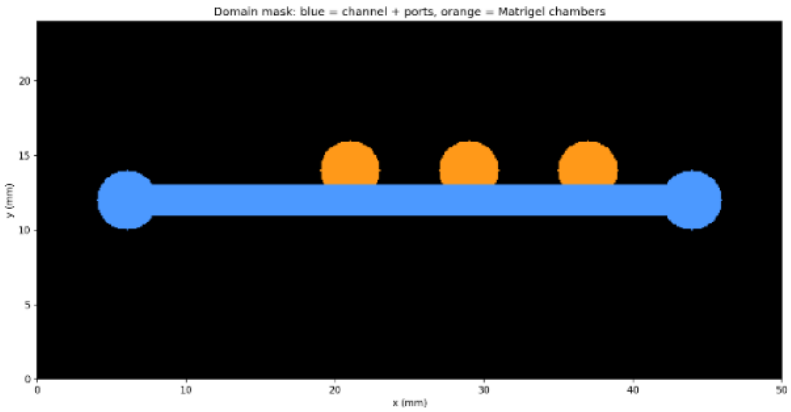


Figure 6. Reconstructed chip mask. Blue: main channel and inlet/outlet ports (open fluid path); Orange: Matrigel-filled culture chambers.

Flow simulations assumed that fluid was injected and collected from left to right, respectively, through a 20-gauge connector positioned at the center of each access port, rather than across the full port cross-section, matching the future experimental perfusion setup. Mass conservation was verified by confirming a constant volumetric flow rate across multiple cross-sections of the straight channel.

The lateral velocity profile was computed from the exact rectangular-duct solution for pressure-driven laminar flow (channel cross-section 2 mm x 0.5 mm, aspect ratio 4:1), evaluated on a fine analytical grid independent of the numerical mesh to guarantee exactly zero velocity at the true channel side walls.

Permeation of the culture medium into the Matrigel chambers was modelled with a fixed time step of 30 s over a 3 h simulated period. A free-solute diffusivity of 6.7×10^{-10} m²/s (representative of small culture-medium solutes in water at 37 °C) was assumed, reduced by a hindrance factor of 0.5 inside the Matrigel chambers. Dirichlet concentration boundary conditions (C/C_source) were imposed at both needle-centered port boundaries, consistent with the pressure boundary conditions used in the flow calculation. Spatial concentration maps were simulated at eight representative time points spanning the 3 h simulated perfusion period.

Wall shear stress was estimated from the local depth-averaged velocity using the parallel-plate (Hele-Shaw) approximation, $\tau = 6\mu U/h$, where U is the local depth-averaged speed, μ is the cell-culture medium viscosity, and h is the channel height (500 μm). In the straight-channel section, the classical closed-form expression $\tau = 6\mu Q/(h^2 w)$ was used, where Q is the flow rate, and w is the channel width.

Table 4. **Input parameters and computed wall shear stress values.**

Parameter	Value
Viscosity, μ	0.77 ± 0.07 mPa·s
Flow rate, Q	4.0 μL/min
Channel height, h	500 μm
Channel width, w	2 mm
$\tau = 6\mu Q/(h^2 w)$ (formula)	Calculated numerical value - 0.6160 mPa

1.3. Fabrication of the Device

The MetaCHIP microfluidic devices were fabricated using a rapid xurography-based prototyping approach adapted from the methodology previously described by Ferreira *et al.* (2021), eliminating the need for conventional photolithographic fabrication and clean-room facilities [111] (Figure 7).

The microfluidic layout was first designed using CAD software and transferred to 500 μm-thick PDMS sheets, which were cut using a ROLAND VersaSTUDIO GS2-24 cutting plotter. The cutting process generated the complete microfluidic architecture, including the perfusion channel, tissue chambers, and auxiliary structures required for hydrogel confinement. Following cutting, the patterned PDMS layer was manually removed from the surrounding material, thoroughly washed with isopropanol to remove residual debris generated during the cutting process, and dried with compressed air. A second PDMS layer was produced by mixing the silicone elastomer base and curing agent (Sylgard 184, Sigma-Aldrich, USA) at a 10:1 (w/w) ratio. The mixture was manually homogenized using a spatula and centrifuged (3900 rpm, 18 °C, 5 min) to remove entrapped air bubbles. Approximately 30 mL was then poured onto a Petri dish and was subsequently cured at 70 °C for 1 h. Before device assembly, microscope glass slides were cleaned sequentially by sonication in Hellmanex® detergent solution (Hellma Analytics, Germany), acetone, and ultrapure water for 5 min each, then dried under compressed air and stored in sterile Petri dishes until use.

To ensure irreversible bonding between the PDMS layers and between PDMS and glass, oxygen plasma activation was performed using a Tergeo Plasma Cleaner (PIE Scientific, USA), using an O2 PDMS recipe (20 W power, 30% duty ratio, 5.0 sccm O_2 flow, 2 min duration, direct mode). This treatment generates reactive silanol (Si-OH) groups on the

exposed PDMS surfaces by oxidizing the native methyl (Si-CH_3) groups of the polymer. When two plasma-activated PDMS surfaces are brought into contact, these silanol groups condense to form covalent siloxane (Si-O-Si) bonds, resulting in an irreversible PDMS–PDMS seal [118]. The same principle applies to PDMS–glass bonding, since glass surfaces are also rich in silanol groups. Plasma-activated PDMS placed in contact with a glass slide undergoes an analogous condensation reaction, forming covalent siloxane bonds directly between the PDMS and the silica network of the glass [119].

Two sequential plasma treatments were carried out: the first to bond the patterned PDMS layer to the cast PDMS substrate (PDMS–PDMS), followed by a second plasma activation to bond the assembled device onto the glass microscope slide (PDMS–glass). Before the second bonding step (PDMS–glass), 20-gauge needles (Instech Laboratories, USA) were used to form the fluidic inlet and outlet ports, and compartments were created with sterile 4 mm biopsy punches (Kai Medical, Japan) (Figure 5).

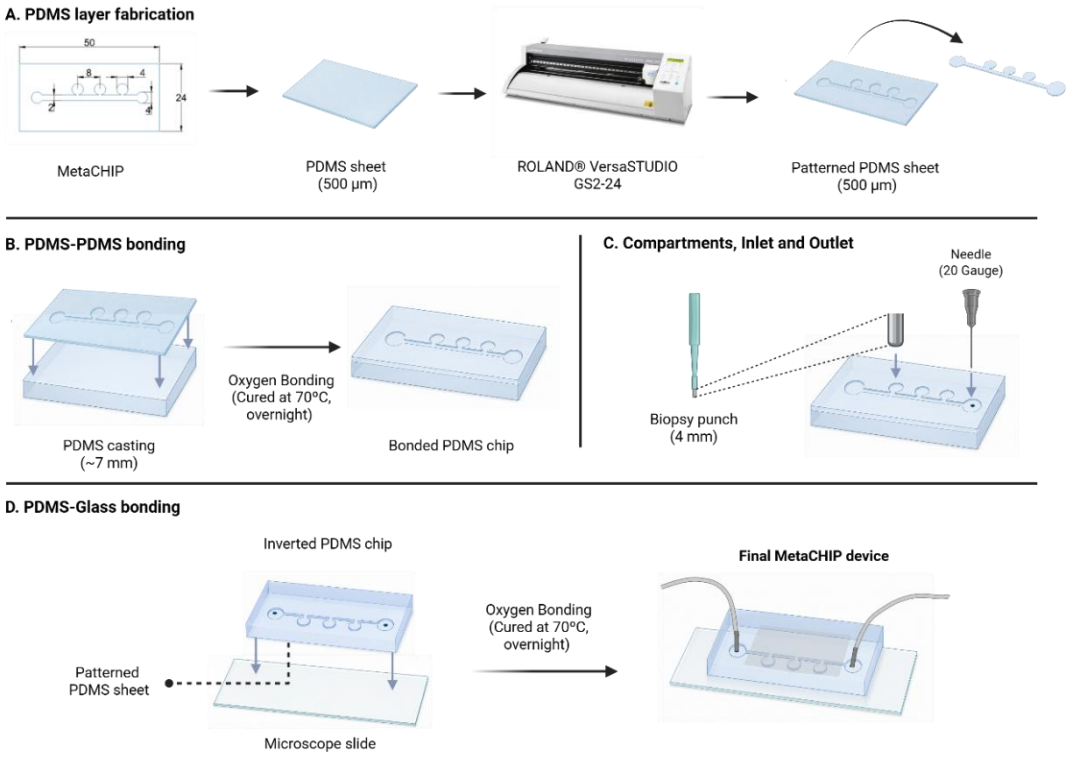


Figure 7. **Fabrication workflow of the MetaCHIP device.** (A) PDMS layers were fabricated by casting PDMS sheets (500 µm thickness) and patterning them using a ROLAND VersaSTUDIO GS2-24 cutting plotter. (B) The patterned PDMS sheet was bonded to a thicker PDMS casting layer (~7 mm) via oxygen plasma treatment, followed by curing at 70°C overnight to produce the bonded PDMS chip. (C) Tissue compartments were created using 4 mm biopsy punches, and inlet/outlet ports were formed using 20-gauge needle adapters. (D) The bonded PDMS chip was inverted and irreversibly sealed onto a glass microscope slide via oxygen plasma bonding, followed by curing at 70°C overnight, yielding the final assembled MetaCHIP device.

1.4. System Assembly

The microfluidic perfusion system was assembled by connecting a pressure-driven flow control unit to the MetaCHIP device, enabling precise and reproducible delivery of culture medium. Air pressure was regulated using an OB1 MK3 pressure controller (Elveflow, France), coupled with a flow sensor (Elveflow, France) that provided real-time monitoring and closed-loop flow-rate control, ensuring stable perfusion conditions over extended culture periods. Culture medium was housed in a 50 mL Falcon tube reservoir, sealed with a dedicated pressure cap (Elveflow, France) adapted to the tube, which allowed the reservoir headspace to be pressurized while maintaining a closed system. The pressure controller was connected to the reservoir using Tygon ND-100-65 Class VI tubing (2.4 mm ID, 5.6 mm OD, 1.6 mm wall thickness; Saint-Gobain, France). Medium was delivered from the reservoir to the chip inlet, and from the chip outlet to a waste reservoir (50 mL Falcon tube), using BTPE-90 polyethylene tubing (0.86 × 1.27 mm ID/OD; Instech Laboratories, USA). Tubing connections to the chip inlet and outlet were made using 20-gauge straight and 90° connectors (Instech Laboratories, USA), allowing secure, leak-free interfacing between the tubing and the microfluidic device.

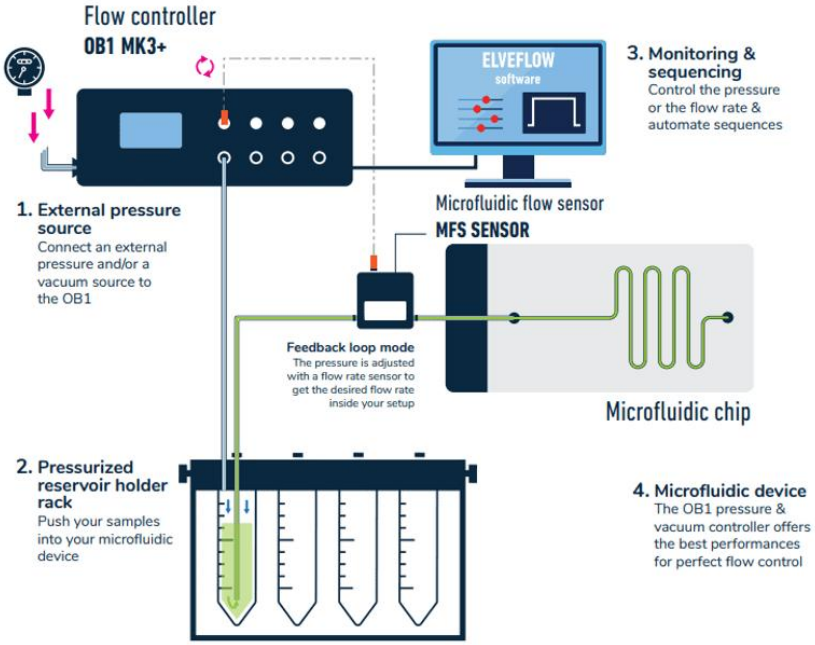


Figure 8. **Schematic representation of the pressure-driven microfluidic flow control system (Elveflow, France) used to perfuse the MetaCHIP device**. The setup comprises: (1) an external pressure source connected to the OB1 MK3 flow controller; (2) a pressurized reservoir holder rack accommodating the sample reservoir; (3) the Elveflow software for pressure/flow-rate control and sequence automation; and (4) an MFS flow sensor operating in feedback-loop mode, adjusting the applied pressure in real time to maintain the desired flow rate through the microfluidic chip. Adapted from Elveflow [120].

Flow generation relies on a pressurized reservoir mechanism. The pressure controller applies gas pressure to the headspace of the sealed reservoir, driving the medium through the outlet and into the tubing. Since flow rate is directly determined by the applied pressure, it can be finely tuned via pressure adjustment. This piezoelectric-based regulation offers fast response, high stability, and, unlike syringe pumps, which are limited by syringe volume, supports larger fluid volumes over extended culture periods [120]. Pressure and flow rate targets were set and monitored via the Elveflow software coupled to a thermal flow rate sensor (Elveflow, France).

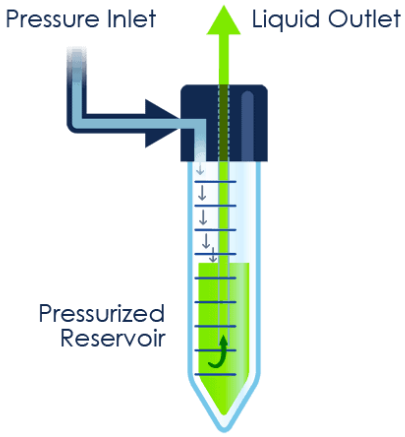


Figure 9. **Schematic representation of the pressurized-reservoir principle.** Gas pressure applied to the reservoir headspace acts on the liquid surface, driving medium flow through the outlet toward the microfluidic chip. Adapted from Elveflow [120].

1.5. Technological validation

The fabricated MetaCHIP devices underwent a series of technological validation assays to assess their structural integrity and functional performance. These validation experiments were designed to verify the reproducibility of the fabrication process, the integrity of the assembled multilayer structure, the efficiency of hydrogel confinement, and the ability of the platform to support fluid transport between the perfusion channel and the tissue chambers. The technological validation workflow comprised structural integrity assessment, leakage evaluation, and diffusion characterization before subsequent biological experiments.

1.5.1. Structural Integrity Assessment

Following fabrication and assembly, each MetaCHIP device was carefully inspected under the naked eye and microscopy to evaluate its structural integrity. Particular attention was given to the quality of the PDMS–PDMS and PDMS–glass bonds to ensure complete sealing of the microfluidic architecture and the absence of air gaps or delamination between layers. The geometry and uniformity of the tissue chambers and perfusion channel were also examined to verify that all microfluidic structures were correctly formed and suitable for subsequent hydrogel loading and perfusion experiments.

1.5.2. Hydrogel Confinement Assessment

To evaluate the ability of the MetaCHIP platform to spatially confine the extracellular matrix within the designated tissue chambers, hydrogel confinement assays were performed. Matrigel (Corning, USA) was introduced into the tissue compartments, while the central perfusion channel was kept free of hydrogel. Following gel loading, the devices were incubated under standard cell culture conditions to allow complete polymerization of the matrix. Confinement was assessed by visual inspection, evaluating whether the Matrigel settled uniformly at the bottom of each chamber, since preferential wetting of the chamber walls was found to compromise the formation of a well-defined hydrogel structure, and whether any hydrogel leaked into the central perfusion channel, which would compromise the intended spatial separation between the vascular compartment and the tissue chambers.

1.5.3. Leakage Assessment

To evaluate the fluidic integrity of the fabricated devices, leakage tests were performed following device assembly and bonding. A colored aqueous solution was introduced through the fluidic inlet until complete filling of the central perfusion channel, and the interconnected microfluidic structures were achieved. Different compartment sealing strategies were evaluated during device optimization, including PCR optical sealing film (MicroAmp™, Applied Biosystems, USA) and low-volume displacement caps (Microfluidic ChipShop GmbH, Germany), to determine their ability to prevent leakage from the tissue compartments under continuous perfusion. The devices were

subsequently maintained under continuous perfusion at 3 mbar for 16–24 h, after which they were visually inspected to assess the presence of fluid leakage to the external environment or across the PDMS interfaces.

1.5.4. Matrigel Diffusion Assessment

To evaluate the ability of the MetaCHIP platform to support passive fluid transport between the perfusion channel and the tissue compartments, diffusion assays were performed following hydrogel confinement. Approximately 20–30 µL of Matrigel was loaded into each tissue chamber and allowed to polymerize under standard cell culture conditions (37ºC, 5%CO_2). Subsequently, a colored aqueous solution was continuously perfused, under 3 mbar, through the central microfluidic channel, and the progression of diffusion into the surrounding hydrogel was monitored over time.

Images were acquired at predefined time points until the colored solution had diffused throughout the hydrogel-filled compartments. The temporal progression of diffusion was subsequently quantified using Fiji (ImageJ, National Institutes of Health, USA) by measuring the percentage of hydrogel area reached by the colored solution at each time point.

2. Validation of the Biological Model

Before incorporating multiple tissue types into the MetaCHIP platform, multiple biological validation experiments are needed to establish the optimal culture conditions for each cellular component and to develop a robust proof-of-principle of the platform using established human cell lines. These experiments included the optimization of gastric cancer spheroid generation, the characterization of spheroid viability and metabolic activity, the optimization of endothelialization of the vascular compartment, and the characterization of the additional cell types incorporated into the platform. Collectively, these studies established the experimental framework required for the implementation of the multi-organ model and validated the feasibility of the proposed platform. Once this proof-of-principle has been established using conventional cell lines, future developments of the MetaCHIP platform will focus on the incorporation of patient-derived

organoids (PDOs) to generate a more physiologically relevant and patient-specific model for investigating gastric cancer metastasis.

2.1. Cell Culture

Human cell lines representative of the primary tumor, vascular compartment, and target metastatic tissues were selected to establish the MetaCHIP platform. MKN-74 and MKN-45 cells were used as models of intestinal- and diffuse-type gastric cancer, respectively, while HUVEC-C, HepaRG, BEAS-2B, and SGBS cells were used to represent the endothelial barrier and the liver, lung, and adipose tissue compartments. In particular, SGBS preadipocytes were selected to model the omental/peritoneal adipose tissue, a major site of peritoneal metastatic seeding in DGC, where milky spots, specialized lymphatic structures embedded within adipose-rich omental tissue, serve as primary entry points for disseminating tumor cells [121]. The culture conditions for each cell line are summarized in Table 5.

Most culture media were purchased from Gibco (Thermo Fisher Scientific, USA) and supplemented with 10% (v/v) fetal bovine serum (FBS) (Gibco, Thermo Fisher Scientific, USA) and 1% (v/v) penicillin–streptomycin (Pen/Strep) (Gibco, Thermo Fisher Scientific, USA). Cells were maintained at 37 °C in a humidified atmosphere containing 5% CO_2 and routinely passaged upon reaching approximately 80–90% confluence. Since all tissue compartments within the MetaCHIP platform are interconnected through a common perfusion circuit, all cell lines were progressively adapted to a common F-12K (Gibco, Thermo Fisher Scientific, USA) culture medium to enable long-term multi-organ co-culture under shared perfusion conditions.

Two cell types required specific culture adaptations beyond this common protocol. HUVEC-C cells were routinely expanded on culture flasks pre-coated with 2% (w/v) gelatin (Sigma-Aldrich, Merck, Germany), and their F-12K medium was further supplemented with heparin (10 mg/mL; Cat. No. H3149, Merck, Germany) and endothelial cell growth supplement (ECGS) (Cat. No. 356006, Corning, USA) to promote endothelial proliferation and preserve the characteristic endothelial phenotype.

SGBS preadipocytes, in turn, were cultured in F-12K supplemented with biotin (3.3 mM; Merck, Germany) and D-pantothenate (1.7 mM; Merck, Germany). Differentiation into mature adipocytes followed a two-step protocol adapted from established SGBS differentiation methods. Once cells reached ~70% confluence, they were first maintained for 4 days in Quick Diff medium, consisting of the basal medium (without FBS)

supplemented with 20 nM insulin, 100 nM cortisol, 0.2 nM triiodothyronine (T3), 25 nM dexamethasone, 250 μM 3-isobutyl-1-methylxanthine (IBMX), and 2 μM rosiglitazone, with medium replacement every 2 days. This combination of adipogenic inducers acts synergistically to activate key transcriptional regulators of adipogenesis, including PPARγ and C/EBPα, driving preadipocytes toward terminal differentiation. From day 4 onwards, the differentiation medium was replaced with 3FC medium containing 20 nM insulin, 100 nM cortisol, and 0.2 nM T3, which was renewed every 2 days until the desired stage of adipocyte differentiation was reached, a process that takes approximately 14 days and is typically accompanied by progressive intracellular lipid droplet accumulation.

Table 5. **Human cell lines and culture conditions used in this study**

Cell Line	Origin/Tissue	Role in the MetaCHIP	Original culture medium	Unified culture medium
MKN-74	Human gastric adenocarcinoma	Primary tumor model	RPMI-1640	F-12K
MKN-45	Human gastric adenocarcinoma	Primary tumor model	RPMI-1640	
HUVEC-C	Human umbilical vein endothelial cells	Endothelial vascular compartment	F-12K	
BEAS-2B	Human bronchial epithelial cells	Lung metastatic niche	DMEM	
HepaRG™	Human hepatic progenitor cells	Liver metastatic niche	William's E Medium	
SGBS	Human preadipocytes	Adipose tissue compartment	DMEM/F-12	

2.2. Gastric Cancer Spheroids

2.2.1. Agarose Molds

Agarose microwell molds were prepared using MicroTissues® 3D Petri Dish® micromolds (Sigma-Aldrich, USA) according to the manufacturer's instructions with minor modifications (Figure 10).

I. A sterile 2% (w/v) agarose solution was prepared by dissolving Ultrapure Grade Agarose (MB05202, NZYTech, Portugal) in 0.9% (w/v) NaCl.
II. The agarose solution was heated until completely dissolved and maintained in a molten state at approximately 70 °C to prevent premature gelation.
III. The surface of the sterile MicroTissues® 3D Petri Dish® micromold was disinfected with 70% (v/v) ethanol inside a Class II biological safety cabinet and allowed to air dry completely.
IV. 500 µL of molten agarose was carefully dispensed into the center of the micromold, ensuring complete filling of all microwell features while avoiding bubble formation.
V. The agarose was allowed to polymerize at room temperature for 10–20 min.
VI. Once fully polymerized, the agarose mold was gently removed from the template and transferred into an individual well of a sterile 12-well tissue culture plate.
VII. Approximately 2 mL of the appropriate complete culture medium was added to each well to immerse the agarose mold fully.
VIII. The molds were equilibrated overnight at 37 °C in a humidified incubator containing 5% CO_2 before cell seeding.

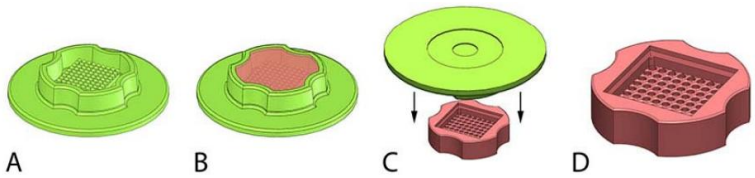


Figure 10. **Preparation of agarose microwell molds using the MicroTissues® 3D Petri Dish® micromold.** (A) Reusable positive micromold containing an array of microwells. (B) Casting of molten agarose into the micromold. (C) Separation of the solidified agarose mold from the positive template after polymerization. (D) Final agarose microwell mold used for gastric cancer spheroid formation. Adapted from the manufacturer's instructions (MicroTissues® 3D Petri Dish®, MicroTissues Inc.).

2.2.2. Cell seeding

To establish a proof-of-principle model for the MetaCHIP platform, gastric cancer spheroids were generated using two human gastric adenocarcinoma cell lines representative of the two major histological subtypes described by Laurén: MKN-74, representing the intestinal-type GC, and MKN-45, a widely used model exhibiting characteristics of diffuse-type GC. The use of both cell lines enabled the establishment of subtype-specific three-dimensional models for the subsequent optimization and biological validation of the platform.

The initial seeding density was determined according to the manufacturer's recommendations for the MicroTissues® 3D Petri Dish® micromold, which correlates the total number of seeded cells with the expected spheroid diameter (Table 6). Based on this information, 32,000 and 256,000 cells were seeded per agarose mold (190 µL), corresponding to nominal spheroid diameters of approximately 100 µm and 200 µm, respectively. The selection of these two spheroid sizes was because of the work done by Rocha et al., who identified this number of cells per spheroid as appropriate [122]. Comparing spheroids of different sizes also enabled the identification of the most suitable configuration for subsequent incorporation into the MetaCHIP platform.

Table 6. **Cell seeding densities used for gastric cancer spheroid generation.** Adapted from the MicroTissues® 3D Petri Dish® manufacturer's protocol.

12-well plate Small spheroids: 256 #12-256		
*Spheroid diameter (µm)	~Cells/spheroid	Total cells seeded (cells/190µl)
50	15	3,840/190 µL
100	125	32,000/190 µL
150	421	107,000/190 µL
200	1,000	256,000/190 µL
250	1,953	500,000/190 µL
300	3,375	860,000/190 µL

*These are estimates only. Estimates of spheroid diameter are based on the following assumptions, i.) diameter of input cells is 20µm (4,180µm3), ii.) total spheroid volume equals cell volume times the number of input cells, iii.) the spheroid is a perfect sphere and, iv.) cells are perfectly distributed to all recesses. In practice, spheroid size and shape will vary depending on cell type.

The cell seeding procedure was performed as follows:

I. MKN-74 and MKN-45 cells were cultured until approximately 80–90% confluence.

II. Cells were washed with sterile phosphate-buffered saline (PBS), detached using TrypLE, neutralized with complete culture medium, and collected by centrifugation. Viable cells were counted and resuspended to prepare suspensions containing either 32,000 or 256,000 cells in 190 µL of complete culture medium.

III. The equilibration medium surrounding the agarose mold and the residual medium within the central seeding chamber were carefully removed.

IV. A volume of 190 µL of the prepared cell suspension was gently dispensed into the center of each agarose mold, ensuring uniform distribution across the microwells.

V. The molds were left undisturbed for approximately 10 min to allow the cells to sediment into the individual microwells.

VI. Approximately 2.5 mL of complete culture medium was then carefully added to the surrounding well without disturbing the seeded cells.

VII. The culture plates were incubated at 37 °C in a humidified atmosphere containing 5% CO_2, allowing the cells to spontaneously aggregate and form a single spheroid within each microwell (Figure 11).

VIII. The culture medium was replaced every 2–3 days until spheroid harvesting.

As illustrated in Figure 11, individual cells sediment into the agarose microwells, where they progressively aggregate and compact through cell-cell interactions, ultimately giving rise to a single spheroid within each microwell.

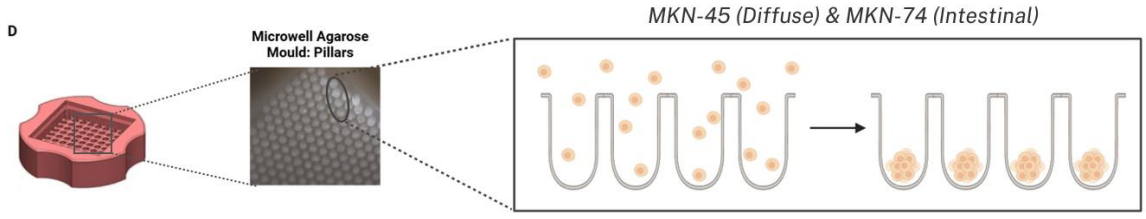


Figure 11. **Schematic representation of gastric cancer spheroid formation using the MicroTissues® 3D Petri Dish® agarose micromold.** Cell suspensions of MKN-74 and MKN-45 are seeded into the agarose microwells, where cells settle by gravity and progressively self-assemble into a single compact spheroid within each microwell. Adapted from the MicroTissues® 3D Petri Dish® manufacturer's protocol.

2.2.3. Spheroid Harvest

Upon completion of spheroid formation, gastric cancer spheroids were recovered from the agarose micromolds for subsequent experimental applications. Since spheroids remain non-adherent within the agarose microwells, they can be harvested without enzymatic treatment, thereby preserving their three-dimensional architecture and cell-cell interactions. The harvesting procedure was performed as follows:

I. The cell culture medium surrounding the agarose mold was removed.
II. The mold was lifted with a sterile spatula and inverted over a well containing fresh medium.
III. The mold was left undisturbed to allow spheroid release by gravity.
IV. Harvested spheroids were transferred to a sterile Eppendorf tube and allowed to settle by gravity; if sedimentation was insufficient, a brief centrifugation step was performed instead.
V. The supernatant was carefully removed, and the spheroid pellet was resuspended in 40 µL of Matrigel.
VI. A 24-well plate was pre-warmed at 37 °C before embedding.
VII. The spheroid–Matrigel suspension was pipetted onto the pre-warmed 24-well plate.
VIII. The plate was immediately inverted to allow the formation of a well-defined Matrigel dome and to promote even distribution of the spheroids throughout the matrix.
IX. The Matrigel was allowed to solidify before the plate was returned to its upright position, and then 1 mL of culture medium was added to each well.

2.2.4. Spheroid Growth Assessment

Spheroid growth was monitored over time by acquiring brightfield images at predefined time points ([Day 0, 1, 3, 5...]). Spheroid area was subsequently measured from these images using Fiji (ImageJ, National Institutes of Health, USA), and the resulting measurements were compared across conditions and time points to assess the growth kinetics of the IGC and DGC spheroids.

2.2.5. Spheroid Viability

Spheroid viability was assessed using the Live/Dead™ Viability/Cytotoxicity Kit (Ref. L3224, Invitrogen, Thermo Fisher Scientific, USA), which distinguishes live from dead cells based on intracellular esterase activity (calcein-AM, green) and plasma membrane integrity (ethidium homodimer-1, red). A staining mix was prepared in PBS according to the manufacturer's instructions. Culture medium was removed from the wells, and spheroids were washed three times with PBS for 5 min each before the staining solution was added. While the manufacturer's protocol recommends a 30 min incubation, this was extended to 2 h, protected from light, to ensure the staining solution penetrated throughout the spheroid. Spheroids were subsequently washed once with PBS for 5 min, and fresh medium was added before imaging by confocal microscopy with a Leica TCS SP5 (Leica Microsystems, Germany).

2.3. Functional Characterization Assays

2.3.1. Metabolic Activity

Metabolic activity was assessed using a resazurin-based fluorometric assay and, where indicated, in parallel with a sulforhodamine B (SRB) colorimetric assay for total biomass estimation, based on the protocol described by Silva et al. [123]. A resazurin stock solution was prepared by dissolving 1 mg of resazurin sodium salt (Sigma-Aldrich, Merck, USA) in 1 mL of sterile PBS, filtering through a 0.2 µm filter, and storing at −20 °C until use. On the day of the assay, the stock solution was thawed and diluted 1:100 in complete culture medium to obtain a 10 µg/mL working solution.

For gastric cancer spheroids, cultures were incubated with the resazurin working solution for 6 h at 37 °C, after which ~80 µL of the resazurin-containing medium was collected from each well and transferred to a 96-well plate, alongside a blank control consisting of resazurin working solution in culture medium without spheroids. Fluorescence was measured using a SpectraMax microplate reader (excitation 540 nm/emission 590 nm).

To assess the compatibility of the different cell lines with the unified F-12K culture medium, cells were seeded in 96-well plates (50,000 cells/well, in triplicate) and cultured for 48 h in either the original culture medium (DMEM), the unified medium (F-12K), or

DMEM/F-12. Cells were then incubated with the resazurin working solution for 2 h at 37 °C, and fluorescence was measured directly by placing the plate in the SpectraMax microplate reader (excitation 540 nm/emission 590 nm). SRB staining was subsequently performed on the same plate to estimate total cell mass, based on the protocol described by Silva et al. [123]. Briefly, following the resazurin assay, the culture medium was removed, and cells were washed once with PBS. Cells were then fixed by adding 1% (v/v) acetic acid in methanol to each well and incubating at −20 °C for at least 3 h (or overnight) to promote fixation. The fixative solution was discarded, and the plate was dried at 37 °C for 1 h. SRB solution (Sigma-Aldrich, Merck, USA) was then added to each well and incubated for 1 h at 37 °C, after which the SRB solution was discarded, and wells were washed with 1% acetic acid prepared in Milli-Q-purified water. The plate was dried again at 37 °C for 1 h (or overnight), and the bound dye was solubilized with 10 mM Tris-NaOH (pH 10) under agitation on an orbital plate shaker for 30 min at room temperature. Absorbance was read at 510 nm, with background measurement at 620 nm.

2.3.2. Immunofluorescence

Immunofluorescence assays were performed primarily to test and validate the performance of selected antibodies and probes, namely the SiR-Actin (Spirochrome AG, Switzerland) probe and the anti-CD31 antibody (Invitrogen, Thermo Fisher Scientific, USA). In parallel, these assays also served as a structural validation tool, confirming the expected morphological and phenotypic features of the biological entities incorporated into the platform.

For gastric cancer spheroids, samples were fixed with methanol for 20 min on ice. Following fixation, cells were washed with PBS, and non-specific binding was blocked with 5% BSA for 30 min. Spheroids were then incubated with SiR-Actin (0.1 µM) for 2 h to label the actin cytoskeleton, followed by nuclear counterstaining with DAPI (1:1000) (Sigma-Aldrich, USA) for 30 min.

For HUVEC-C, cells were seeded on glass coverslips within the culture wells pre-coated, and fixed with 4% paraformaldehyde (PFA) (Electron Microscopy Sciences, USA) for 20 min at room temperature. Following fixation, cells were washed with PBS and incubated with 50 mM NH_4Cl for 10 min to quench residual aldehyde groups, washed again, and permeabilized with 0.2% Triton X-100 for 5 min. After a further PBS wash, non-specific binding was blocked with 5% BSA for 30 min. Cells were then incubated overnight at 4

°C, protected from light, with a primary antibody against CD31 (PECAM-1) (1:200; 5 µg/mL), followed by PBS washes and incubation with an AlexaFluor 488-conjugated secondary antibody (Invitrogen, Thermo Fisher Scientific, USA) (1:500) for 2 h at room temperature, protected from light. Nuclei were counterstained with DAPI (1:1000) (for 5 min prior to imaging.

In a separate experiment aimed at testing the SiR-Actin probe, HUVEC-C cells were seeded on fibronectin-coated coverslips only and processed following the same protocol described above, with the addition of SiR-Actin (0.1 µM) co-incubated with the secondary antibody for 2 h.

2.4. Endothelialization of the vascular compartment

2.4.1. Coating Optimization

Before endothelialization of the microfluidic device, a coating optimization assay was performed to determine the most suitable substrate for HUVEC-C attachment and morphology. Cells were seeded in 12-well plates (50,000 cells/well, in duplicate) on coverslips pre-coated with fibronectin, widely used as a coating substrate for endothelial cell culture [124], gelatin, routinely used for HUVEC-C maintenance, or left uncoated, and monitored for 72 h. Coating performance was assessed by immunofluorescence staining against CD31, as described in Section 2.3.2. Based on this assessment, fibronectin was selected as the coating condition for subsequent endothelialization experiments.

2.4.2. Chip Endothelialization

Before endothelialization, all materials required for chip assembly, adhesive sealing film, scissors, tubing, connectors, the microfluidic chip, and syringe adapters, were sterilized under UV light for at least 20 min. The experimental setup used for chip perfusion and endothelialization, including the syringe, syringe adapter, tubing, 90° connectors, microfluidic chip, and waste reservoir, is shown in Figure 12.

The chip assembly and endothelialization procedure was performed as follows:

I. Connectors were inserted at a 90° angle into the inlet and outlet ports of the chip.
II. Two segments of tubing (approximately 5–7 cm) were cut and connected to both connectors.
III. A syringe fitted with an adapter was attached to the inlet tubing.
IV. A 50 mL Falcon tube was attached to the outlet tubing to serve as a waste reservoir.
V. The chip was washed with ethanol for 20 min, with the compartments left uncovered (without sealing film).
VI. Ethanol was removed from the chip and compartments, which were then left to air-dry.
VII. The compartments were washed three times with PBS, 5 min per wash.
VIII. The channel was washed three times with PBS, 5 min per wash.
IX. PBS was removed from the channel.
X. ~30 µL of Matrigel was pipetted into the compartments and incubated for 10 min at 37 °C.
XI. Fibronectin was perfused through the channel and incubated for 1 h at 37 °C (alternatively, 2 h at room temperature).
XII. HUVEC-C cells were detached from a confluent T25 flask.
XIII. Cells were centrifuged and resuspended in 250 µL of medium (divided across two Eppendorf tubes).
XIV. The cell suspension was loaded into a syringe using a needle.
XV. The needle was replaced with the tubing adapter, and the suspension was perfused into the channel; cells were allowed to adhere for 30 min at 37 °C.
XVI. Additional cell suspension (second Eppendorf) was perfused, and the chip was inverted to allow adhesion to the opposite channel surface, followed by a further 30 min incubation at 37 °C.
XVII. The waste tubing was plugged, and the chip was connected to the perfusion system.

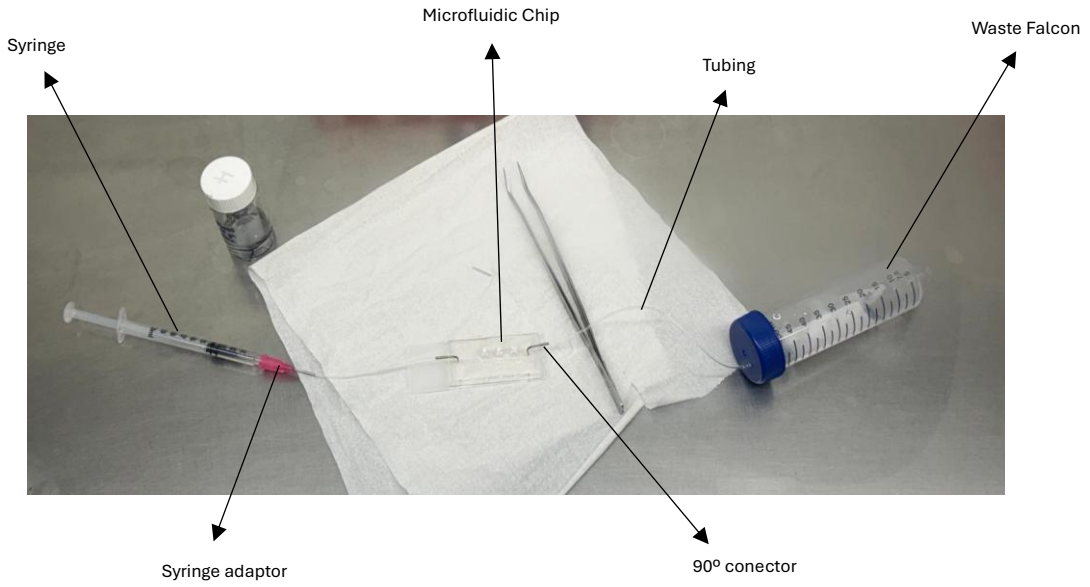


Figure 12. **Experimental setup used for HUVEC-C perfusion and chip endothelialization.** Materials include a microfluidic chip, silicone tubing, connectors, a syringe fitted with an adaptor, and forceps for chip handling.

IV. Results

1. Engineering

1.1. Device Design

The design of the MetaCHIP platform underwent an iterative optimization process comprising three main designs (v3–v5), each developed to address fabrication and handling limitations identified in the preceding version (Figure 13).

The initial prototype, MetaCHIP v3, featured tissue chambers generated using 3 mm biopsy punches and positioned relatively close to one another. To increase chamber height, this design incorporated two layers of xurographed PDMS (Figure 13). During fabrication, however, the short distance between adjacent chambers made the punching procedure particularly challenging. The mechanical stress generated during punching could deform or tear the surrounding PDMS, frequently resulting in irregular chamber edges and compromising fabrication reproducibility.

MetaCHIP v4 addressed these limitations by increasing the overall chip dimensions, thereby enlarging the spacing between chambers, and by increasing chamber diameter from 3 to 4 mm. These changes improved punching reliability, reduced PDMS damage, and provided a larger working area for experimental manipulation. However, a further practical limitation emerged: when low-displacement caps were used to seal the chambers, the remaining spacing was insufficient to accommodate adjacent caps without physical interference.

MetaCHIP v5 was therefore developed by further increasing the distance between tissue chambers while maintaining the 4 mm diameter. This additional spacing enabled independent sealing with low-displacement caps and improved access to individual chambers. The larger chamber size also facilitated hydrogel loading and more consistent Matrigel confinement at the bottom glass surface. Overall, v5 represented the final geometric optimization of the platform, combining improved fabrication reproducibility, chamber accessibility, sealing compatibility, and hydrogel handling.

Each version was developed with either three or four tissue chambers, with the four-chamber configuration including an additional compartment for the primary tumor model. Initial validation was mainly performed using the three-chamber format because of its simpler handling. Functionally, the three-chamber design allows investigation of circulating tumor cells and their interactions with secondary tissue compartments,

whereas the four-chamber configuration additionally enables analysis of interactions between the primary tumor, the vascular compartment, and downstream metastatic sites.

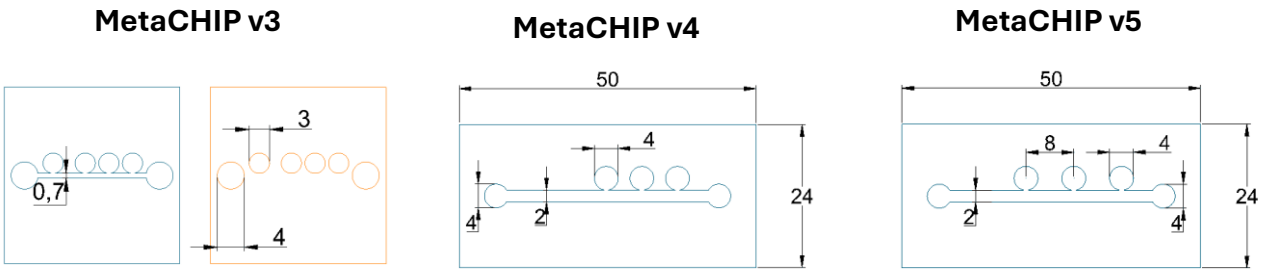


Figure 13. Evolution of the MetaCHIP device design across three successive design versions (v3–v5). Created using computer-aided design (CAD) software. Dimensions are indicated in millimeters.

1.2. Flow, Shear Stress and Culture-Medium Permeation Simulation

As a preliminary *in silico* evaluation of the device, CFD simulations were performed to model flow velocity, shear stress, and culture-medium permeation within the MetaCHIP chip. This approach allowed the fluid dynamics and diffusion behavior expected within each compartment to be assessed computationally before and in parallel with experimental testing, providing a basis for comparison with the flow and permeation patterns observed experimentally.

The simulated flow pattern showed a steady, uniform speed along the straight section of the channel, with fluid speeding up locally where it entered from the narrower connector into the wider channel (Figure 14).

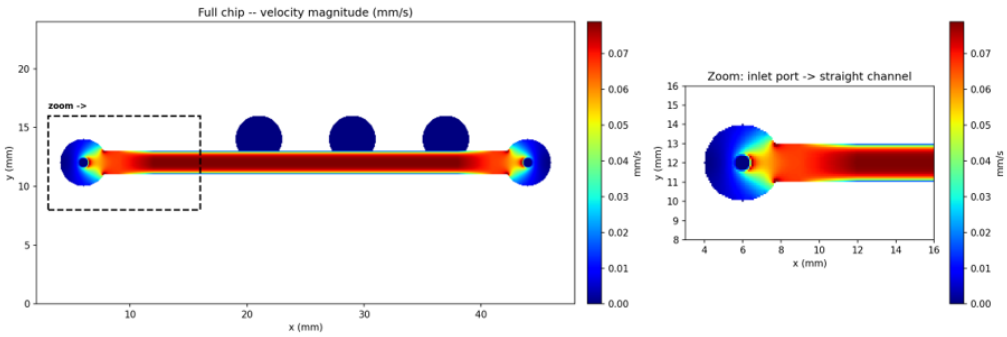


Figure 14. Full-chip velocity field (left) and detail of the inlet port-to-channel transition (right).

The depth-averaged profile was obtained by numerically integrating over the channel depth at each lateral position and then rescaled to the target flow rate of 4 µL/min. The resulting profile shows a peak centerline speed of approximately 0.079 mm/s, decreasing smoothly to zero at both side walls, confirming that the finite channel width introduces an additional, physically expected velocity gradient (Figure 15). The observed simulation pattern is compatible with a laminar flow profile as expected.

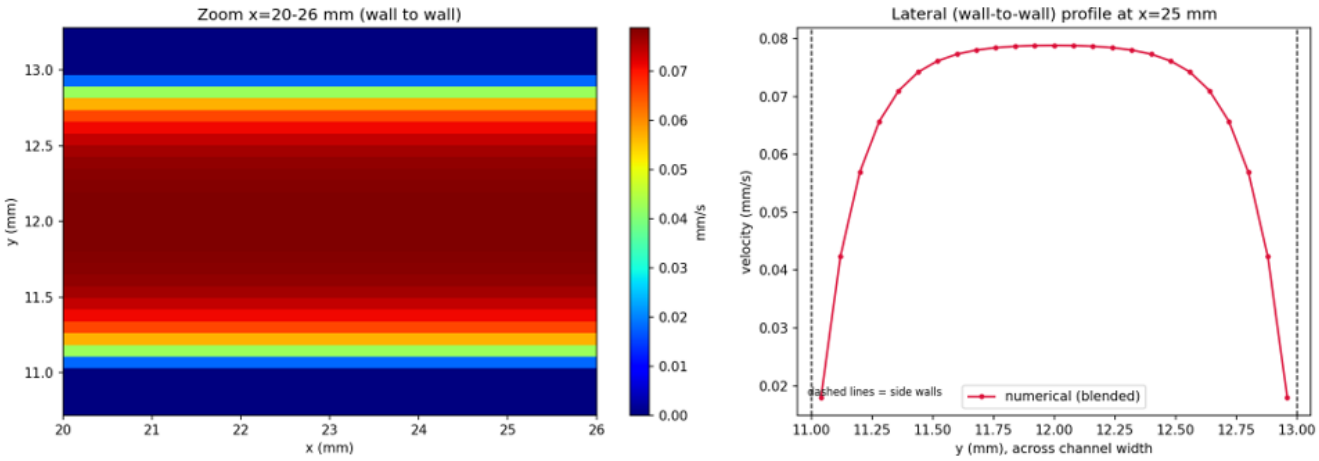


Figure 15. **Lateral (wall-to-wall) velocity profile across the channel width at x = 25 mm, illustrating the near-wall slowdown.**

The mechanical forces experienced by cells within the main channel are also a critical design parameter, since excessive wall shear stress can compromise cell viability and function, while physiologically relevant shear levels can support cell maturation. To evaluate this, wall shear stress along the main channel was computed.

Shear stress was computed according to the formula $\tau = 6\mu Q/(h^2 w)$, where Viscosity, µ is the viscosity of the liquid flowing, Q the flow rate inputed, h the channel height and w the channel width. The manually calculated shear stress value, obtained from the analytical straight-duct formula, matched the numerically simulated plateau value at the core of the straight channel (x = 9–40 mm) to within numerical precision, confirming the internal consistency of the flow simulation (0.6160 mPa)..A minimum and maximum shear stress value of 0.3479 mPa and 0.8375 mPa across the channel geometry were computed (Table 6). Locally elevated shear stress occurs only near the channel/port junctions, where the flow converges toward the needle, and is not captured by the simple straight-duct formula. Matrigel chambers were excluded from the map, as they are not exposed to appreciable convective shear (Figure 17).

The input parameters used in the simulation are listed in Table 3, in the Materials and Methods section 1.2.

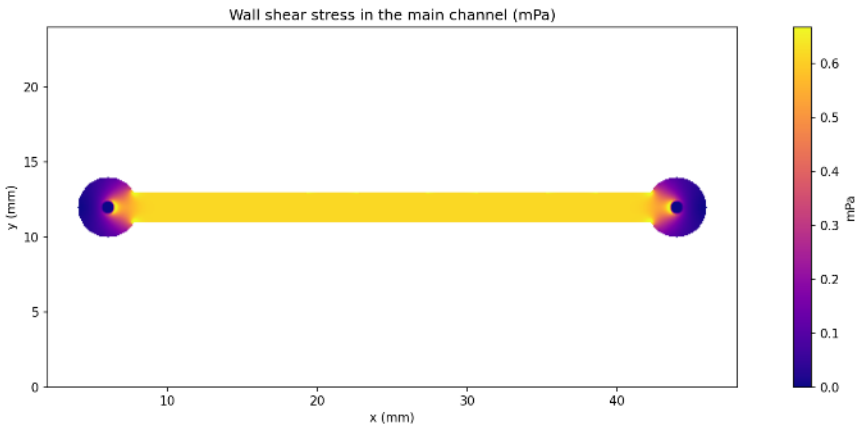


Figure 16. **Wall shear stress along the main channel and ports.** The value is quasi-constant along the straight channel (x = 9–40 mm), rising near the channel/port junctions, where the flow converges with the connector

Table 7. **Numerical wall shear stress values.** In the main channel, including the plateau region and the minimum/maximum values observed near the channel/port junctions.

Parameter	Value
τ numerical, plateau (x = 9–40 mm)	Simulated value - 0.6160 mPa
τ numerical, min (channel, incl. port overlap)	Simulated value - 0.3479 mPa
τ numerical, max (channel, incl. port overlap)	Simulated value - 0.8375 mPa

It is also important to ensure that cell culture medium from the main channel (representing the artificial vasculature) effectively reaches the hydrogel-filled chambers, which represent the metastatic target sites. To test this, computational simulations were used to predict how culture medium will penetrate from the main channel into each chamber, and the time required for this process to occur.

Chamber 1 (closest to the inlet) reached saturation fastest, consistent with its shorter convective transport distance from the source. At 120 min, the three chambers reached 66.5%, 64.7%, and 63.2% of the source concentration, respectively (Figure 17A). Spatial concentration maps further showed that the channel reached near-uniform source concentration within minutes, owing to fast advective transport, whereas the three

matrigel chambers filled by diffusion alone, producing a visibly slower, radially graded concentration front that had not reached full saturation by the end of the simulated period (Figure 17B).

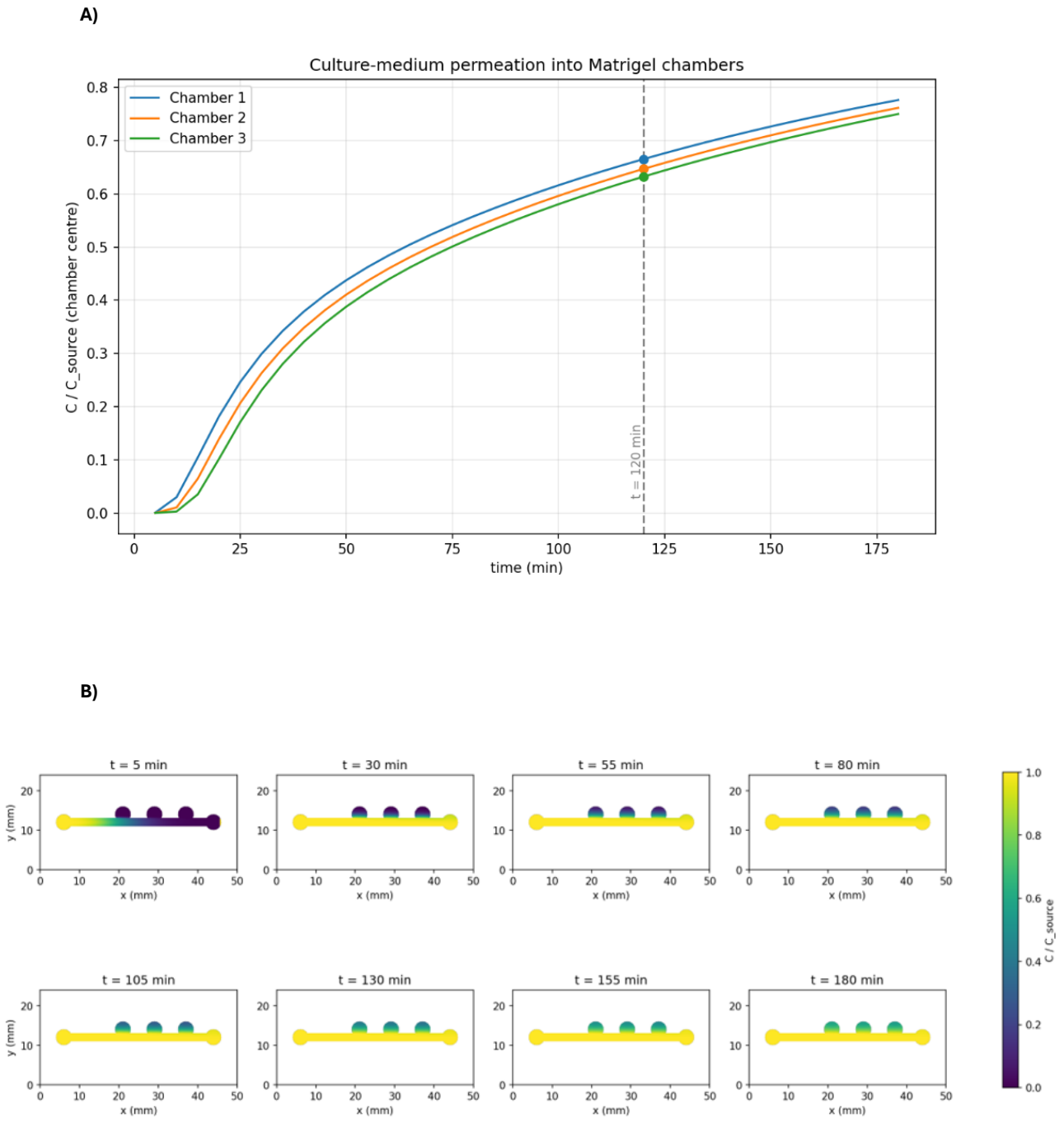


Figure 17. **Time evolution of the culture-medium concentration** (normalized to the source concentration) at the center of each of the three Matrigel chambers (A), and spatial distribution of the normalized concentration at eight time points (5 to 180 min) after the start of perfusion (B).

1.3. Fabrication

With the fabrication protocol established, device assembly was assessed in terms of structural integrity and batch-to-batch reproducibility

Following the xurography-based fabrication protocol described in Chapter III (Section 1.2), MetaCHIP devices were successfully assembled into fully bonded, ready-to-use microfluidic platforms (Figure 18). The fabrication process consistently yielded devices with well-defined tissue chambers and a continuous central perfusion channel, confirming the reproducibility of the protocol across multiple fabrication batches.

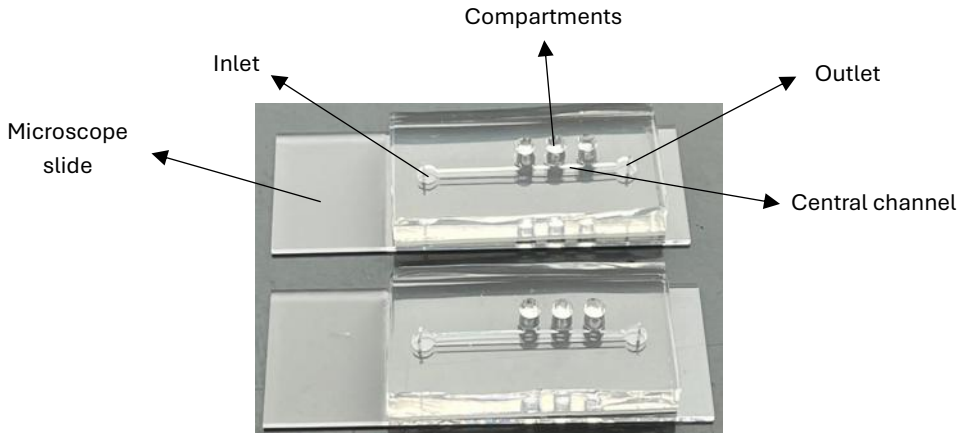


Figure 18. **Representative photograph of fabricated MetaCHIP devices** (MetaCHIP v5, with 3 chambers).

2. Validation of the Technological Model

2.1. Hydrogel Confinement

To evaluate the effect of chamber diameter on hydrogel confinement, MetaCHIP v4 devices, featuring both 3 mm and 4 mm tissue chambers on the same chip, were loaded with 4 µL of Matrigel per chamber and visually inspected (Figure 19). While adequate confinement could occasionally be achieved in the 3 mm chambers, handling was considerably more difficult compared to the 4 mm chambers, with the hydrogel frequently

receding toward the chamber walls rather than settling uniformly at the bottom. In contrast, the 4 mm chambers consistently allowed for more reliable and reproducible hydrogel confinement. These results supported the selection of the 4 mm chamber diameter for the final MetaCHIP v5 design.

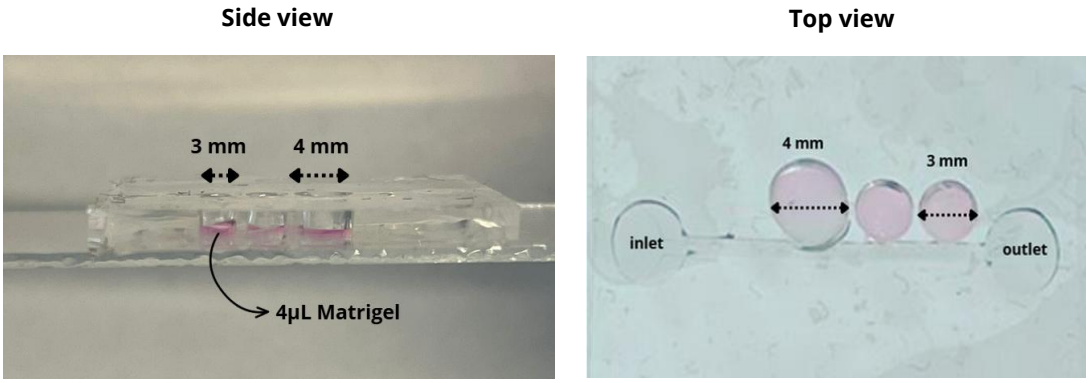


Figure 19. **Comparison of Matrigel confinement between 3 mm and 4 mm tissue chambers on a MetaCHIP v4 device.** Side view (left) and top view (right) images show 4 µL of Matrigel (pink) loaded into 3 mm and 4 mm chambers. Inlet and outlet ports are indicated in the top view.

2.2. Chamber volume

As described previously, the MetaCHIP device is composed of two PDMS layers: a channel layer, obtained by cutting a thin PDMS sheet to define the microfluidic network, and a separate layer produced manually by casting PDMS into Petri dishes, which is subsequently bonded to the channel layer. Since the tissue chambers are formed by punching directly through this cast layer, its thickness directly dictates the maximum culture-medium capacity of each chamber.

To maximize this culture's medium capacity without compromising the mechanical integrity of the PDMS during punching, four PDMS casting volumes were tested (22.5, 25, 27.5, and 30 mL). This volume was poured into standard Petri dishes, corresponding to increasing PDMS layer thicknesses and, consequently, increasing chamber volumes (35, 40, 48, and 55 µL, respectively, for a 4 mm punch) (Figure 20). All four casting volumes allowed successful punching without PDMS tearing. A casting volume of 30 mL was selected for subsequent device fabrication, as it provided the largest chamber volume while avoiding excessive PDMS thickness.

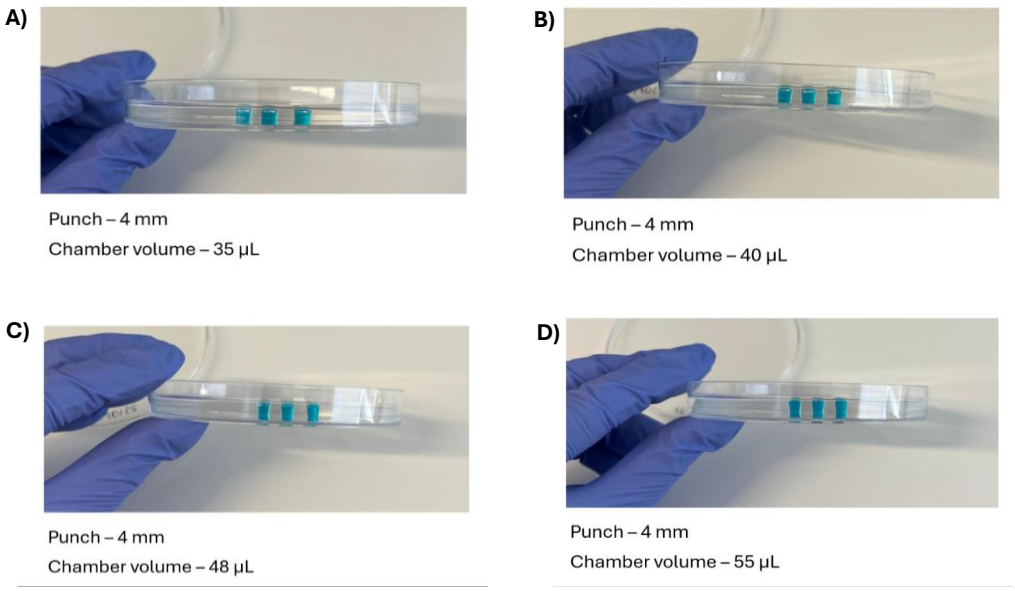


Figure 20. **Comparison of PDMS casting volumes and resulting tissue chamber volumes.** Side view of PDMS layers cast at increasing volumes and punched using a 4 mm biopsy punch, resulting in progressively larger tissue chamber volumes: (A) 22.5 mL casting volume, 35 µL chamber volume; (B) 25 mL casting volume, 40 µL chamber volume; (C) 27.5 mL casting volume, 48 µL chamber volume; (D) 30 mL casting volume, 55 µL chamber volume.

2.3. Leakage Test

To assess the fluidic integrity of the fabricated platforms, leakage tests were performed on the MetaCHIP v4 device, following a similar assessment previously conducted on the MetaCHIP v3 device over a 24 h perfusion period, during which no leakage was observed.

For the MetaCHIP v4 device, the two end chambers were sealed with low-volume displacement caps, while the middle chamber was sealed with an adhesive PCR sealing film. A colored aqueous solution was continuously perfused through the central channel at 3 mbar over a 16 h period, and the device was visually inspected for fluid leakage across the PDMS interfaces or into the external environment (Figure 21). No leakage was detected at either T0h or T16h, confirming the fluidic integrity of the device.

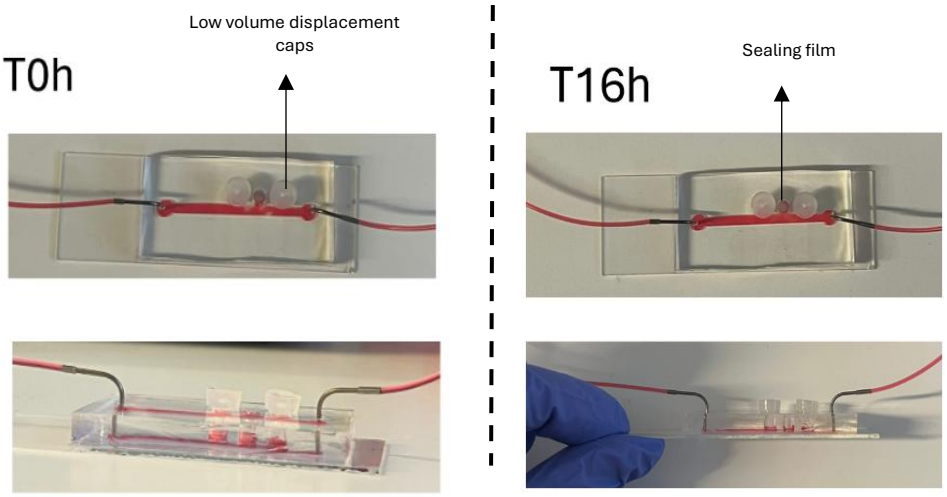


Figure 21. **Leakage test of a MetaCHIP v4 device at T0h and T16h.** Top and side views show the device during continuous perfusion of a colored aqueous solution at 3 mbar. No visible leakage was observed at either timepoint.

2.4. Diffusion Test

To assess whether our fluidic design and flow rates could efficiently permeate the hydrogel, which is essential for secondary niche priming with conditioned media, as mentioned earlier, we performed a diffusion test to complement and experimentally validate the permeation behavior previously predicted by CFD simulation.

To evaluate passive diffusion between the central perfusion channel and the tissue chambers, a MetaCHIP v5 device loaded with Matrigel was continuously perfused with a colored aqueous solution (blue). An initial observational assessment indicated a progressive color change within the tissue chambers over time, from pink/purple to blue, consistent with diffusion of the solution into the hydrogel-filled compartments (Figure 22). To quantitatively characterize this process, images were acquired at defined time points (30, 60, 75, 90, and 120 min) following an initial PBS wash (Figure 23A), and the percentage of hydrogel area reached by the colored solution in each chamber was determined using Fiji (ImageJ). Diffusion progressed steadily over time, reaching a mean of 26% at 30 min, 35% at 60 min, 58% at 75 min, and 82% at 90 min, with complete diffusion (100%) achieved across all chambers by 120 min (Figure 23B).

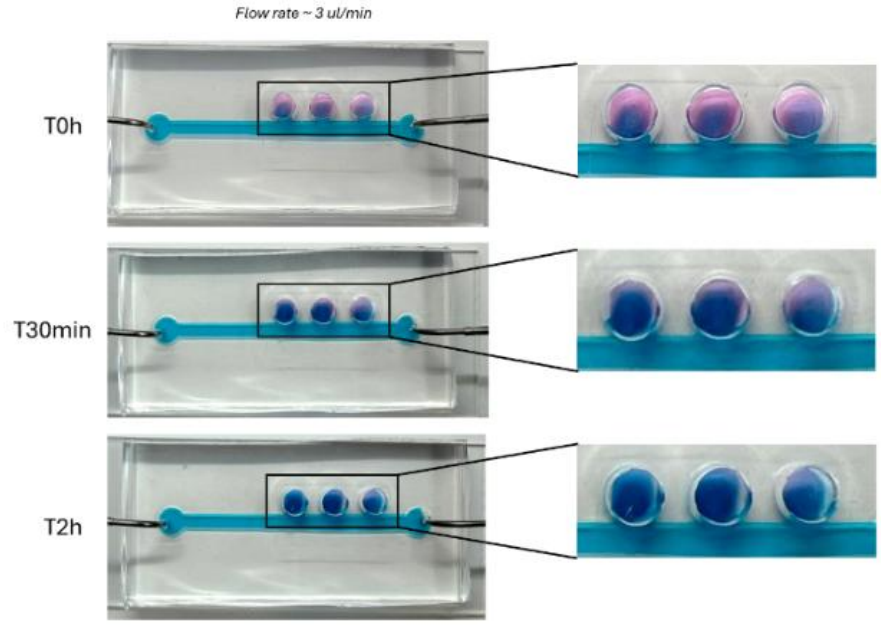


Figure 22. **Preliminary diffusion test in a MetaCHIP v5 device**. A colored aqueous solution was perfused through the central channel at a flow rate of ~3 µL/min. Progressive color change within the tissue chambers, from pink/purple (T0h) to blue (T2h), indicates diffusion of the solution into the hydrogel-filled compartments.

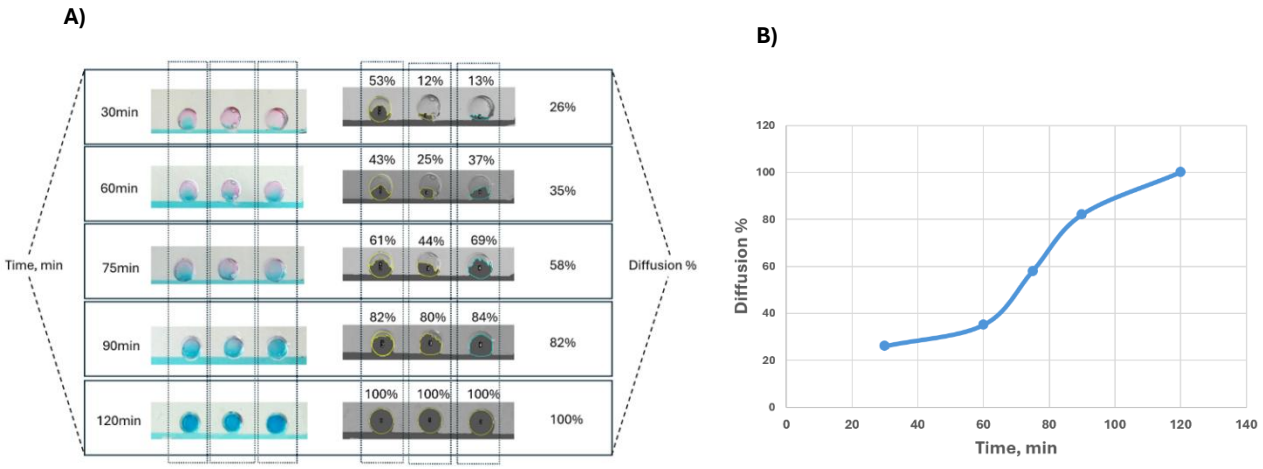


Figure 23. **Quantitative diffusion assay in a MetaCHIP v5 device.** (A) Representative top-view images of the tissue chambers at increasing time points (30–120 min) following perfusion of a colored aqueous solution through the central channel, with the corresponding percentage of hydrogel area reached by the solution indicated for each chamber and the mean diffusion percentage per time point shown on the right. (B) Mean diffusion percentage across the three tissue chambers as a function of time.

3. Validation of the Biological Model

The MetaCHIP was built to support coculture of four/five biological models: the primary tumor, which will be represented by gastric cancer spheroids; the artificial vasculature, represented by endothelial cells cultured on top of a physiologically relevant coating; and the secondary metastatic sites, represented by organ-specific cell types corresponding to common sites of gastric cancer metastasis. As an initial validation strategy, each of these components was first developed and characterized one by one, before their integration into the complete multi-organ platform. This approach allowed the establishment and optimization of culture conditions, seeding densities, and assay protocols specific to each physiological model.

Validation began with the establishment of gastric cancer spheroids, representing the primary tumor compartment (Section 3.1), followed by the development and characterization of the artificial vasculature (Section 3.2). Metastatic target sites were then addressed, focusing on the lung and liver as common sites of gastric cancer metastasis, represented by BEAS-2B and HepaRG cell lines, respectively (Sections 3.3 and 3.4).

3.1. Gastric Cancer Spheroids

To represent the primary tumor compartment within the MetaCHIP platform, 3D spheroids were generated from two gastric cancer cell lines, MKN-74 and MKN-45, representing the intestinal and diffuse histological subtypes, respectively, as classified by the Laurén system.

Before their integration into the microfluidic device, spheroids were characterized in static culture to establish an appropriate seeding density and to evaluate their growth kinetics, viability, and metabolic activity over time, ensuring the use of a reproducible and viable tumor model for subsequent on-chip experiments.

3.1.1. Cell Seeding

Spheroids were generated using the MicroTissues® 3D Petri Dish® micromold system. First, we seeded the MKN-74 cells to test two different densities, corresponding to nominal spheroid diameters of 100 µm and 200 µm. And then we seeded, MKN-45 cells were seeded at the predefined density (200 µm), following the protocol described in Chapter III (Section 2.2.2). Brightfield microscopy performed immediately after seeding (T0) confirmed successful cell distribution within the agarose microwells for both densities, before spheroid compaction (Figure 24).

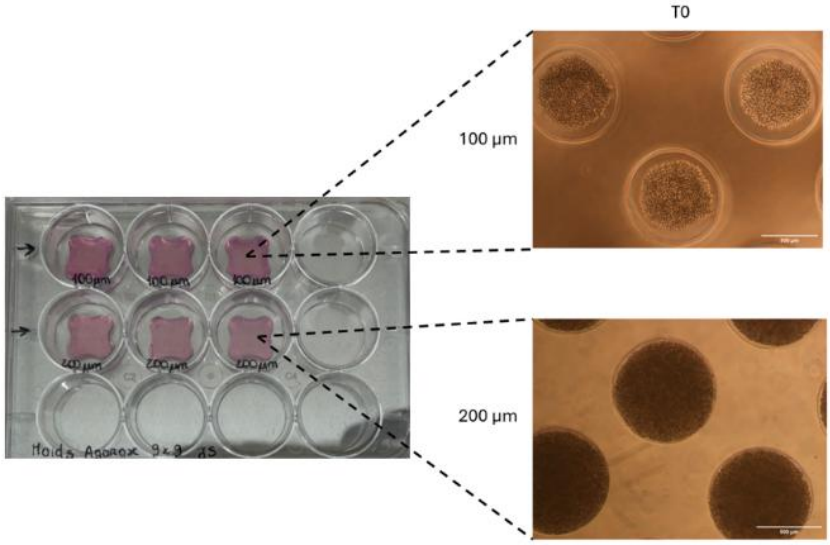


Figure 24. **Cell distribution within agarose microwells immediately after seeding (T0).** Representative brightfield images of MKN-74 cells seeded at densities corresponding to nominal spheroid diameters of 100 µm (top) and 200 µm (bottom), prior to spheroid compaction.

3.1.2. MKN-74 Spheroids – Growth Kinetics and Viability

Following embedding in Matrigel, MKN-74 spheroids generated at two seeding densities, corresponding to nominal diameters of 100 µm and 200 µm, were monitored over 72 h to assess their growth behavior (Figure 25). It should be noted that these nominal values reflect the expected spheroid size at the time of seeding and do not represent the actual spheroid size at later time points, as spheroids continued to grow within the Matrigel matrix over the course of the assay.

Spheroid area was measured at each time point using Fiji (ImageJ) (Figure 26). The 200 µm spheroids exhibited a larger initial area (T0: ~280,000 µm²) but remained largely

stable over the 72-h period (T72: ~290,000 µm²), whereas the 100 µm spheroids, despite starting from a smaller initial area (T0: ~115,000 µm²), displayed a more pronounced increase in area over time, nearly doubling by T72 (~215,000 µm²).

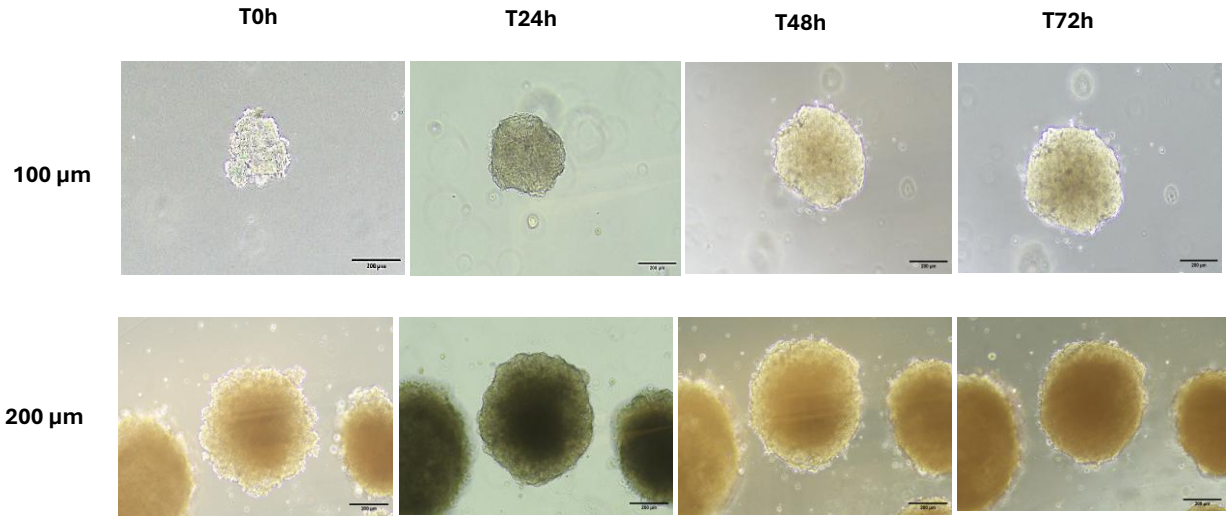


Figure 25. **Brightfield images of MKN-74 spheroids embedded in Matrigel over 72 h.** Representative images of spheroids generated at 100 µm and 200 µm at T0, T24, T48, and T72.

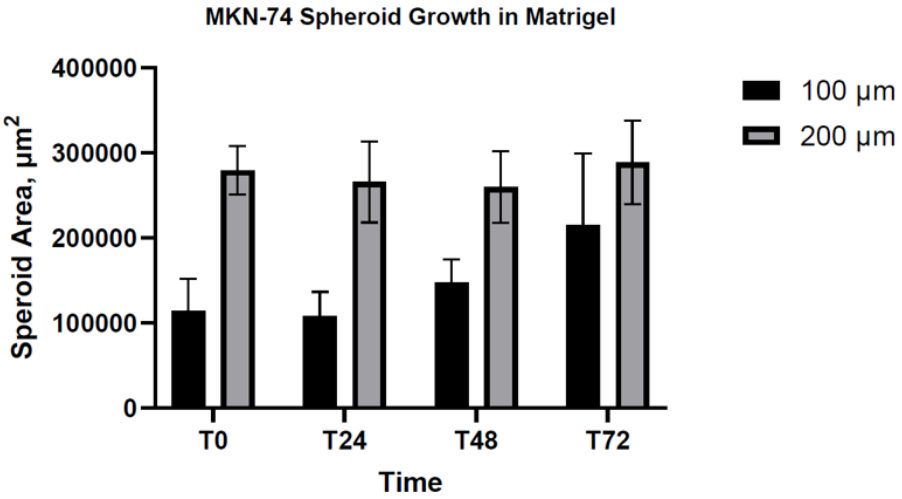


Figure 26. **Growth kinetics of MKN-74 spheroids in Matrigel.** Spheroid area (µm²) for 100 µm and 200 µm spheroids at T0h, T24h, T48h, and T72h, measured using Fiji (ImageJ) (mean ± SD).

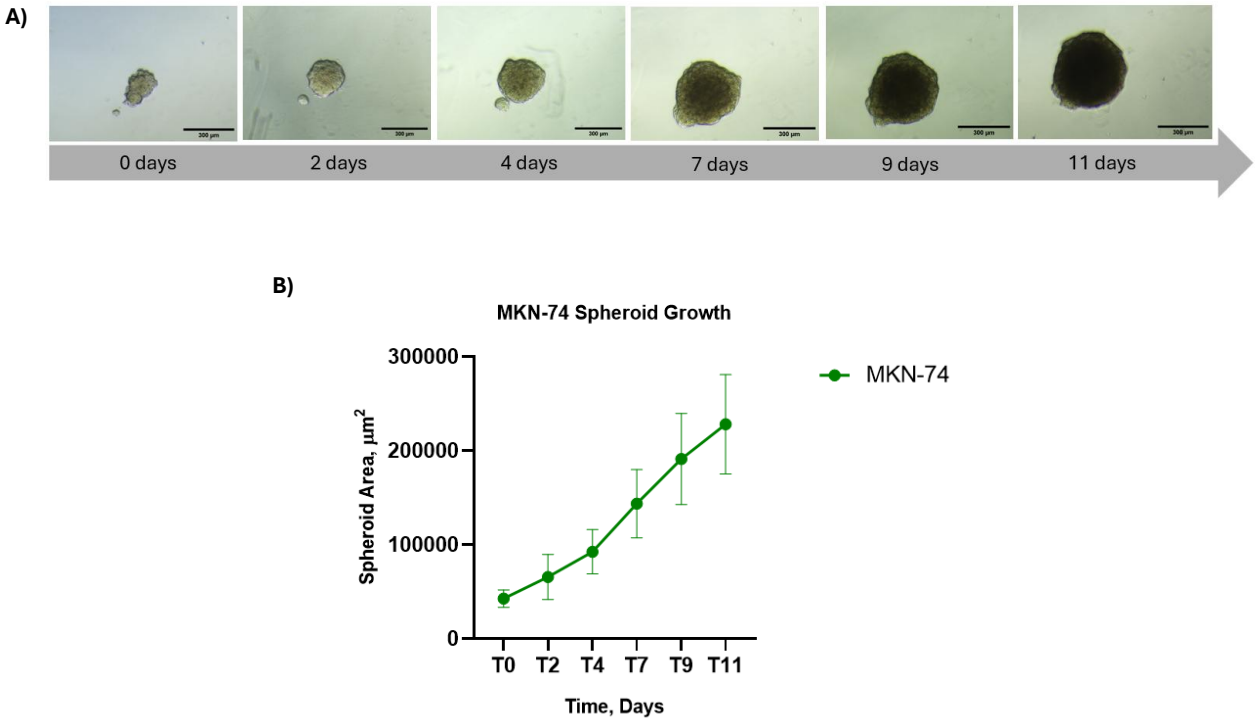


Figure 27. Growth of MKN-74 spheroids embedded in Matrigel during 72 h. (A) Representative brightfield images of spheroids generated at a 100 µm nominal diameter at T24, T48, and T72. (B) Spheroid area (µm²) over time, measured using Fiji (ImageJ) (mean ± SD).

To assess spheroid viability following prolonged culture in Matrigel, MKN-74 spheroids generated at both seeding densities (corresponding to nominal diameters of 100 µm and 200 µm) were evaluated using a Live/Dead assay after 10 days in culture (4 days in the agarose micromold followed by 6 days embedded in Matrigel) (Figure 28). Spheroids generated at the lower seeding density displayed predominantly high viability, with strong Calcein-AM (green) signal throughout the spheroid structure and minimal ethidium homodimer-1 (red) staining. In contrast, spheroids generated at the higher seeding density exhibited a more pronounced red signal, indicating increased cell death within these larger spheroids.

Taken together, these results indicate that the 100 µm nominal diameter yielded spheroids with greater growth potential and improved viability over extended culture periods. In contrast, the 200 µm spheroids exhibited stable growth across time points, a phenotype potentially consistent with the onset of cellular senescence, although this was not directly assessed in the present study. These spheroids also displayed increased cell death by day 10, compared with the 100 µm spheroids. Based on these findings, the 100

µm seeding density was selected for subsequent MKN-74 spheroid experiments, as well as for the generation of MKN-45 spheroids.

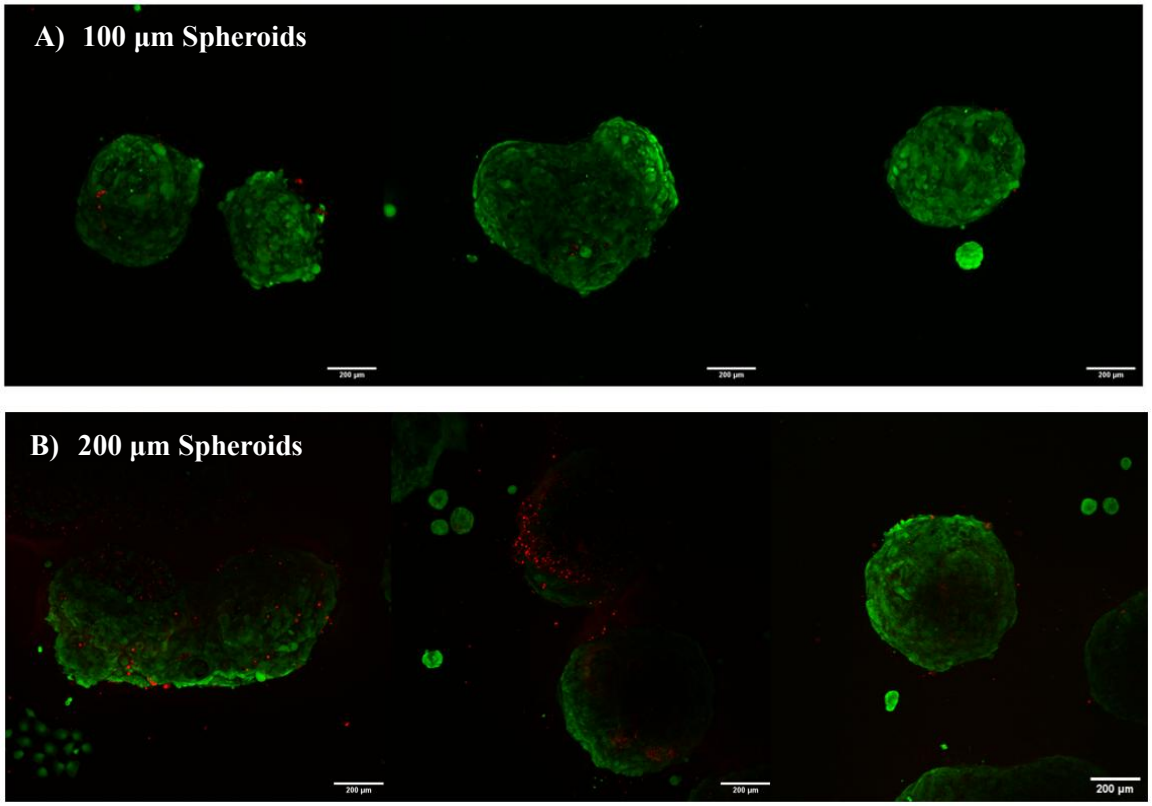


Figure 28. **Viability of MKN-74 spheroids after 10 days in culture (6 days embedded in Matrigel).** Live/Dead staining (Calcein-AM, green: live cells; ethidium homodimer-1, red: dead cells) of spheroids generated at (A) 100µm: 32,000 cells per mold and (B) 200µm: 256,000 cells per mold

3.1.3. MKN-45 Spheroids – Growth Kinetics and Viability

Based on the results obtained for MKN-74 spheroids, the 100 µm nominal diameter was selected to generate MKN-45 spheroids. Following embedding in Matrigel, spheroid growth was monitored over 72 h by brightfield microscopy (Figure 29A) and quantified using Fiji (ImageJ) (Figure 29B). MKN-45 spheroids displayed a consistent increase in area over time, from approximately 185,000 µm² at T0 to 350,000 µm² at T72, without evidence of growth stagnation, a pattern consistent with that observed for MKN-74 spheroids at the same seeding density.

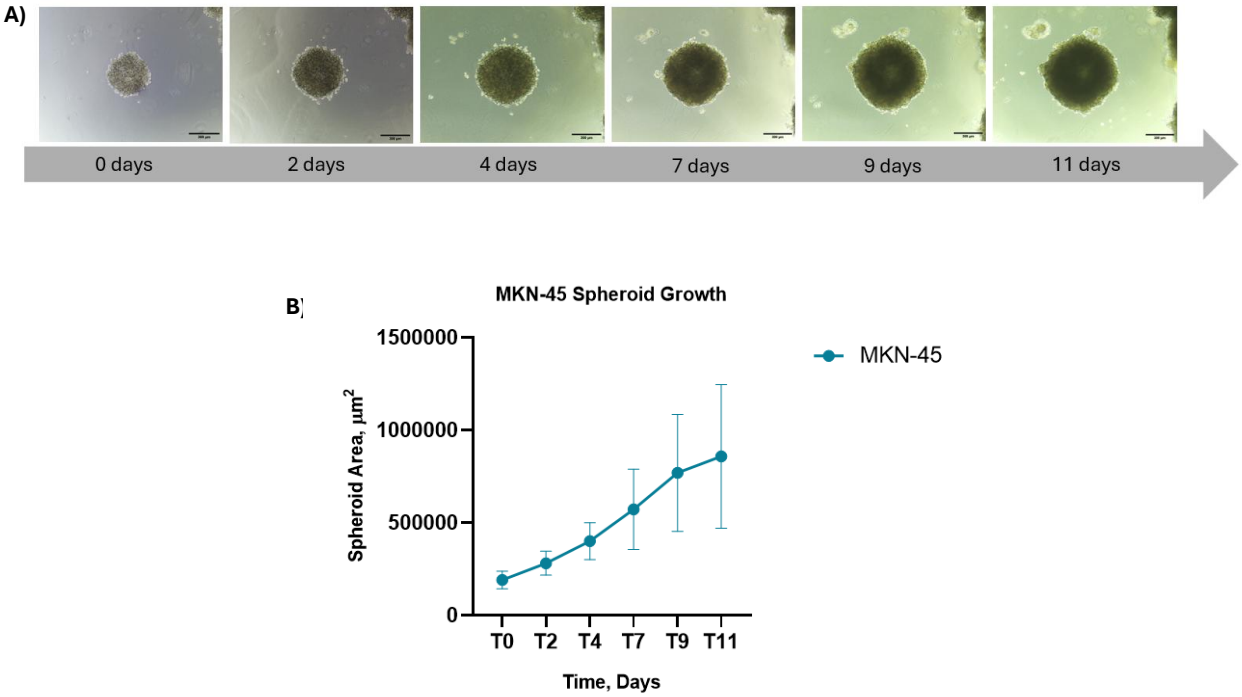


Figure 29. **Growth of MKN-45 spheroids embedded in Matrigel during 72 h.** (A) Representative brightfield images of spheroids generated at a 100 µm seeding density at T24, T48, and T72. (B) Spheroid area (µm²) over time, measured using Fiji (ImageJ) (mean ± SD).

Spheroid viability was subsequently assessed by Live/Dead staining after 10 days in culture (6 days embedded in Matrigel) (Figure 30). MKN-45 spheroids exhibited predominantly high viability, with strong Calcein-AM (green) signal and minimal ethidium homodimer-1 (red) staining, consistent with the results obtained for MKN-74 spheroids at the same density. Numerous small, dispersed Calcein-AM-positive cells were also observed surrounding the spheroids, which may reflect the loose cell-cell adhesion characteristic of MKN-45 cells, consistent with the reduced E-cadherin function typically associated with the diffuse-type gastric cancer phenotype.

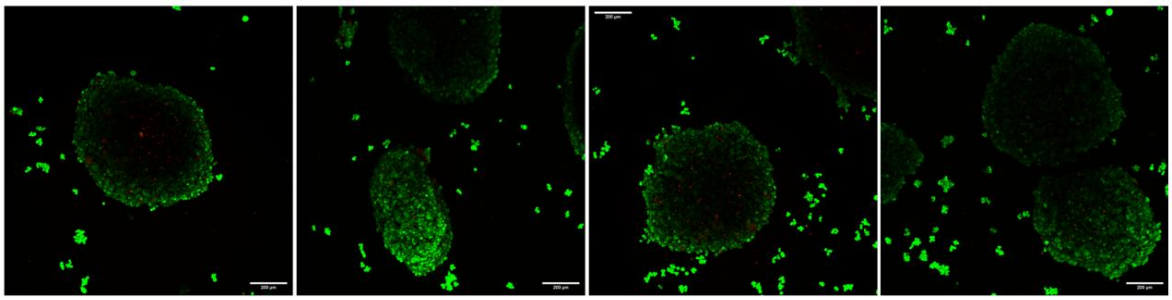


Figure 30. **Viability of MKN-45 spheroids after 10 days in culture (6 days embedded in Matrigel).** Live/Dead staining (Calcein-AM, green: live cells; ethidium homodimer-1, red: dead cells).

3.1.4. Metabolic Activity

To determine an appropriate resazurin incubation time for gastric cancer spheroids embedded in Matrigel, MKN-74 and MKN-45 spheroids (100 µm seeding density) were incubated with the resazurin working solution, and fluorescence was measured at multiple time points over a 9 h period (Figure 31). While 2D cell cultures are typically incubated with resazurin for 2 h, this incubation was not enough for spheroids embedded in Matrigel, because fluorescence signal remained low. During the 9h incubation the signal continuously increased, without reaching a plateau. Based on these results, a 6 h incubation period was selected as good compromise between sufficient signal accumulation and practical incubation time.

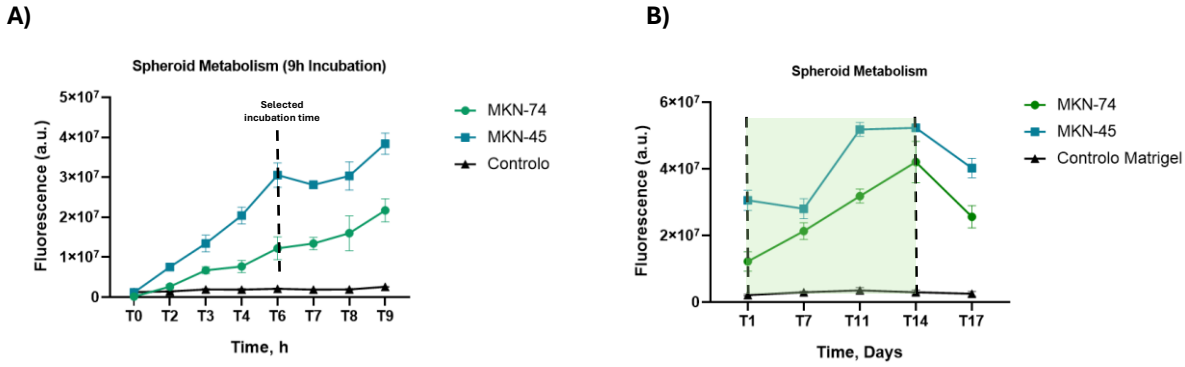


Figure 31. **Metabolic activity of MKN-74 and MKN-45 spheroids embedded in Matrigel.** (A) Resazurin incubation time optimization, showing fluorescence signal over a 9 h incubation period. (B) Long-term monitoring of spheroid metabolic activity over 17 days, using a 6 h resazurin incubation. Matrigel-only wells were included as a negative control in both assays.

3.2. Artificial Vasculature

To represent the vascular compartment within the MetaCHIP platform, human umbilical vein endothelial cells (HUVEC-C) were cultured within the central perfusion channel, forming an artificial vasculature intended to serve as a physiological barrier for studying intravasation and extravasation processes during metastasis. Since endothelial cell attachment and monolayer formation are highly dependent on the underlying substrate, an appropriate extracellular matrix coating was first established and validated in static culture before seeding cells within the microfluidic device, to ensure the formation of a stable, confluent, and physiologically representative vascular barrier on-chip.

3.2.1. Coating Optimization

To assess the reliability of different coating conditions over time, HUVEC-C cells were cultured on cell culture plates coated with fibronectin, gelatin, or left uncoated, and imaged by brightfield microscopy up to 72 h in culture (Figure 32). At 72 h, cells cultured on both fibronectin- and gelatin-coated plates continued to proliferate, displaying a well-spread, elongated spindle-shaped morphology and increasing confluency over time. In contrast, cells on uncoated coverslips showed signs of detachment, with an apparent reduction in cell number by 72 h compared with the coated conditions, indicating that the absence of an extracellular matrix coating compromised long-term cell adhesion and viability.

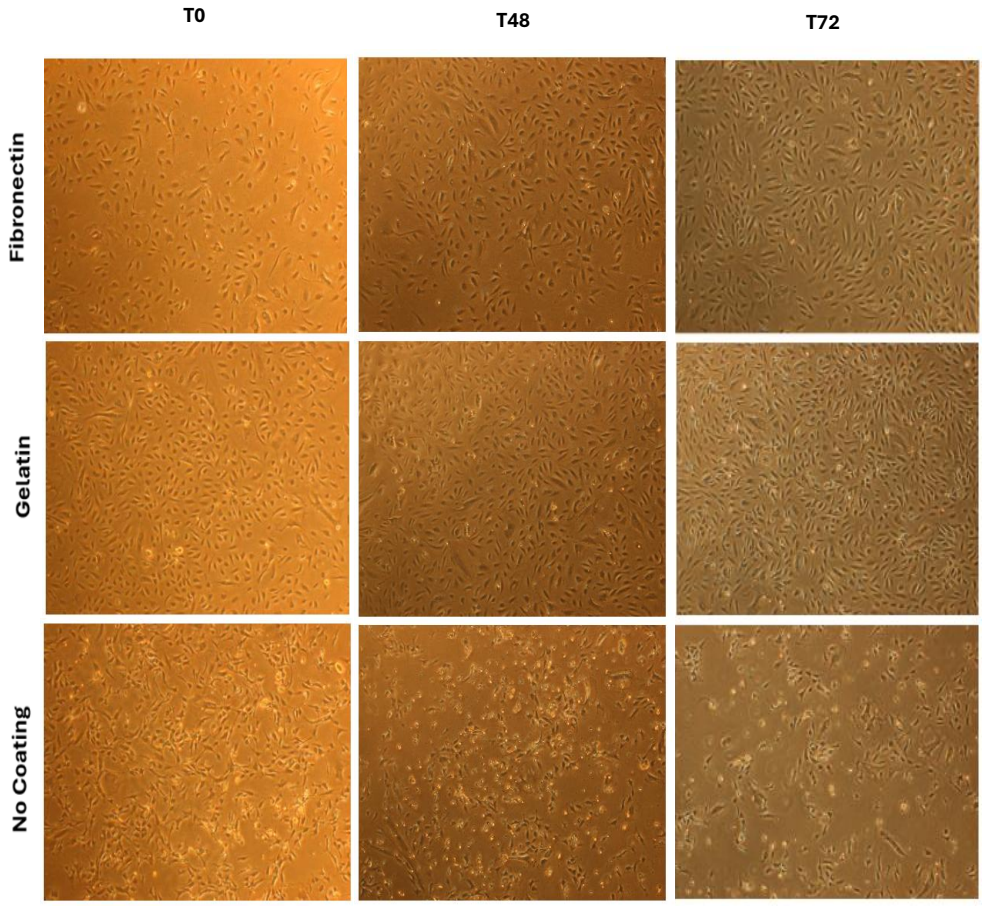


Figure 32. **Brightfield microscopy images of HUVEC-C.** Images were acquired at 0, 48, and 72 hours (T0, T48, T72) after seeding. At 72 h, cells on fibronectin- and gelatin-coated coverslips displayed continued proliferation and increasing confluency, whereas cells on uncoated coverslips showed reduced cell number and signs of detachment.

Cells were further assessed by immunofluorescence staining for CD31 (Figure 33). All three coating conditions supported CD31-positive staining, consistent with maintenance of the endothelial phenotype, with fibronectin- and gelatin-coated cells displaying higher cell density (DAPI) compared to the uncoated condition. Given the comparable performance of fibronectin and gelatin, fibronectin was selected as the coating condition for subsequent experiments, owing to its human origin and its widespread use as a substrate for endothelial cell culture [124].

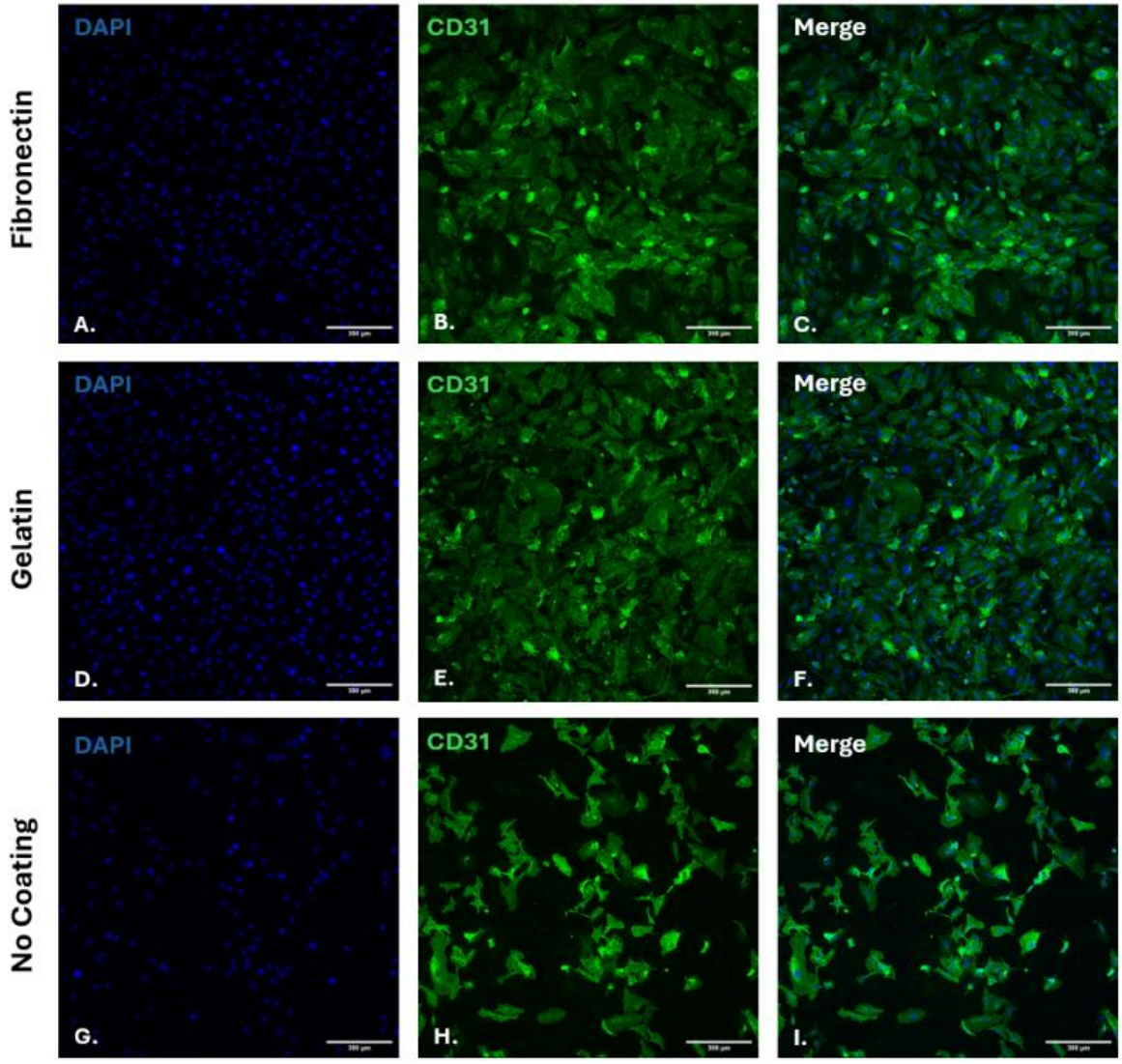


Figure 33. **Immunofluorescence characterization of HUVEC-C cultured on fibronectin, gelatin, or uncoated coverslips.** DAPI (nuclei, blue), CD31 (endothelial marker, green), and merged images for fibronectin (A–C), gelatin (D–F), and no coating (G–I).

3.2.2. HUVECs-on-CHIP

After the optimization of the coating condition, HUVEC-C were seeded into the microfluidic channel of the MetaCHIP device on a fibronectin-coated surface and assessed by brightfield microscopy 24 h after perfusion (Figure 34). Cells successfully attached and formed a confluent monolayer along the channel, with morphology comparable to HUVEC-C maintained in routine 2D culture on gelatin-coated flasks (Figure 34). Cells within the chip appeared more densely packed compared to flask culture, which is likely related, at least in part, to the substantially smaller culture area of the microfluidic channel compared to a T25 flask. The influence of shear stress from continuous perfusion may also have contributed to this appearance, although this was not directly assessed in the present study.

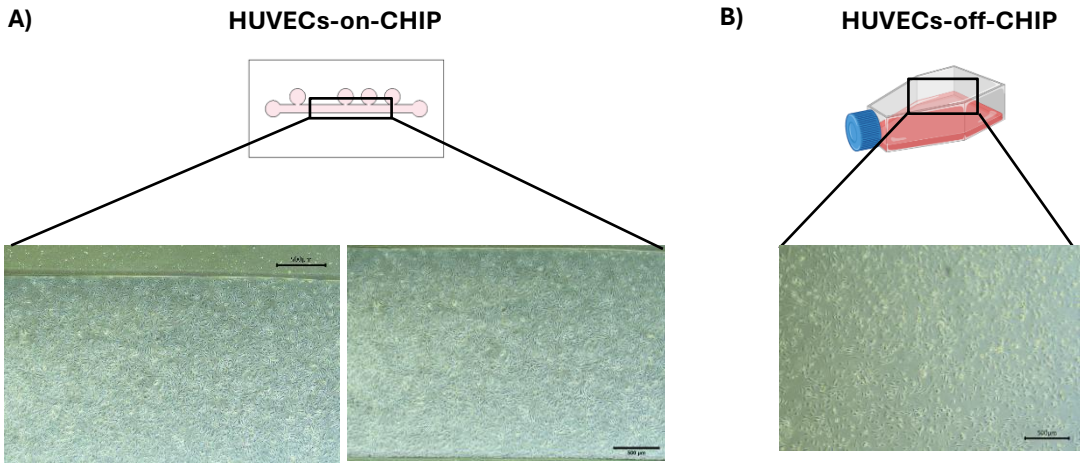


Figure 34. **Comparison of HUVEC-C morphology on-chip and off-chip.** (A) Representative brightfield images of HUVEC-C cultured within the MetaCHIP microfluidic channel 24 h after seeding (HUVECs-on-chip). (B) Representative brightfield image of HUVEC-C cultured under routine 2D conditions on a gelatin-coated T25 flask (HUVECs-off-chip), shown for morphological comparison.

3.3. Medium Compatibility

Since the MetaCHIP platform is designed to co-culture cells from multiple organ systems within a single device, a unified culture medium compatible with all cell types involved is important. However, each of the target-organ cell lines is conventionally maintained in a distinct, organ-specific medium, optimized for its individual metabolic and phenotypic requirements. To evaluate whether this transition to a shared medium could be achieved

without compromising cell function, the metabolic activity of each cell line was compared between its original culture medium and the proposed unified medium (F-12K).

3.3.1. Lung

To assess the compatibility of BEAS-2B cells with the unified F-12K culture medium, specific metabolic activity was evaluated using a sequential resazurin/SRB assay after culture in the conventional medium (DMEM), F-12K, or DMEM/F-12 (Figure 35). Detectable activity was maintained under all conditions. Although DMEM/F-12 showed the highest mean value, followed by F-12K and DMEM, no statistically significant differences were observed between F-12K and either comparison medium. These results indicate that replacement of DMEM with F-12K did not significantly alter the specific metabolic activity of BEAS-2B cells, supporting the compatibility of this medium with the cell type under the conditions tested.

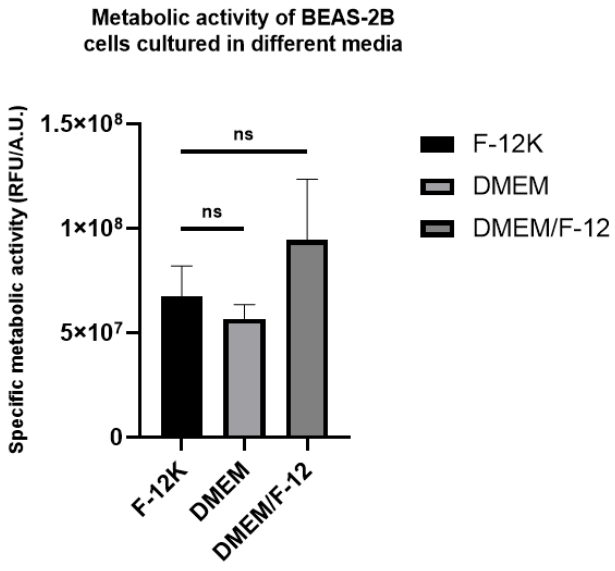


Figure 35. Metabolic activity of BEAS-2B cells cultured in DMEM, F-12K, or DMEM/F-12, assessed using a sequential resazurin/SRB assay. No statistically significant differences were observed between conditions (Kruskal-Wallis test with Dunn's multiple comparisons).

3.3.2. Liver

To assess the compatibility of HepaRG cells with the unified F-12K culture medium, metabolic activity was compared across cells cultured in William's E, F-12K, or DMEM/F-12 using a sequential resazurin/SRB assay (Figure 36). Although mean specific

metabolic activity varied across conditions, no statistically significant differences were observed. HepaRG cells cultured in F-12K showed values comparable to those maintained in their conventional William's E medium, with no apparent reduction following the change in culture medium.

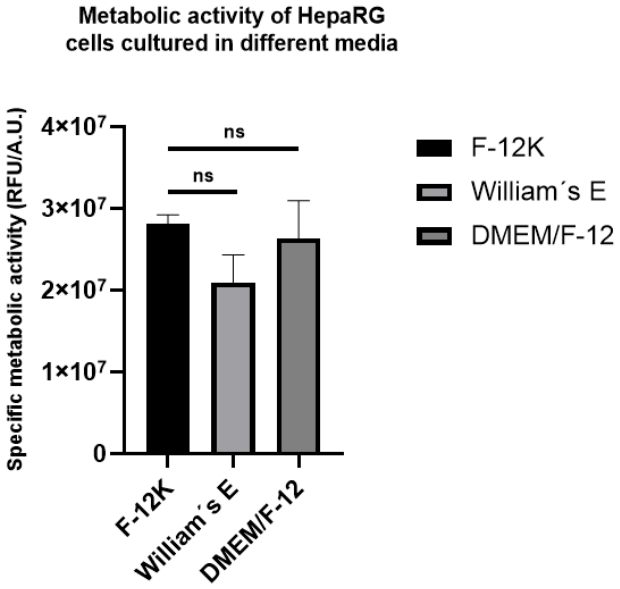


Figure 36. **Metabolic activity of HepaRG cells cultured in William's E, F-12K, or DMEM/F-12**, assessed using a sequential resazurin/SRB assay. No statistically significant differences were observed between conditions (Kruskal-Wallis test with Dunn's multiple comparison

V. DISCUSSION

Gastric cancer metastasis remains difficult to investigate experimentally because it is a dynamic and systemic process involving sequential interactions between the primary tumor, the vascular compartment, and multiple anatomically and biologically distinct target tissues. Conventional *in vitro* assays generally isolate individual metastatic behaviors, such as migration or invasion, whereas animal models provide systemic complexity at the expense of experimental controllability, human specificity, and, frequently, immune competence. Moreover, existing experimental platforms rarely allow the direct and simultaneous comparison of metastatic niches within the same circulating system. This limitation is particularly relevant in gastric cancer, in which the intestinal and diffuse histological subtypes display markedly different patterns of dissemination, suggesting that metastatic progression is determined not only by the intrinsic properties of tumor cells but also by their interaction with organ-specific microenvironments. Accordingly, the development of human-relevant platforms capable of connecting a primary gastric tumor model to several potential metastatic sites represents an important step towards a mechanistic understanding of gastric cancer organotropism.

Beyond these general limitations of current experimental approaches, two specific and largely unresolved questions motivated the design of this work. For diffuse-type GC, it remains unclear whether the rapid, overall lethality driven by peritoneal carcinomatosis reflects an intrinsic confinement of DGC cells to the peritoneal cavity, or whether these cells retain an equally real capacity to colonize distant organs that simply does not have time to manifest before the patient succumbs to local disease. For intestinal-type GC, distant metastases are common, yet the biological basis for the preferential colonization of specific organs, such as the liver, lung, or bone, remains poorly understood. Traditional *in vitro*, animal, and clinical models are each unable to resolve these questions for distinct reasons mentioned earlier, and, in the specific case of DGC, disease progression in both patients and xenografted animals is invariably truncated by death before the full metastatic potential of diffuse-type cells can be observed. This raised the central question of whether a human gastric cancer avatar model, unconstrained by host survival, could help elucidate the speed and patterns of GC dissemination beyond the point at which conventional models are limited and we hypothesized that a MoC system incorporating 3D spheroids derived from immortalized intestinal- and diffuse-type gastric cancer cell lines would effectively recreate the organ-specific metastatic pathways associated with each subtype, as an initial, tractable step toward this goal, and, beyond the mechanistic gap it addresses, in alignment with the 3Rs framework (Replacement, Reduction, Refinement).

Within this context, this study established the technological and biological foundations of MetaCHIP, a multi-compartment microfluidic platform designed to model the systemic dissemination of gastric cancer under controlled perfusion. The final device integrates spatially separated tissue chambers with a central perfusable channel intended to represent an artificial vascular compartment, thereby providing a framework in which primary tumor cells may ultimately intravasate, circulate, extravasate, and interact with distinct metastatic niches within a single experimental system. To establish a robust and reproducible experimental platform, this work followed a stepwise development strategy in which the engineering properties of the device and the behavior of its individual cellular components were first independently optimized using immortalized cell lines, thereby generating a proof-of-concept before progressing toward the full biological complexity of an organoid-based multi-organ model.

An important strength of this work is that the biological relevance of a multi-organ metastasis model cannot really be separated from how well the engineering side of the device works. In microphysiological systems, technical aspects such as chamber shape, hydrogel placement, sealing, flow distribution, shear stress, and solute transport are not just fabrication details, they directly affect the microenvironment that the cells experience, and therefore the biological results obtained. For this reason, this Discussion starts by looking at the engineering characterization of MetaCHIP before moving on to its biological validation, since how reliable the biology is depends, at least in part, on how well the device itself works.

Device Design and Optimization

The stepwise design of the MetaCHIP platform (v3–v5) reflects a common challenge in microfluidic fabrication: achieving an optimal balance between structural robustness and functional performance.

In MetaCHIP v3, the proximity between tissue chambers increased local mechanical stress during manual biopsy-punch fabrication. Increasing the inter-chamber distance in v4 resolved this fabrication constraint but revealed a second, previously unanticipated problem, as the small chamber diameter was incompatible with reliable Matrigel confinement. This finding suggests that hydrogel behavior within a microwell depends not only on its intrinsic viscosity and gelation kinetics, but also on the geometry of the confining structure, as surface tension and wall contact effects would be expected to become proportionally more influential relative to gravitational settling as chamber

diameter decreases. The v5 modification, which enlarged the chambers to 4 mm, addressed this by giving the hydrogel more surface area to settle into under gravity before it gelled. This improvement in Matrigel confinement suggests that larger chambers are simply easier to work with, since they leave more room for error during manual pipetting. Overall, this iterative process shows that the device geometry could not be optimized for a single goal (fabrication yield) alone; the chamber dimensions had to work well mechanically, fluidically, and for hydrogel handling all at once, and the final v5 design was the geometry that best balanced these different needs (see Chapter IV, Figure 12).

Critically, the ability to identify and resolve these three distinct, sequential difficulties (mechanical stress during punching, hydrogel confinement) within a single design cycle was only feasible because of the rapid prototyping approach used for device fabrication. Since chip layouts were produced by cutting-plotter micromachining rather than photolithography, each design iteration could be produced and tested at low cost and without the time associated with mask design and cleanroom fabrication. This allowed successive versions of the chamber geometry to be evaluated within a small time, making it practical to treat chamber diameter and inter-chamber spacing as tunable parameters.

Flow, Shear Stress, and Solute Transport

The Computational Fluid Dynamics (CFD) simulations provided a quantitative basis for interpreting the physicochemical environment generated within the device. The simulations predicted near-uniform, low-magnitude flow along the central channel, compatible with laminar flow (see Chapter IV, Figure 14 and Figure 15). This behavior minimizes variation of shear stress profiles across the entire length of the perfusion channel, ensuring adequate and stable shear stress across the predicted artificial vasculature path (see Chapter IV, Figure 15). Locally elevated shear stress only at the port–channel junctions indicates that the perfusable compartment maintains a shear regime broadly compatible with endothelial cell culture; this is consistent with the successful HUVEC-C monolayer formation subsequently observed on-chip (see Chapter IV, Figure 33). At the target flow rate of 4 μL/min, the estimated wall shear stress reached a plateau of 0.616 mPa (0.0062 dyn/cm²) along the straight channel section, ranging from 0.348 to 0.838 mPa (0.0035–0.0084 dyn/cm²) when including the locally elevated values near the port junctions (see Chapter III, Table 3). This is approximately two to three orders of magnitude lower than the physiological range reported for the

human microvasculature *in vivo*, where shear stress has been estimated at 1–7 dyn/cm² in arteries and 0.6–1.1 dyn/cm² in veins of various tissues [125]. Comparably low shear magnitudes (~0.01 dyn/cm²) have nonetheless been reported to support successful endothelial monolayer establishment in other microfluidic co-culture platforms [126], supporting the interpretation that the shear stress generated in MetaCHIP, despite being non-physiological, is enough to allow HUVEC-C attachment and monolayer formation. Even so, this represents a limitation of the current work, as the flow rate chosen for the device was primarily chosen by the need to conserve culture medium over long-term, low-volume perfusion experiments, rather than by an attempt to precisely replicate physiological hemodynamic conditions. As a result, the endothelial cells within the device are likely exposed to a shear environment permissive for attachment and monolayer formation, but substantially below the mechanical stimuli experienced by endothelium *in vivo*, which may in turn substantially influence endothelial phenotype and barrier function.

Importantly, the simulation also confirmed that the tissue chambers themselves are shielded from appreciable convective shear, meaning that any exposure of the embedded spheroids to mechanical stimuli is expected to be dominated by diffusive rather than convective forces. The time-resolved concentration maps further showed that solute exchange between the channel and the chambers is diffusion-limited, with the three chambers reaching ~63–67% of source concentration by 120 min despite the channel itself equilibrating within minutes (see Chapter IV, Figure 16).

Fabrication Reproducibility and Technological Validation

The consistent, leak-free assembly of MetaCHIP devices across fabrication batches, maintained over a 16–24 h perfusion period, confirms that the xurography-based fabrication and bonding protocol selected is reliable enough for prolonged cell culture experiments (see Chapter IV, Figure 20). The diffusion assay further supports the CFD predictions: the near-complete equilibration of the tissue chambers by 120 min agrees qualitatively with the simulated kinetics, despite differences between the idealized simulation geometry and the fabricated chip (see Chapter IV, Figure 21 and Figure 22). Notably, the chamber geometry used in the CFD model, based on the design mask, was not perfectly identical to the physical device, which has a slightly narrower chamber opening; this geometric discrepancy is a limitation of the simulation, as the CAD design had to be converted to a PDF vector mesh before CFD simulation. This simplification is expected to slightly overestimate the direct convective and diffusive exchange area

between the main channel and each chamber. The reported flow field, wall-shear-stress values, and mass-conservation checks in the straight channel are not affected by this simplification, as they concern the channel geometry away from the chamber openings. Together, these results show that the v5 platform is ready for biological experiments, as it does not leak, holds together reliably, and allows enough solute exchange between compartments for standard culture protocols and validating our strategy for tumor secretome exposure of the secondary metastatic chambers, as enough conditioned media from the primary tumor can reach the metastatic sites.

Gastric Cancer Spheroid Validation: Seeding Density, Growth Behavior and Metabolic Activity

The comparison between the 100 μm and 200 μm nominal diameters for MKN-74 spheroids revealed a clear trade-off between initial spheroid size and long-term growth capacity. While the 200 μm spheroids started larger, their area remained essentially unchanged over the 72-h monitoring period; the 100 μm spheroids, on the other hand, nearly doubled in size over the same timeframe (see Chapter IV, Figure 25). This pattern is consistent with the interpretation that the larger spheroids reached a size-dependent growth plateau earlier, potentially due to diffusion-limited nutrient and oxygen availability at the spheroid core. The reduced viability observed in the 200 μm spheroids after 10 days further supports this interpretation and is compatible with, although not directly confirmed by, the development of diffusion-related constraints such as central hypoxia or senescence-associated growth arrest, as discussed (see Chapter IV, Figure 27). Importantly, the larger spheroids remained viable overall throughout the observation period, indicating that they were not unsuitable for 3D culture. However, the objective of the present work was not simply to maintain viable tumor spheroids, but to establish a stable and reproducible model for long-term on-chip studies of metastatic dissemination. For this application, spheroids must maintain active growth, structural integrity and high viability, while minimizing cell death throughout extended culture. Consequently, the 100 μm seeding density represented the most appropriate compromise, combining sustained growth, high viability and greater biological stability over time, making it better suited for prolonged microfluidic culture.

MKN-45 spheroids, generated at the 100 μm nominal diameter selected from the MKN-74 optimization, displayed growth and viability profiles broadly similar to MKN-74

spheroids at the same density (see Chapter IV, Figure 28), supporting the generalizability of the seeding protocol across gastric cancer cell lines with different histological subtypes. Notably, MKN-45 spheroids were surrounded by numerous small, dispersed cells that were not observed to the same extent for MKN-74. This is consistent with the diffuse-type morphology typically associated with MKN-45 cells, which display reduced E-cadherin-mediated cell-cell adhesion compared to intestinal-type lines such as MKN-74 [127]. This observation is of relevance to the broader aims of the MetaCHIP platform, as loosely adherent, dispersing cells at the spheroid periphery may better recapitulate the early single-cell dissemination events characteristic of diffuse-type gastric cancer metastasis *in vivo*, compared to more cohesive, intestinal-type tumor models.

Metabolic activity was measured using resazurin reduction, which reflects the ability of metabolically active cells to convert the non-fluorescent dye into the fluorescent resorufin through intracellular redox reactions. Consequently, the fluorescence signal provides an indirect measure of cellular metabolic activity rather than a direct quantification of cell number.

The resazurin incubation time optimization highlighted an important methodological difference between 2D and 3D culture formats: the standard 2 h incubation used for monolayer cultures was insufficient to generate a detectable fluorescence signal in Matrigel-embedded spheroids, and even after 9 h the signal had not reached a plateau (see Chapter IV, Figure 30A). This is consistent with the expectation that resazurin reduction in 3D spheroids is limited by diffusion of the dye into the spheroid core and through the surrounding hydrogel matrix. The selection of a 6 h incubation period represents a practical compromise between assay sensitivity and feasibility, though it should be noted that, since the signal had not reached a plateau at this timepoint, absolute fluorescence values obtained under this protocol are best interpreted as relative comparisons between conditions rather than as measurements of maximal metabolic capacity.

Following assay optimization, both MKN-74 and MKN-45 spheroids displayed increasing metabolic activity during the first days of culture, reaching maximum values around day 14. Then, metabolic activity progressively declined, with a noticeable reduction from day 14 onwards in both cell lines (see Chapter IV, Figure 30B). This decline most likely reflects changes in the physiological state of the spheroids as culture progressed. As tumor spheroids increase in size, oxygen and nutrient diffusion become progressively limited, while metabolic waste accumulates within the core. Together, these changes may

reduce the overall metabolic activity of the spheroid without necessarily indicating complete loss of viability.

Although MKN-45 spheroids consistently generated a stronger resazurin signal than MKN-74 spheroids, this difference cannot be unequivocally attributed to a higher intrinsic metabolic activity of the cells (see Chapter IV, Figure 30A). The diffuse architecture of MKN-45 spheroids, characterized by weaker cell-cell adhesion, likely facilitates the diffusion of resazurin into the spheroid and the release of the fluorescent product back into the surrounding medium. In contrast, the more compact organization of MKN-74 spheroids may impose greater diffusion barriers, potentially limiting resazurin penetration. Consequently, the observed differences probably reflect a combination of intrinsic cellular metabolism and spheroid structural properties.

From the perspective of MetaCHIP development, these findings define an important experimental window during which tumor spheroids remain highly metabolically active. Since metastatic dissemination depends on active cellular processes, including proliferation, migration, and dynamic interactions with the surrounding microenvironment, maintaining robust metabolic activity is desirable for future long-term microfluidic experiments. The decline observed after day 14 therefore suggests that experiments passing this period of time may require further optimization of culture conditions or spheroid architecture.

Endothelialization of the Microfluidic Channel

Establishing a stable endothelial monolayer represents a critical requirement for modeling the hematogenous metastatic cascade in vitro. During metastasis, CTCs continuously interact with the vascular endothelium through processes including adhesion, intravasation, and extravasation. Consequently, the development of a continuous endothelial lining was an essential step toward reproducing the vascular interface of the metastatic microenvironment within MetaCHIP.

Both fibronectin and gelatin supported endothelial attachment and preserved CD31 (PECAM-1) expression, indicating maintenance of endothelial identity under both coating conditions (see Chapter IV, Figure 32). Although no major qualitative differences were observed between the two coatings, fibronectin was selected for subsequent experiments given its widespread use in microvascular endothelial culture and its role as

a major ECM component involved in endothelial adhesion through integrin-mediated interactions [128]. This choice also avoids the xenogeneic origin of gelatin (typically derived from porcine collagen), favoring a substrate more consistent with the human origin of the HUVEC-C line.

The preservation of CD31 expression is particularly relevant, as this adhesion molecule contributes to endothelial cell-cell junctions and vascular barrier integrity [129]. While CD31 staining alone cannot confirm the establishment of a fully functional endothelial barrier, its continuous expression supports the interpretation that HUVEC-Cs are able to form an endothelial monolayer suitable for subsequent proof-of-concept studies.

Interestingly, HUVEC-Cs cultured within the microfluidic channel appeared more densely packed than those maintained under conventional static culture (see Chapter IV, Figure 33). This may partly reflect the substantially smaller dimensions of the microfluidic channel; however, continuous perfusion may also have contributed to this morphology by promoting more homogeneous nutrient distribution and exposing cells to sustained fluid flow. Since these two factors were not independently evaluated, their relative contribution to the observed phenotype cannot be distinguished in the present study.

Nevertheless, further characterization of the endothelial compartment is required to fully validate its physiological relevance. While CD31 expression and confluent monolayer formation demonstrate successful endothelial establishment, future studies should evaluate cytoskeletal organization through F-actin staining, both under conventional static culture and within the microfluidic platform; comparing actin organization between these conditions would help clarify whether confinement and continuous perfusion induce morphological or structural adaptations. In addition, a Live/Dead staining of HUVEC-C cultured on-chip would provide complementary information on cell viability under prolonged microfluidic culture, further strengthening the biological validation of the vascular compartment before undertaking tumor cell extravasation studies.

Culture Medium Compatibility Across Organ Compartments

One of the major challenges in developing MoC platforms lies in identifying culture conditions that simultaneously support multiple cell types with distinct physiological requirements. In the present work, F-12K was selected as the unified culture medium because it is the standard medium for HUVEC-C culture. This decision was primarily driven by the central role of the endothelial compartment within the MetaCHIP platform.

HUVEC-C monolayer lines the perfused microfluidic channel, and it is continuously exposed to the circulating medium throughout the experiment, whereas the target-organ cell lines remain embedded within hydrogel compartments and experience the medium predominantly through diffusive exchange. Moreover, endothelial cells are highly responsive to changes in culture conditions, with alterations in medium composition, growth-factor supplementation, and mechanical cues substantially affecting their proliferation, phenotype, and functional properties [130]. Consequently, rather than adapting the endothelial cells to a non-optimal medium, the strategy adopted was to evaluate whether the remaining cell types could tolerate adaptation to the HUVEC-C medium without compromising their basic cellular function.

In agreement with this rationale, both BEAS-2B and HepaRG cells maintained comparable metabolic activity across all three tested media during 48 h, with no statistically significant differences detected between conditions for either cell type (see Chapter IV, Figure 34 and Figure 35). Nonetheless, these findings support the feasibility of using F-12K as a common culture medium across an increasing number of the platform's organ compartments, extending the compatibility observations from the endothelial compartment to both a lung and a liver cell model.

Future work will extend this medium compatibility assessment to the one remaining organ-specific cell type incorporated into the MetaCHIP platform, namely SGBS adipocytes. At the time of this study, this model was still under optimization, with SGBS cells in the process of adipogenic differentiation. Once this culture is fully established, evaluating its compatibility with the unified F-12K medium will be essential to ensure that all tissue compartments can be maintained under common perfusion conditions without compromising their viability or tissue-specific functionality.

General Limitations and Future Directions

Beyond the limitations discussed for each result, a few broader points apply to the MetaCHIP platform at its current stage of development.

First, biological validation so far has been done on each organ compartment separately (gastric spheroids, endothelial cells, lung cells, liver cells), rather than in the fully integrated, multi-organ setup that is the platform's ultimate goal. This step-by-step approach was a deliberate choice, meant to establish solid baseline conditions for each

cell type before combining them. However, it means that effects that may only emerge from co-culture have not yet been studied. Second, the platform has only been tested over relatively short periods (up to 17 days for spheroid metabolic monitoring, 24 h for endothelialization); its long-term stability under continuous multi-organ perfusion, which will be needed for metastasis studies, is still a work in progress. Third, as noted throughout this Discussion, several functional readouts that would strengthen the biological validation of the platform, such as cytoskeletal organization, barrier permeability, and viability under prolonged on-chip culture, have not yet been performed, and are natural next steps.

Going forward, the next stage of this work is to gradually add the organ compartments once their individual optimization is complete, followed by assembling the full four-organ MetaCHIP configuration under continuous perfusion with a shared F-12K medium. This would allow the platform to be used for its intended purpose: tracking the spread of gastric cancer spheroids through the vascularized channel and their interaction with, and possible colonization of, the other organ compartments, recreating key steps of the metastatic cascade.

In addition to integrating the remaining organ compartments, two additional lines of work will complement the characterization presented in this thesis. First, given the relatively large sample quantities required for proteomic analysis, a set of off-chip conditioned-media experiments is ongoing, in which healthy cell lines (metastatic targets) are exposed to medium previously conditioned by the GC cell lines (MKN-45 and MKN-74), to evaluate resulting changes in protein expression in the metastatic microenvironment, elicited by circulating tumor secreted factors; this approach makes it possible to test the effects of the tumor cell secretome on the other organ compartments without being constrained by the limited cell numbers obtainable on-chip constituting a dynamic platform that will allow us to assess the seed-and-soil theory of tumor priming of the secondary metastatic sites in a dynamically evolving multi-organ system. As a first step in this line of work, BEAS-2B cells were exposed to MKN-45-conditioned medium and profiled by label-free quantitative proteomics at three time points (48, 120, and 192 hours), alongside matched unexposed controls to guide selection of the most informative time point for subsequent replicated experiments.

Second, the on-chip characterization of tumor cell dissemination is planned to rely not only on fluorescent cell tracking, but also on RNA sequencing, which will provide a transcriptomic readout of how gastric cancer cells, and potentially the surrounding organ compartments, respond over the course of on-chip metastasis experiments. Together,

these approaches are expected to provide a more complete molecular picture of tumor-organ interactions within MetaCHIP than morphological or metabolic readouts alone.

In parallel with the experiments described above, preliminary work by other members of the research group has assessed the feasibility of tracking GC cells using cell-tracer dyes, namely CellTrace Far Red and CellTrace Green, in a different microfluidic chip. These results indicate that labeled cells, particularly those stained with Far Red, remain trackable for up to 16 days in culture, suggesting that this labeling strategy is compatible with the extended culture timeframes required for future metastasis-tracking experiments. Although these results were obtained outside of the MetaCHIP platform and were not generated as part of the present work, they are a relevant and encouraging proof of concept.

Finally, after establishing this proof-of-concept using immortalized cell lines, the next step we want to take is to move toward patient-derived organoids (PDOs). Our group already has an established protocol for generating gastric organoids from healthy tissue obtained from patients undergoing bariatric surgery. Building on this, the long-term goal is to make MetaCHIP as human-relevant as possible by replacing the immortalized cell lines with patient-derived organoids, which would better capture patient-specific tissue characteristics than established cell lines can.

Conclusion

Taken together, the results presented in this work show that the MetaCHIP platform is a feasible multi-compartment microfluidic system for modeling gastric cancer metastasis. The iterative device redesign process led to a platform (v5) that balances fabrication reliability, hydrogel confinement, and fluidic function, with CFD simulations confirming a diffusion-dominated transport regime and a low, though endothelium-permissive, shear environment within the perfusable channel. Biologically, the platform supports the formation and long-term maintenance of gastric cancer spheroids from both intestinal-type (MKN-74) and diffuse-type (MKN-45) cell lines, the formation of a confluent endothelial monolayer under perfusion, and the compatibility of at least two additional organ-specific cell types (BEAS-2B and HepaRG) with a shared culture medium (F-12K). While full integration of all four organ compartments and validation of dynamic tumor cell dissemination remain as the next phases of this project, the technological and biological groundwork established here provides a solid basis for MetaCHIP's continued development as a human-relevant, animal-free alternative for studying GC metastasis.

More broadly, the work described in this thesis represents the first stage of a long-term goal: the establishment of MetaCHIP not simply as a single-purpose metastasis model, but as an easily reproducible platform that can be readily adopted by other laboratories and adapted to a range of different studies. The modular architecture of the device, combining individualized tissue compartments with a shared perfusable central channel, is not just limited to the GC metastasis application explored here; the same design could equally support other studies that benefit from this configuration, such as drug delivery and permeability testing across the vascularized channel, or the investigation of metastatic dissemination from other primary tumor types. In this sense, the present characterization of MetaCHIP's fabrication, fluidic behavior, and biological compatibility is intended not only to validate the specific gastric cancer metastasis model pursued in this thesis, but also to lay the groundwork for the platform's broader use as a flexible, accessible tool for the organ-on-chip community.

VI. REFERENCES

1. World Health Organization. *Cancer*. 2025 [cited 2026 3 March]; Available from: https://www.who.int/news-room/fact-sheets/detail/cancer.
2. Bray, F., et al., *Global cancer statistics 2022: GLOBOCAN estimates of incidence and mortality worldwide for 36 cancers in 185 countries.* CA Cancer J Clin, 2024. **74**(3): p. 229-263.
3. Siegel, R.L., et al., *Cancer statistics, 2025.* CA Cancer J Clin, 2025. **75**(1): p. 10-45.
4. Bizuayehu, H.M., et al., *Global Disparities of Cancer and Its Projected Burden in 2050.* JAMA Netw Open, 2024. **7**(11): p. e2443198.
5. Hanahan, D. and R.A. Weinberg, *The hallmarks of cancer.* Cell, 2000. **100**(1): p. 57-70.
6. Hanahan, D. and Robert A. Weinberg, *Hallmarks of Cancer: The Next Generation.* Cell, 2011. **144**(5): p. 646-674.
7. Hanahan, D., *Hallmarks of Cancer: New Dimensions.* Cancer Discov, 2022. **12**(1): p. 31-46.
8. Hanahan, D., *Hallmarks of cancer-Then and now, and beyond.* Cell, 2026.
9. Lai, S., *A human mode of intestinal type gastric carcinoma.* Med Hypotheses, 2019. **123**: p. 27-29.
10. Duan, Y., et al., *Helicobacter pylori and gastric cancer: mechanisms and new perspectives.* J Hematol Oncol, 2025. **18**(1): p. 10.
11. Tian, C.F., et al., *Tumor microenvironment characteristics association with clinical outcome in patients with resected intestinal-type gastric cancer.* Oncologist, 2024. **29**(10): p. e1280-e1290.
12. Xia, J.Y. and A.A. Aadam, *Advances in screening and detection of gastric cancer.* J Surg Oncol, 2022. **125**(7): p. 1104-1109.
13. Jiang, N., *Global burden and future trends of gastric cancer in women of reproductive age: estimates from the GBD 2021 Study, 1990-2050.* Front Oncol, 2025. **15**: p. 1616936.
14. Mamun, T.I., S. Younus, and M.H. Rahman, *Gastric cancer-Epidemiology, modifiable and non-modifiable risk factors, challenges and opportunities: An updated review.* Cancer Treat Res Commun, 2024. **41**: p. 100845.
15. Jun, J.K., et al., *Effectiveness of the Korean National Cancer Screening Program in Reducing Gastric Cancer Mortality.* Gastroenterology, 2017. **152**(6): p. 1319-1328.e7.
16. Assumpção, P.P., et al., *The diffuse-type gastric cancer epidemiology enigma.* BMC Gastroenterol, 2020. **20**(1): p. 223.

17. Thrift, A.P., T.N. Wenker, and H.B. El-Serag, *Global burden of gastric cancer: epidemiological trends, risk factors, screening and prevention.* Nat Rev Clin Oncol, 2023. **20**(5): p. 338-349.
18. Park, J.Y., et al., *Global lifetime estimates of expected and preventable gastric cancers across 185 countries.* Nat Med, 2025. **31**(9): p. 3020-3027.
19. Wang, X., et al., *Emerging trends in early-onset gastric cancer.* Chin Med J (Engl), 2024. **137**(18): p. 2146-2156.
20. Karimi, P., et al., *Gastric cancer: descriptive epidemiology, risk factors, screening, and prevention.* Cancer Epidemiol Biomarkers Prev, 2014. **23**(5): p. 700-13.
21. Ma, J., et al., *Lauren classification and individualized chemotherapy in gastric cancer.* Oncol Lett, 2016. **11**(5): p. 2959-2964.
22. Wu, L.W., et al., *Diffuse Gastric Cancer: A Comprehensive Review of Molecular Features and Emerging Therapeutics.* Target Oncol, 2024. **19**(6): p. 845-865.
23. Koemans, W.J., et al., *The metastatic pattern of intestinal and diffuse type gastric carcinoma - A Dutch national cohort study.* Cancer Epidemiol, 2020. **69**: p. 101846.
24. Díaz Del Arco, C., et al., *Clinicopathological differences, risk factors and prognostic scores for western patients with intestinal and diffuse-type gastric cancer.* World J Gastrointest Oncol, 2022. **14**(6): p. 1162-1174.
25. Shimamura, T., et al., *Overexpression of MUC13 is associated with intestinal-type gastric cancer.* Cancer Sci, 2005. **96**(5): p. 265-73.
26. Lee, J.W., et al., *Identification of different gene expressions between diffuse- and intestinal-type spheroid-forming gastric cancer cells.* Gastric Cancer, 2019. **22**(5): p. 967-979.
27. Gullo, I., et al., *Precancerous lesions of the stomach, gastric cancer and hereditary gastric cancer syndromes.* Pathologica, 2020. **112**(3): p. 166-185.
28. Ji, K., et al., *Construction and interpretation of machine learning-based prognostic models for survival prediction among intestinal-type and diffuse-type gastric cancer patients.* World J Surg Oncol, 2024. **22**(1): p. 275.
29. Pyo, J.H., et al., *Early gastric cancer with a mixed-type Lauren classification is more aggressive and exhibits greater lymph node metastasis.* J Gastroenterol, 2017. **52**(5): p. 594-601.
30. Chen, Y.C., et al., *Clinicopathological Variation of Lauren Classification in Gastric Cancer.* Pathol Oncol Res, 2016. **22**(1): p. 197-202.
31. *Comprehensive molecular characterization of gastric adenocarcinoma.* Nature, 2014. **513**(7517): p. 202-9.

32. Shi, D., et al., *Research advances in the molecular classification of gastric cancer.* Cell Oncol (Dordr), 2024. **47**(5): p. 1523-1536.
33. Riquelme, I., et al., *Molecular classification of gastric cancer: Towards a pathway-driven targeted therapy.* Oncotarget, 2015. **6**(28): p. 24750-79.
34. O'Connor, K.G., *Gastric cancer.* Semin Oncol Nurs, 1999. **15**(1): p. 26-35.
35. Hatta, W., et al., *The Impact of Tobacco Smoking and Alcohol Consumption on the Development of Gastric Cancers.* Int J Mol Sci, 2024. **25**(14).
36. Stjepanovic, N., et al., *Hereditary gastrointestinal cancers: ESMO Clinical Practice Guidelines for diagnosis, treatment and follow-up†.* Annals of Oncology, 2019. **30**(10): p. 1558-1571.
37. Correa, P. and M.B. Piazuelo, *The gastric precancerous cascade.* J Dig Dis, 2012. **13**(1): p. 2-9.
38. Díaz del Arco, C., M.J. Fernández Aceñero, and L. Ortega Medina, *Molecular Classifications in Gastric Cancer: A Call for Interdisciplinary Collaboration.* International Journal of Molecular Sciences, 2024. **25**(5): p. 2649.
39. Li, F., et al., *Molecular evolution of intestinal-type early gastric cancer according to Correa cascade.* J Biomed Res, 2024. **39**(3): p. 270-285.
40. Toh, J.W.T. and R.B. Wilson, *Pathways of Gastric Carcinogenesis, Helicobacter pylori Virulence and Interactions with Antioxidant Systems, Vitamin C and Phytochemicals.* Int J Mol Sci, 2020. **21**(17).
41. Ansari, S., et al., *Diffuse Gastric Cancer: A Summary of Analogous Contributing Factors for Its Molecular Pathogenicity.* Int J Mol Sci, 2018. **19**(8).
42. Raju, D., et al., *Gastric Signet Ring Cell Carcinoma: Tumor Microenvironment Reprogramming and Novel Therapeutic Targets With Emphasis on GRIN2D.* Clin Transl Sci, 2025. **18**(11): p. e70424.
43. Garcia-Pelaez, J., et al., *Genotype-first approach to identify associations between CDH1 germline variants and cancer phenotypes: a multicentre study by the European Reference Network on Genetic Tumour Risk Syndromes.* Lancet Oncol, 2023. **24**(1): p. 91-106.
44. Oliveira, C., et al., *Germline CDH1 deletions in hereditary diffuse gastric cancer families.* Hum Mol Genet, 2009. **18**(9): p. 1545-55.
45. Lobo, S., et al., *Hereditary diffuse gastric cancer spectrum associated with germline CTNNA1 loss of function revealed by clinical and molecular data from 351 carrier families and over 37 000 non-carrier controls.* Gut, 2025.
46. van der Sluis, L., et al., *Current advances and challenges in Managing Hereditary Diffuse Gastric Cancer (HDGC): a narrative review.* Hered Cancer Clin Pract, 2024. **22**(1): p. 21.

47. Luo, W., et al., *CDH1 Gene and Hereditary Diffuse Gastric Cancer Syndrome: Molecular and Histological Alterations and Implications for Diagnosis And Treatment.* Front Pharmacol, 2018. **9**: p. 1421.
48. Corso, G., et al., *Second-hit CDH1 gene mechanisms in hereditary diffuse gastric and lobular breast cancer syndrome: frequency and impact on tumorigenesis.* Hum Mol Genet, 2025. **34**(16): p. 1345-1352.
49. Lim, H.J., L. Zhuang, and R.C. Fitzgerald, *Current advances in understanding the molecular profile of hereditary diffuse gastric cancer and its clinical implications.* J Exp Clin Cancer Res, 2023. **42**(1): p. 57.
50. Morgan, E., et al., *The current and future incidence and mortality of gastric cancer in 185 countries, 2020-40: A population-based modelling study.* EClinicalMedicine, 2022. **47**: p. 101404.
51. Kim, T.U., et al., *MDCT features in the differentiation of T4a gastric cancer from less-advanced gastric cancer: significance of the hyperattenuating serosa sign.* Br J Radiol, 2013. **86**(1029): p. 20130290.
52. Cao, L.L., et al., *Evaluation of the Eighth Edition of the American Joint Committee on Cancer TNM Staging System for Gastric Cancer: An Analysis of 7371 Patients in the SEER Database.* Gastroenterol Res Pract, 2019. **2019**: p. 6294382.
53. Semenova, Y., et al., *Chemotherapy Options for Locally Advanced Gastric Cancer: A Review.* Cancers (Basel), 2025. **17**(5).
54. Zhu, K., et al., *ypT0 gastric carcinoma after preoperative chemotherapy: a unique status according to AJCC 8(th) edition cancer staging system.* Transl Cancer Res, 2020. **9**(12): p. 7384-7393.
55. Yaprak, G., et al., *Prognostic factors for survival in patients with gastric cancer: Single-centre experience.* North Clin Istanb, 2020. **7**(2): p. 146-152.
56. Baba, H., et al., *Prognostic factors for stage IV gastric cancer.* Int Surg, 2013. **98**(2): p. 181-7.
57. Monster, J.L., et al., *Diffuse gastric cancer: Emerging mechanisms of tumor initiation and progression.* Biochim Biophys Acta Rev Cancer, 2022. **1877**(3): p. 188719.
58. Iyer, P., et al., *Diffuse gastric cancer: histologic, molecular, and genetic basis of disease.* Transl Gastroenterol Hepatol, 2020. **5**: p. 52.
59. Patients, V.o.C. *Stages of Stomach Cancer and Their Relevance to Prognosis*. 2019; Available from: https://www.voiceofcancerpatients.com/articles/stages-of-stomach-cancer-and-their-relevance-to-prognosis.
60. Chambers, A.F. and Z. Werb, *Invasion and metastasis--recent advances and future challenges.* J Mol Med (Berl), 2015. **93**(4): p. 361-8.

61. Plaks, V., C.D. Koopman, and Z. Werb, *Cancer. Circulating tumor cells.* Science, 2013. **341**(6151): p. 1186-8.
62. Amelot, A., et al., *Timeline metastatic progression: in the wake of the « seed and soil » theory.* Med Oncol, 2017. **34**(11): p. 185.
63. Ribatti, D., G. Mangialardi, and A. Vacca, *Stephen Paget and the 'seed and soil' theory of metastatic dissemination.* Clin Exp Med, 2006. **6**(4): p. 145-9.
64. Riihimäki, M., et al., *Metastatic spread in patients with gastric cancer.* Oncotarget, 2016. **7**(32): p. 52307-52316.
65. Zheng, H., et al., *Pathobiological characteristics of intestinal and diffuse-type gastric carcinoma in Japan: an immunostaining study on the tissue microarray.* J Clin Pathol, 2007. **60**(3): p. 273-7.
66. Korivi, B.R., et al., *Intestinal and diffuse gastric cancer: a retrospective study comparing primary sites.* Clinical Imaging, 2019. **56**: p. 33-40.
67. Shimizu, D., M. Kanda, and Y. Kodera, *Emerging evidence of the molecular landscape specific for hematogenous metastasis from gastric cancer.* World J Gastrointest Oncol, 2018. **10**(6): p. 124-136.
68. Liu, H.K., et al., *Inhibitory effects of gamma-tocotrienol on invasion and metastasis of human gastric adenocarcinoma SGC-7901 cells.* J Nutr Biochem, 2010. **21**(3): p. 206-13.
69. Wang, R., et al., *IFT80 Improves Invasion Ability in Gastric Cancer Cell Line via ift80/p75NGFR/MMP9 Signaling.* Int J Mol Sci, 2018. **19**(11).
70. Zhu, Z., et al., *Effect of gastric cancer stem cell on gastric cancer invasion, migration and angiogenesis.* Int J Med Sci, 2020. **17**(13): p. 2040-2051.
71. Kondo, R., et al., *Cancer-associated fibroblast-dependent and -independent invasion of gastric cancer cells.* J Cancer Res Clin Oncol, 2023. **149**(8): p. 5309-5319.
72. Chen, H.Y., et al., *Ouabain Suppresses Cell Migration and Invasion in Human Gastric Cancer AGS Cells Through the Inhibition of MMP Signaling Pathways.* Anticancer Res, 2021. **41**(9): p. 4365-4375.
73. Pijuan, J., et al., *In vitro Cell Migration, Invasion, and Adhesion Assays: From Cell Imaging to Data Analysis.* Front Cell Dev Biol, 2019. **7**: p. 107.
74. Pan, Y., L. Zhao, and J. Fang, *Animal models and pathogenesis of gastric cancer: from premalignant conditions-to-metastasis.* Cancer Biol Med, 2026. **23**(5): p. 637-56.
75. Busuttil, R.A., et al., *An orthotopic mouse model of gastric cancer invasion and metastasis.* Scientific Reports, 2018. **8**(1): p. 825.

76. Okazaki, M., et al., *Establishing a xenograft mouse model of peritoneal dissemination of gastric cancer with organ invasion and fibrosis.* BMC Cancer, 2017. **17**(1): p. 23.
77. Giraud, J., et al., *Orthotopic Patient-Derived Xenografts of Gastric Cancer to Decipher Drugs Effects on Cancer Stem Cells and Metastatic Dissemination.* Cancers (Basel), 2019. **11**(4).
78. Reddavid, R., et al., *Patient-Derived Orthotopic Xenograft models in gastric cancer: a systematic review.* Updates Surg, 2020. **72**(4): p. 951-966.
79. Poh, A.R., et al., *Mouse models for gastric cancer: Matching models to biological questions.* Journal of Gastroenterology and Hepatology, 2016. **31**(7): p. 1257-1272.
80. Wang, L., et al., *Subsite-specific metastatic organotropism and risk in gastric cancer: A population-based cohort study of the US SEER database and a Chinese single-institutional registry.* Cancer Med, 2023. **12**(19): p. 19595-19606.
81. Zeng, C.D.D., et al., *Preoperative Folate Receptor-Positive Circulating Tumor Cells Are Associated With Occult Peritoneal Metastasis and Early Recurrence in Gastric Cancer Patients: A Prospective Cohort Study.* Front Oncol, 2022. **12**: p. 769203.
82. Abdolahi, S., et al., *Patient-derived xenograft (PDX) models, applications and challenges in cancer research.* J Transl Med, 2022. **20**(1): p. 206.
83. Long, J.E., M. Jankovic, and D. Maddalo, *Drug discovery oncology in a mouse: concepts, models and limitations.* Future Sci OA, 2021. **7**(8): p. Fso737.
84. Shyu, R.Y., L.K. Wang, and F.M. Tsai, *Translating Gastric Cancer Genomics into Targeted Therapy: Mechanistic Insights from Animal Models and Patient-Derived Systems.* Cells, 2026. **15**(4).
85. Tannenbaum, J. and B.T. Bennett, *Russell and Burch's 3Rs then and now: the need for clarity in definition and purpose.* J Am Assoc Lab Anim Sci, 2015. **54**(2): p. 120-32.
86. Fatehullah, A., S.H. Tan, and N. Barker, *Organoids as an in vitro model of human development and disease.* Nat Cell Biol, 2016. **18**(3): p. 246-54.
87. Lancaster, M.A. and J.A. Knoblich, *Organogenesis in a dish: modeling development and disease using organoid technologies.* Science, 2014. **345**(6194): p. 1247125.
88. Clevers, H., *Modeling Development and Disease with Organoids.* Cell, 2016. **165**(7): p. 1586-1597.
89. Drost, J. and H. Clevers, *Organoids in cancer research.* Nat Rev Cancer, 2018. **18**(7): p. 407-418.

90. Sato, T., et al., *Single Lgr5 stem cells build crypt-villus structures in vitro without a mesenchymal niche.* Nature, 2009. **459**(7244): p. 262-5.
91. Barker, N., et al., *Lgr5(+ve) stem cells drive self-renewal in the stomach and build long-lived gastric units in vitro.* Cell Stem Cell, 2010. **6**(1): p. 25-36.
92. Huch, M., et al., *In vitro expansion of single Lgr5+ liver stem cells induced by Wnt-driven regeneration.* Nature, 2013. **494**(7436): p. 247-50.
93. Huch, M., et al., *Unlimited in vitro expansion of adult bi-potent pancreas progenitors through the Lgr5/R-spondin axis.* Embo j, 2013. **32**(20): p. 2708-21.
94. Dye, B.R., et al., *In vitro generation of human pluripotent stem cell derived lung organoids.* Elife, 2015. **4**.
95. Karthaus, W.R., et al., *Identification of multipotent luminal progenitor cells in human prostate organoid cultures.* Cell, 2014. **159**(1): p. 163-175.
96. Vlachogiannis, G., et al., *Patient-derived organoids model treatment response of metastatic gastrointestinal cancers.* Science, 2018. **359**(6378): p. 920-926.
97. Yan, H.H.N., et al., *A Comprehensive Human Gastric Cancer Organoid Biobank Captures Tumor Subtype Heterogeneity and Enables Therapeutic Screening.* Cell Stem Cell, 2018. **23**(6): p. 882-897.e11.
98. McCracken, K.W., et al., *Modelling human development and disease in pluripotent stem-cell-derived gastric organoids.* Nature, 2014. **516**(7531): p. 400-4.
99. Bartfeld, S., et al., *In vitro expansion of human gastric epithelial stem cells and their responses to bacterial infection.* Gastroenterology, 2015. **148**(1): p. 126-136.e6.
100. Nanki, K., et al., *Divergent Routes toward Wnt and R-spondin Niche Independency during Human Gastric Carcinogenesis.* Cell, 2018. **174**(4): p. 856-869.e17.
101. Whitesides, G.M., *The origins and the future of microfluidics.* Nature, 2006. **442**(7101): p. 368-73.
102. Filippi, M., et al., *Microfluidic Tissue Engineering and Bio-Actuation.* Advanced Materials, 2022. **34**(23): p. 2108427.
103. Zhang, B. and M. Radisic, *Organ-on-a-chip devices advance to market.* Lab Chip, 2017. **17**(14): p. 2395-2420.
104. Huh, D., G.A. Hamilton, and D.E. Ingber, *From 3D cell culture to organs-on-chips.* Trends Cell Biol, 2011. **21**(12): p. 745-54.
105. Ergir, E., et al., *Small Force, Big Impact: Next Generation Organ-on-a-Chip Systems Incorporating Biomechanical Cues.* Front Physiol, 2018. **9**: p. 1417.

106. Stucki, A.O., et al., *A lung-on-a-chip array with an integrated bio-inspired respiration mechanism.* Lab on a Chip, 2015. **15**(5): p. 1302-1310.
107. Liu, J., et al., *Design and Fabrication of a Liver-on-a-chip Reconstructing Tissue-tissue Interfaces.* Front Oncol, 2022. **12**: p. 959299.
108. Kasendra, M., et al., *Development of a primary human Small Intestine-on-a-Chip using biopsy-derived organoids.* Sci Rep, 2018. **8**(1): p. 2871.
109. Li, Z., et al., *Assessment of cadmium-induced nephrotoxicity using a kidney-on-a-chip device.* Toxicol Res (Camb), 2017. **6**(3): p. 372-380.
110. Ferreira, D.A., et al., *Bioinspired human stomach-on-a-chip with in vivo like function and architecture.* Lab on a Chip, 2023. **23**(3): p. 495-510.
111. Ferreira, D.A., et al., *A Fast Alternative to Soft Lithography for the Fabrication of Organ-on-a-Chip Elastomeric-Based Devices and Microactuators.* Adv Sci (Weinh), 2021. **8**(8): p. 2003273.
112. Bhatia, S.N. and D.E. Ingber, *Microfluidic organs-on-chips.* Nat Biotechnol, 2014. **32**(8): p. 760-72.
113. Skardal, A., T. Shupe, and A. Atala, *Organoid-on-a-chip and body-on-a-chip systems for drug screening and disease modeling.* Drug Discov Today, 2016. **21**(9): p. 1399-1411.
114. Aleman, J. and A. Skardal, *A multi-site metastasis-on-a-chip microphysiological system for assessing metastatic preference of cancer cells.* Biotechnol Bioeng, 2019. **116**(4): p. 936-944.
115. Liu, L., et al., *Leaf-vein-inspired multi-organ microfluidic chip for modeling breast cancer CTC organotropism.* Front Oncol, 2025. **15**: p. 1602225.
116. Ma, J., et al., *Patient-derived organoids in gastric cancer: bridging the tumor microenvironment to functional precision oncology.* Front Bioeng Biotechnol, 2026. **14**: p. 1790902.
117. Castagna, A., et al., *Imaging gastric cancer metastasis progression in an organotypic, three-dimensional functional model of the human peritoneum.* Pleura Peritoneum, 2025. **10**(1): p. 11-17.
118. Waters, L.J., et al., *Effect of plasma surface treatment of poly(dimethylsiloxane) on the permeation of pharmaceutical compounds.* Journal of Pharmaceutical Analysis, 2017. **7**(5): p. 338-342.
119. Bhattacharya, S., et al., *Studies on surface wettability of poly(dimethyl) siloxane (PDMS) and glass under oxygen-plasma treatment and correlation with bond strength.* Journal of Microelectromechanical Systems, 2005. **14**(3): p. 590-597.

120. Elveflow. *Microfluidics Application Note: Pressure-driven flow control*. [Internet] 2019 [cited 12/08/2026; Available from: https://elveflow.com/microfluidic-applications/pressure-driven-flow-control/.
121. Kanda, M. and Y. Kodera, *Molecular mechanisms of peritoneal dissemination in gastric cancer.* World J Gastroenterol, 2016. **22**(30): p. 6829-40.
122. Rocha, S., et al., *3D Cellular Architecture Affects MicroRNA and Protein Cargo of Extracellular Vesicles.* Adv Sci (Weinh), 2019. **6**(4): p. 1800948.
123. Silva, F.S.G., et al., *Determination of Metabolic Viability and Cell Mass Using a Tandem Resazurin/Sulforhodamine B Assay.* Curr Protoc Toxicol, 2016. **68**: p. 2.24.1-2.24.15.
124. Clark, R.A., J.M. Folkvord, and L.D. Nielsen, *Either exogenous or endogenous fibronectin can promote adherence of human endothelial cells.* J Cell Sci, 1986. **82**: p. 263-80.
125. Santamaría, R., et al., *Remodeling of the Microvasculature: May the Blood Flow Be With You.* Front Physiol, 2020. **11**: p. 586852.
126. Rogers, M.T., et al., *A high-throughput microfluidic bilayer co-culture platform to study endothelial-pericyte interactions.* Sci Rep, 2021. **11**(1): p. 12225.
127. Yokozaki, H., *Molecular characteristics of eight gastric cancer cell lines established in Japan.* Pathol Int, 2000. **50**(10): p. 767-77.
128. Short, S.M., G.A. Talbott, and R.L. Juliano, *Integrin-mediated signaling events in human endothelial cells.* Mol Biol Cell, 1998. **9**(8): p. 1969-80.
129. Privratsky, J.R. and P.J. Newman, *PECAM-1: regulator of endothelial junctional integrity.* Cell Tissue Res, 2014. **355**(3): p. 607-19.
130. Demeter, F., et al., *Nature versus nurture: genetic background and media composition shape endothelial cell transcriptomes in vitro.* Scientific Reports, 2026. **16**(1): p. 13621.

FACULDADE DE **MEDICINA**